Computational Modeling of Hall Thruster Channel Wall Erosion

by

John Tamin Yim

A dissertation submitted in partial fulfillment
of the requirements for the degree of
Doctor of Philosophy
(Aerospace Engineering)
in The University of Michigan
2008

Doctoral Committee:

Professor Iain D. Boyd, Co-Chair
Assistant Professor Michael Keidar, George Washington University, Co-Chair
Professor Alec D. Gallimore
Associate Professor Michael L. Falk

To my parents.

ACKNOWLEDGEMENTS

There have been many people who have supported, encouraged, aided, guided, advised, and just been there for me throughout my time at the University of Michigan. I would like to start with my advisor, Iain Boyd. I really could not have asked for a better advisor supervising my entirely enjoyable and successful graduate career. He has always been available for guidance as well as pushing me forward in my research. I'd also like to thank Michael Keidar, my other co-chair, for his continued support in my research from starting me off on his codes to helping me around tricky issues with plasma modeling. His plethora of ideas and suggestions have always been inspiring as well.

I'd like to thank NASA Glenn Research Center, particularly the electric propulsion branch headed by Dave Manzella, for their support for me throughout my time in graduate school. It was their interest in Hall thruster erosion modeling that began me on this research journey and their continued advice and support were a great boon. Plus, there is always a certain sense of satisfaction being able to work with useful data and especially with direct and real applications.

I'd also like to acknowledge the National Science Foundation for their support for three years through the Graduate Research Fellowship Program. It was a great honor to be chosen by them to be able to freely pursue different avenues of research and being able to investigate a variety of fields related to my main topic.

A big thanks to all of my friends here at the university. The guys in the department and particularly in our non-equilibrium gas and plasma dynamics group have always been a blast to be around, as they are on the whole both smart and entertaining. Thanks for always fielding my dumb questions too. With my friends from church, especially the other graduate students, it has been a true blessing to have been in fellowship with them as we shared our joys and frustrations of grad school life. Those guys are some of the best people I have ever gotten to know.

Finally, a special thanks to my parents and my brother. You have always been there for me from the very beginning, and I can't even begin to express how much your continued love and support have meant to me. Thank you.

TABLE OF CONTENTS

CHAPTER

LIST OF FIGURES

LIST OF TABLES

NOMENCLATURE

Variables

A	Area [m^2]
A	Fitting coefficient
B	Magnetic field [T]
B	Fitting coefficient
D_0	Dimer energy [eV]
E	Electric field [V/m]
E	Energy [eV]
E_{th}	Threshold energy [eV]
$\vec{F}$	Force [N]
F	Flux vector (axial)
G	Flux vector (radial)
I	Current [A]
I_{sp}	Specific impulse [s]
N	Number of particles
Q	Heat (power density) [W/m^3]
S	Source term
S_n	Elastic stopping power
$\mathcal{S}$	Surface [m^2]
T	Temperature [K]
T_0	Equilibrium temperature [K]
$\bar{T}$	Average temperature [K]

$\vec{T}$	Thrust [N]
U	Conserved variable vector
U_s	Surface binding energy
$\mathcal{V}$	Volume [m^3]
V_d	Discharge voltage [V]
Y	Sputter yield [mm^3/C]
$\hat{Y}$	Normalized sputter yield (angular dependence)
Z	Atomic number
a	Sound speed [m/s]
a_0	Bohr radius [Å]
a_F	Firsov screening length [Å]
$\vec{a}$	Acceleration vector [m/s^2]
b_{ij}	Bond-order term
e	Elementary charge [C]
e_{int}	Internal energy [J]
f_c	Cutoff function
f_R	Repulsive component of interatomic potential
f_A	Attractive component of interatomic potential
h	Channel width [m]
j	Current density [A/m^2]
k	Boltzmann constant [J/K]
m	Mass [kg]
$\dot{m}$	Mass flow rate [kg/s]
n	Number density [m^{-3}]
p	Pressure [N/m^2]
q	Charge [C]
r	Radius [m]
r_0	Dimer separation [Å]

r_{ij}	Distance between particle i and j [Å]
$\vec{r}$	Position vector [m]
s	Secondary electron emission coefficient
s_e	Reduced electronic stopping power
s_n	Reduced nuclear stopping power
t	Time [s]
v	Velocity [m/s]
y	Differential sputter yield
$\vec{v}$	Velocity vector [m/s]
α	Incidence angle of sputtered particle [deg]
β	Ionization rate [m^3/s]
δ	Kronecker delta
ϵ_0	Permittivity of free space [F/m]
θ	Ion incidence angle from surface normal [deg]
θ_{ijk}	Angle between particle vectors ij and ik [rad]
λ_D	Debye length [m]
μ	Mobility [m^2/(V s)]
ν	Collision frequency [s^{-1}]
ρ	Density [kg/m^3]
σ	Collision cross section [m^2]
τ	Time constant [s]
ϕ	Plasma potential [V]
ϕ	Azimuthal angle of sputtered particle [deg]
Φ	Interatomic potential function [V]
ψ	Magnetic field streamfunction [T m^2]
ω	Gyrofrequency [1/s]

Subscripts

a	Neutral atom
e	Electron
h	Heavy particle (neutral atom or ion)
i	Ion
r	Radial
s	Sheath
z	Axial

Abbreviations

BCA	Binary Collision Approximation
BN	Boron Nitride (h- hexagonal, c- cubic)
BOL	Beginning-Of-Life
EP	Electric Propulsion
HARP	High-speed Axial Reciprocating Probe
KE	Kinetic Energy
MD	Molecular Dynamics
PIC	Particle-In-Cell
QCM	Quartz Crystal Microbalance
SPT	Stationary Plasma Thruster
TAL	Thruster with Anode Layer

CHAPTER I

Introduction

1.1 Objective

The exploration and utilization of space requires effective, efficient, and reliable means of propulsion. The goal of the work presented in this thesis is to improve one important aspect of propulsion design through the development of computational modeling of Hall thruster discharge channel wall erosion. The erosion of the channel walls is one of the main life-limiting factors for Hall thrusters, a form of space electric propulsion. As mission requirements and expectations involving Hall thrusters increase, the need to predict and validate thruster lifetimes also increases. Experimental characterization of the erosion is time-consuming and costly, requiring up to tens of thousands of hours of testing and costing hundreds of thousands of dollars for propellant supply and use of facilities. Computational tools that can model the erosion quickly and accurately are therefore a valuable asset for the thruster design and mission planning processes. Research in this area will provide a better understanding of the erosion physics and will be useful for future thruster development. Erosion modeling tools will also aid in the acceptance and implementation of Hall thrusters as a primary propulsion device through improving confidence of their long term reliability. As Hall thrusters continue to develop in promising and exciting ways, they will enhance the capability to perform further reaching and faster growing future space exploration and use.

1.2 Electric Propulsion

Rockets operate on of the basic principle set forth in Newton's third law of motion, namely that every action has an equal and opposite reaction. Typically, propulsion systems expel a gas product, the action, in order to propel the spacecraft, the reaction. Electric propulsion (EP) refers to propulsion systems that primarily use electric power, as opposed to chemical, nuclear, or other sources, to produce thrust.

There are three main categories of EP devices: electrothermal, electrostatic, and electromagnetic.[54] These divisions are based on the mechanism through which electric power is utilized to accelerate the exhaust flow. Electrothermal devices use electric power to heat a propellant flow. The propellant gas is heated through a heating element, as in a resistojet, or through direct electric arc heating, as in an arcjet, for example. The propellant gains energy as it is heated and then is expelled through a nozzle. Electrostatic thrusters use an electric field to accelerate charged particles. Instead of a thermal means of adding energy to the flow, an electrostatic force is applied to accelerate the propellant out of the thruster. Examples include ion thrusters, which accelerate ions, colloid thrusters, which accelerate charged droplets, and field emission electric propulsion (FEEP), which accelerate ions or droplets off from liquid Taylor cones. Electromagnetic thrusters use combined electric and magnetic fields to accelerate the propellant. Magnetoplasmadynamic (MPD) thrusters offer a high throughput electromagnetic acceleration of an ionized gas. Pulsed plasma thrusters (PPT) vaporize a solid propellant and accelerate the resulting plasma electromagnetically in pulses to produce thrust. Hall thrusters can be considered to be either electromagnetic or electrostatic, or some combination of the two, as they emulate portions from both categories.

Electric propulsion offers a few advantages over traditional chemical propulsion. The main draw is that it allows for a lower ratio of the propellant mass to the total mass of the spacecraft. Reducing the ratio of the propellant mass is accomplished by increasing the exhaust velocities through a more effective acceleration of the propellant by either adding additional thermal energy, as in the electrothermal case, or by applying a body force directly on the propellant, as in the electrostatic or electromagnetic forms. How higher exhaust velocities lead to a lower propellant mass ratio can be seen starting with Newton's second law of motion,

$$F = ma \tag{1.1}$$

The force in this case is the thrust produced by the rocket,

$$F = T = \dot{m} v_{\text{exit}} \tag{1.2}$$

where $\dot{m}$ is the propellant mass flow rate and v_{exit} is the propellant exhaust velocity. Rewriting Eqs. (1.1) and (1.2) to

$$\frac{\partial m}{\partial t} v_{\text{exit}} = m \frac{\partial v}{\partial t} \tag{1.3}$$

and then integrating over time, while assuming that v_{exit} is constant, produces the famed rocket equation,

$$\Delta v = v_{\text{exit}} \ln \frac{m_0}{m_f} \tag{1.4}$$

which can be rearranged to be

$$\frac{m_f}{m_0} = e^{-\Delta v / v_{\text{exit}}} \tag{1.5}$$

Then, for missions with a specified Δv requirement, a higher propellant exit velocity allows for the final mass, m_f, to be a greater proportion of the total initial mass, m_0. Since the final mass is the mass of the spacecraft minus the propellant mass, maximizing the ratio of the final to initial mass increases the amount of mass that can be allocated for scientific equipment or other valuable payload. For every space mission, there is an optimal exit velocity, or in a more commonly used form, the specific impulse. The specific impulse, I_{sp}, is the ratio of the thrust to the propellant weight flow rate,

$$I_{sp} = \frac{\dot{m} v_{\text{exit}}}{\dot{m} g_0} = \frac{v_{\text{exit}}}{g_0} \tag{1.6}$$

where g_0 is the sea-level gravitational acceleration, 9.81 m/s^2. Chemical rockets typically have specific impulses in the hundreds of seconds. Electrothermal thrusters have specific impulses typically ranging from the low hundreds to around one thousand seconds. Electromagnetic thrusters offer specific impulses in the thousands of seconds. Electrostatic thrusters are able to achieve specific impulses in the thousands of seconds and possibly even tens of thousands of seconds.[101]

There are a few issues regarding the integration of EP thrusters onto spacecraft. One concern is with possible exhaust plume interaction with spacecraft surfaces. With Hall thrusters, for example, plume plasma may impinge on external surfaces and cause material degradation.[19] This can occur due to either high-energy ions with a relatively large divergence angle or from back-flowing charge-exchange ions. Sputtered material from internal or external surfaces may also become deposited on other spacecraft components. Either case would reduce the effectiveness or even completely impair the use of solar panels, scientific instrumentation, and other sensitive devices. Hall thruster erosion studies aid in the understanding of the rate of internal sputtering and the trajectory of sputtered products.

Another issue is power generation. A spacecraft needs to provide enough electrical energy to power these devices, thus means to generate, store, and process power are required. The increased power requirements can mean larger solar arrays, radioisotope thermoelectric generators (RTG), or possibly even nuclear reactors and other alternative sources of power, may be required along with larger and heavier batteries or capacitors for energy storage. Power processing units (PPU) are not insignificant units of hardware as well in terms of size, mass, and complexity. The electrical support equipment all require sufficient engineering for proper functionality, spacecraft integration, and ensured durability and robustness to withstand the space environment. Of course, they also contribute additional mass that needs to be launched.

Limitations on the available power lead toward a corresponding limitation of thrust since more power is needed to produce greater thrust. Other factors that play a role in limiting the thrust density for these thrusters include space-charge limitations for electrostatic devices—a concern for ion thrusters, but not Hall thrusters—as well as structural, material, and other engineering concerns. Though EP can offer specific impulses that are orders of magnitude higher than chemical rockets, the associated thrust is often orders of magnitude lower. Figure 1.1 displays various propulsion means and their range of specific impulse and thrust.[101] EP is currently more commonly relegated to secondary propulsion duties requiring lower thrust such as satellite station-keeping and orbit raising, but it is increasingly being considered as a viable means of primary propulsion, especially for travel within the solar system where its specific impulse range is optimal. Past missions utilizing EP as primary propulsion include the Deep Space 1, and Dawn probes from NASA and the Hayabusa probe from the Japanese Aerospace Exploration Agency (JAXA). These three space probes traveled to asteroids and comets using ion thrusters as their primary propulsion system. The SMART-1 probe, developed by the European Space Agency, utilized a Hall thruster as its primary propulsion source to travel to and enter orbit around the Earth's moon. With a lower thrust, EP devices need to operate for a long period of time to achieve the necessary Δv of the mission. The lifetime requirements can reach into the thousands and tens of thousands of hours. Ensuring a long enough lifetime becomes a non-trivial task and is one of the main motivating factors behind this thesis.

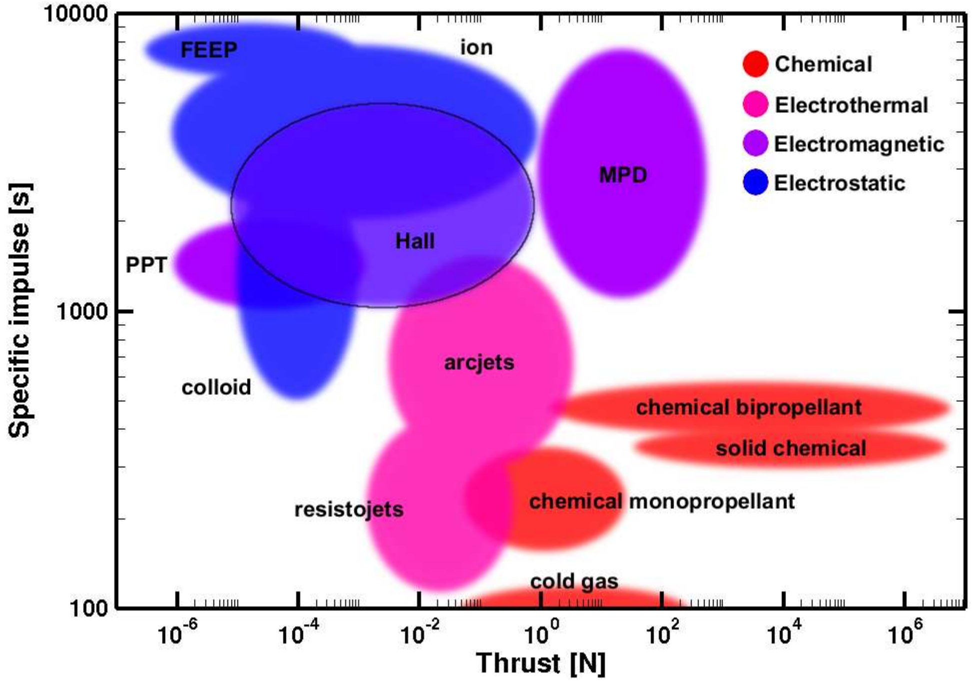

Figure 1.1: Thrust and specific impulse ranges for various forms of propulsion.

1.3 Hall Thrusters

Hall thrusters are a category of electric propulsion devices that originated in the 1950's and 1960's in both the United States and the former Soviet Union. Though interest in Hall thrusters waned in the US during the 1970's and 1980's, Russian work continued to advance the development of these devices. After the first operational use of a Hall thruster in space, the SPT-60 in 1972, over 100 thrusters have been flown on satellites.[121] Hall thrusters have mostly been used for satellite station-keeping duties. Their near optimal specific impulse and thrust-to-power ratio have also led them to be used for orbit insertion as well. The current renewed interest in Hall thrusters is focused on further development of higher power and higher specific impulse devices that can be used for primary propulsion as well as dual-mode thrusters that are able to operate with varying output ranging from a low specific impulse, high thrust mode to a high specific impulse, low thrust mode.[27,67]

There are two main types of Hall thrusters, the stationary plasma thruster (SPT) and the thruster with anode layer (TAL).[28,58] The walls of the SPT are made of an electrically insulating material whereas the TAL has conducting walls. The details of the plasma physics within the discharge channel vary, and the TAL has higher electron temperatures and a shorter channel length as a result, but many of the basic ideas and principles governing the two types of Hall thrusters are the same. The SPT-type Hall thruster will be the focus of this thesis.

A very basic schematic of a generic SPT Hall thruster is shown in Fig. 1.2. The discharge, or acceleration, channel is typically annular in shape. At the upstream end of the channel is the anode, through which the neutral propellant gas is injected. Outside of the channel, downstream of the exit plane, sits a cathode. The cathode emits electrons, a portion of which goes to neutralize the outgoing ion flow while the rest travel upstream towards the anode. An applied magnetic field traps the electrons heading toward the anode and impedes their axial drift. This region of low electron mobility also establishes a self-consistent axial electric field arising from the voltage potential difference between the anode and cathode. The predominantly radial magnetic field is set by electromagnetic coils located around the channel. The electrons are then caught in crossed electric and magnetic fields, causing them to move azimuthally forming a Hall current, from which the thruster obtains its name. This region of the channel with high Hall current is where most of the ionization of the neutral propellant occurs. The ions are then accelerated by the axial electric field out of the channel. One of the defining features of a Hall thruster is that the applied magnetic field is set such that electrons are highly magnetized and constrained to the magnetic field, while the ions are effectively unmagnetized within the length scale of the thruster and their motion is virtually unaffected by the magnetic field. One of the design philosophies for Hall thrusters is to increase the residence time of the electrons within the channel, to improve the propellant utilization efficiency, while accelerating the ions unimpeded to increase the specific impulse. So in this sense, Hall thrusters can be considered to be electrostatic since the thrust is generated primarily by electrostatic means, though the magnetic field plays such an important role in the physics of the plasma flow that Hall thrusters can also be

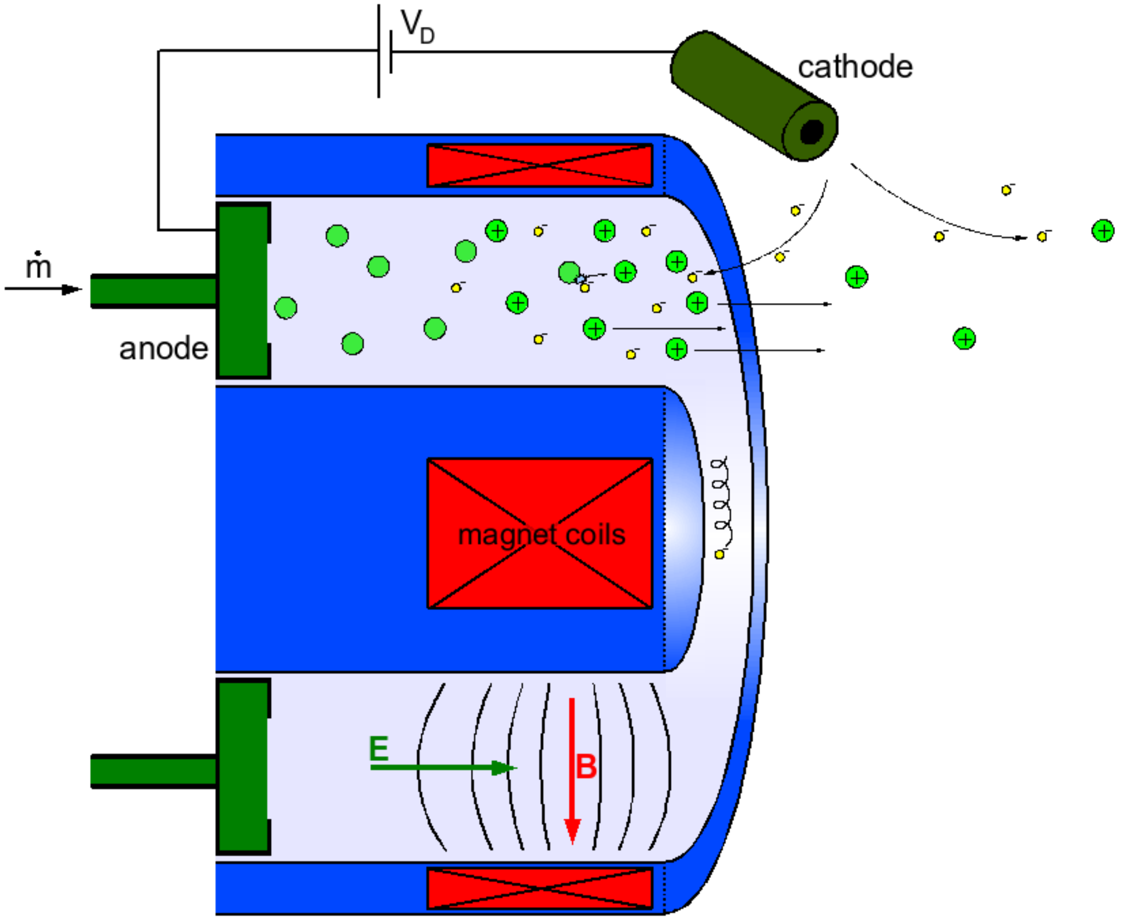

Figure 1.2: A basic schematic of a Hall thruster highlighting several key aspects.

considered to fall in the electromagnetic category.

Hall thrusters typically have a specific impulse in the low thousands of seconds, though there are ongoing efforts to increase it. Typical values of thrust are in the hundredths to tenths of newtons. Due in part to these low thrust values, mission requirements for Hall thruster lifetimes can reach into the thousands and tens of thousands of hours. Thus, lifetime prediction and validation becomes an important part of the thruster design and development process.

1.4 Hall Thruster Channel Wall Erosion

There are several different failure modes that can limit the lifetime of Hall thrusters. Erosion of the cathode from ion bombardment, evaporation of the thermoemitter and heater materials from high temperature, degradation of insulating and structural materials from space conditions, and deformation and cracking from thermal shocks are a few possible methods of failure.[29] The main accepted method of thruster failure, however, is the erosion of the discharge channel walls. As ions are accelerated downstream, some of them impact the walls with enough energy to sputter the wall material. Eventually this gradual erosion reaches the point where a part of the walls is completely eroded through and exposes the magnetic circuit and other sensitive parts of the thruster to the plasma flow. Figure 1.3 is taken from experimental work performed by Absalamov *et al.* on the channel wall erosion of an SPT-100 thruster.[2] The inner and outer wall profiles are shown with the anode towards the left side of the figure and the exit plane of the thruster to the right. Though the width of the channel is not drawn to scale, it is still clear that a significant amount of erosion occurred in a relatively short time. The outer wall, with an initial 5 mm thickness, has been completely eroded through at the exit plane after only 1000 hours of operation.

Depending on the mission specifications, months and even years of continuous thruster operation may be required which translates into lifetime requirements of thousands and tens of thousands of hours. Demonstrating such long life capability in an experimental trial and error manner is very time consuming and costly. An straightforward life demonstration takes months of continual operation. In addition, Hall thrusters require vacuum conditions for operation, and operating a ground-based vacuum tank for extended periods of time is not a trivial or inexpensive task. Operational interruptions, both planned and unplanned, disrupt tests and add additional time needed to complete life testing. Maintenance of the tank, seals, pumps, and instrumentation needs to be considered, as does a continual supply of propellant gas and electrical power to the thruster, which all add to the costs of such undertakings. The cost of xenon is roughly

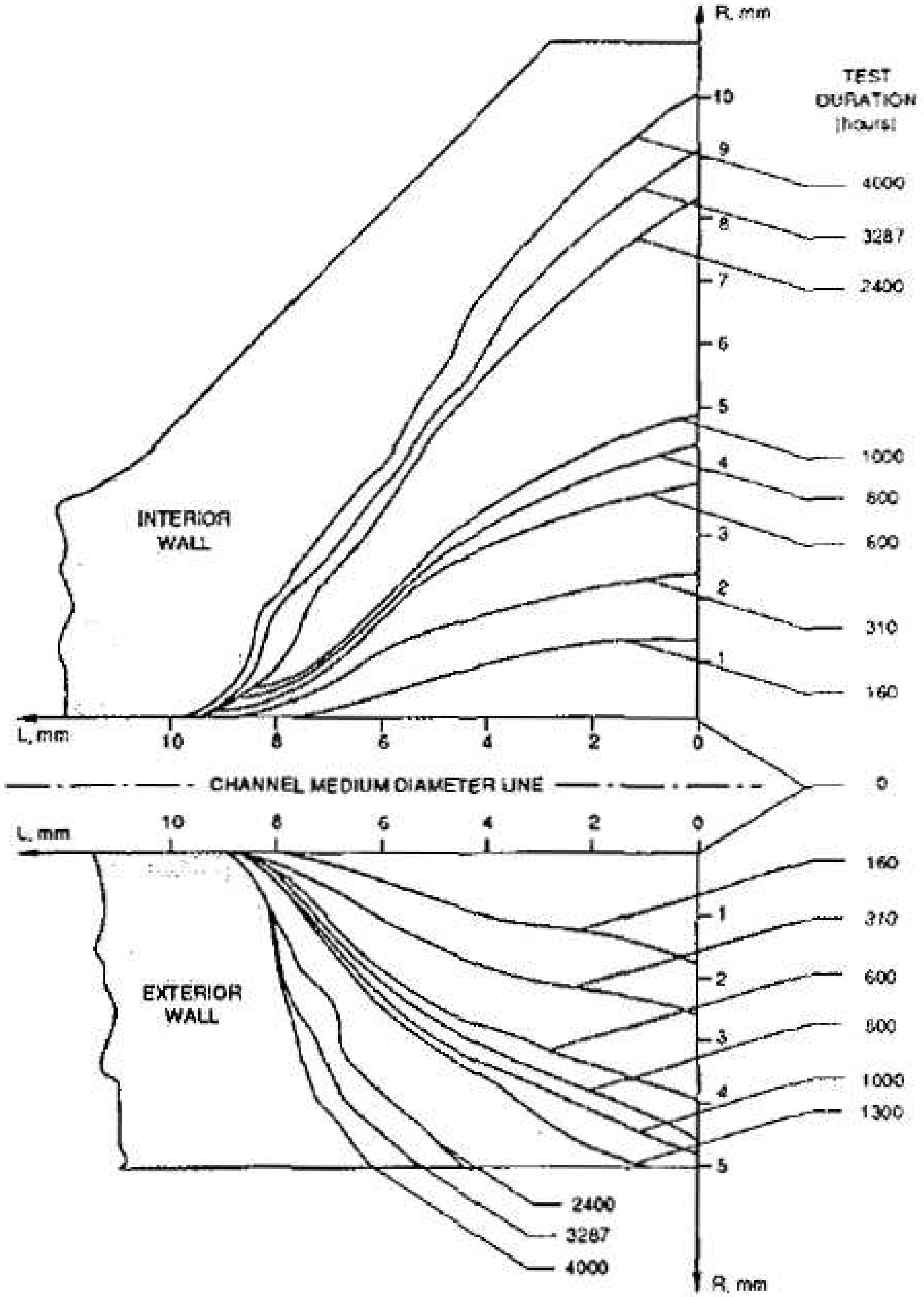

Figure 1.3: Experimentally observed wall erosion profiles for the SPT-100 thruster.[2]

$1140 per kilogram.[61] For propellant flow rates around 5 mg/s, more than $20,000 are required per 1000 hours of operation in propellant costs alone.

The benefits of a modeling effort to characterize erosion include a significantly quicker and less costly means to generate erosion results. Models also have the capability to test a variety of different thruster geometries and operating conditions. There will be a continual need for experimental erosion testing, in part to validate the accuracy of model results, but models and simulations are useful tools that contribute a substantial benefit towards characterizing Hall thruster channel wall erosion.

The erosion of the channel walls may have other effects beyond lifetime considerations as well. Performance characteristics may be affected by changes to the thruster geometry. Beam divergence increases since the ions are able to exit at larger angles from the channel centerline; this has been observed experimentally.[2,80] However, measurements of thrust over extended periods of time seem to indicate fluctuations of less than ten percent of the total thrust are observed.[9,30,42] Erosion of the channel walls can also lead to redeposition of the sputtered wall material either back in the thruster or perhaps onto other parts of the spacecraft, including sensitive instrumentation. Proper characterization and modeling of the erosion process would be helpful in analyzing these other effects of thruster erosion in addition to lifetime prediction.

A common material that is used for SPT-type Hall thruster channel walls is boron nitride (BN) or a BN compound. Boron nitride offers a number of excellent characteristics that make it attractive for use in space applications. It is fairly chemically inert and a good electrical insulator. Boron nitride also has a high melting temperature and high thermal conductivity.[73,106] The cubic allotrope (c-BN) has extreme hardness, second only to diamond, and is a material under much research to improve fabrication quality and quantity.[82,106] For Hall thrusters, however, the hexagonal allotrope (h-BN) is used in part due to its easy machinability. The work in this thesis will focus on h-BN as the wall material and particularly its sputtering due to xenon ion impacts.

1.5 Thesis Outline

The main topic of this thesis is the development of models useful for simulating, analyzing, and predicting the erosion of the Hall thruster channel walls. Chapter II covers an overview of past and current modeling approaches in a few areas including Hall thruster plasma physics modeling, wall material sputter modeling, and comprehensive erosion simulations and other lifetime assessment models. Chapter III describes the hydrodynamic model that is used to describe the plasma flow and ion flux to the walls. This work is the only known fluid-based plasma model used for Hall thruster erosion studies. Chapter IV details the molecular dynamics method used to simulate the sputtering of the wall material due to ion impacts. This work is the only known application of a full molecular dynamics model for boron nitride sputter yield calculations. This is also the first presentation of sputter yield data of boron nitride for xenon ion energies below 80 eV. Chapter V analyzes the applications of the hydrodynamic simulation to compare the effects of krypton versus xenon propellants in the NASA-173Mv1 thruster, the molecular dynamics simulation to calculate boron nitride sputter yields at low xenon ion energies, and an erosion simulation combining the two methods to model a 4000 hour life test of the SPT-100 thruster. For all three case studies, the computational results are compared to available experimental data. Chapter VI summarizes the findings and highlights areas that may warrant further examination.

CHAPTER II

Erosion Modeling

2.1 Overview

The erosion of the Hall thruster acceleration channel walls is a slow process. Often thousands of hours of operation at full power are necessary to erode the walls to the point where the magnetic circuit is exposed to the plasma flow. Full characterization of the erosion in an experimental manner requires long operation times of ground-based vacuum chambers that incurs high costs. To ameliorate these time and cost issues, a number of methods that model the thruster lifetimes have been proposed. These models range from semi-empirical extrapolations of experimental results to sophisticated particle methods that simulate the plasma flow and sputtering processes. The goal of this work is to continue the development of methods that are useful towards predicting the lifetime of Hall thrusters through accurate modeling of the erosion process.

Apart from the various semi-empirical models of the thruster lifetime, most of the methods developed to analyze the erosion of Hall thruster channel walls can be considered to consist of two components. One is a description of the plasma flow within the thruster, with the aim of determining the ion flux to the walls. The other is a relation of the incoming ion flux to the walls to the resulting sputter yields, which are then translated into erosion rates. A sample procedure to estimate the erosion and lifetime would be to iterate through calculations of the ion flux to the walls, the resulting sputter yields and erosion rates, and the updated wall profiles as they erode away.

The work presented in this thesis focuses on using a hydrodynamic method to model the plasma flow and subsequent ion fluxes to the walls, and a molecular dynamics method to simulate a sputtering boron nitride surface undergoing xenon ion impacts. The full details of the hydrodynamic model and the molecular dynamics model are presented in Chapters III and IV, respectively. The rest of this section gives an overview of the various approaches that can be taken for modeling Hall thruster wall erosion. Further development of each of these models, in conjunction with continued experimental testing and flight validation, will lead toward a more comprehensive understanding of the erosion process and how it can be most accurately or usefully characterized.

2.2 Semi-Empirical Models

The simplest lifetime model consists of fitting a regression curve to experimental erosion data.[11,56] For example, the total volumetric erosion rate of a Hall thruster is shown in Fig. 2.1. A two-mechanism process for erosion has been proposed, where one mechanism for erosion may dominate early on but diminishes over time until a second process take precedence.[79] Alternatively, a logarithmic dependence can be used to explain the experimental trend.[90] These extrapolations, while useful for quick back-of-the-envelope calculations, are specific to a particular thruster with a particular operating condition. More general lifetime prediction models can incorporate dependence on various thruster parameters such as thruster geometry, discharge voltage, and wall material sputter yields among others.[1,10,29,75,79] These models often provide more of a physical underpinning by utilizing first-order approximations of the plasma flow along the channel and considering energy and angular dependence of sputtering, but still depend to a large degree on experimental data. These semi-empirical models reduce the need for a full extended life test of a thruster and can make estimations of the erosion profiles and thruster lifetime from a more limited set of experimental data.

Though semi-empirical models provide quick and simple ways to make predictions of erosion and lifetime, they do not easily lend themselves towards thruster design purposes. These models may offer rough estimates for thrusters of a slightly different geometry

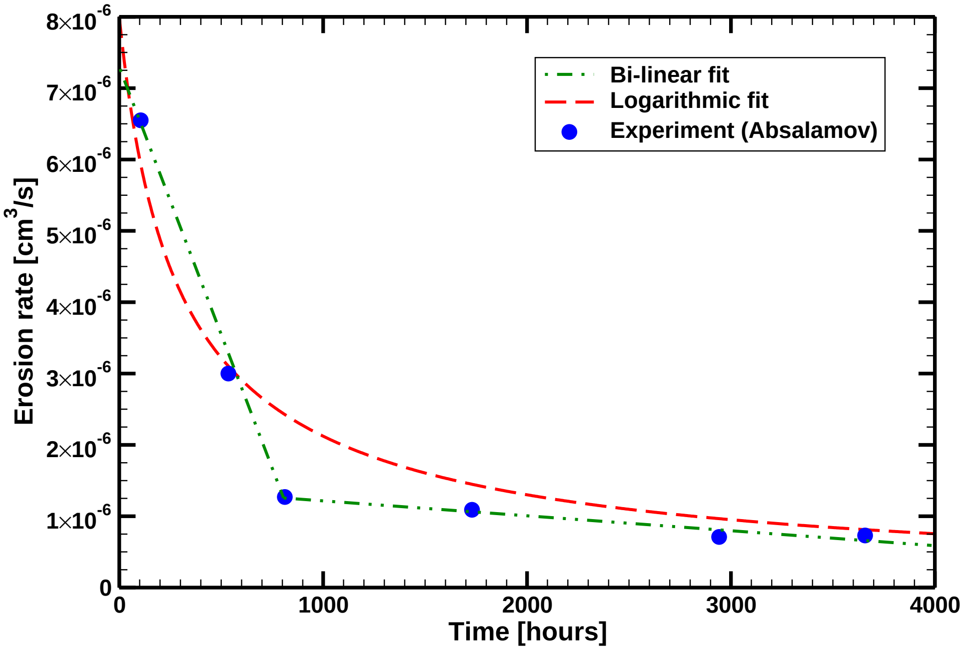

Figure 2.1: Sample empirical fits applied to experimental total volumetric erosion rate data.[2]

or operating conditions, but they are not entirely reliable for different configurations since these models by their nature depend on experimental observations that are often device specific. Models developed from an entirely physical basis or even from first principles would allow for greater confidence when applied to different thrusters and operating conditions. These models would still likely require some amount of calibration to experimental results, but not to the extent of semi-empirical methods.

2.3 Plasma and Wall Flux Models

Plasma modeling is a vibrant area of research in many different fields and with a wide range of applications. Apart from space electric propulsion, plasmas are modeled in other research contexts such as fusion energy generation, semiconductor processing, and space environment simulation. Many different methods and approaches have been developed over the years. For the application of Hall thruster discharge simulations, however, the focus has been directed along two main approaches, whether the ions are modeled either as a fluid or as particles.

The desired goal of a plasma model in the context of erosion simulations is to calculate the ion fluxes to the walls. Different approaches have been proposed to find the ion flux to the walls including empirical fits from ion current density profiles or beam divergence as well as assuming a scattering mechanism due to collisions.[10,77] The axisymmetric versions of fluid and particle methods calculate the flux to the walls through proper application of boundary conditions that often includes modeling of the sheath region between the bulk plasma and the walls.

2.3.1 Fluid-Based Methods

Fluid methods model the ions and other species based on governing conservation equations. These conservation equations are derived by taking moments of the Boltzmann equation assuming a Maxwellian distribution of the velocity and energy distribution functions. For traditional fluid dynamics, a Maxwellian distribution is obtained through sufficient collisions to establish local thermodynamic equilibrium. The flow of ions in a Hall thruster is nearly collisionless since their mean free path is on the order of the channel length—calculated parameters for an SPT-100 thruster are shown in Table 2.1[88]—so a Maxwellian distribution resulting from a sufficiently high collision rate cannot be assumed. The fluid approximation, however, is not necessarily a poor representation for the ions and neutrals. The propellant gas injected at the anode face likely has a Maxwellian distribution and there are few mechanisms that would alter that distribution within the channel. The location of ionization and subsequent remaining potential drop will affect the velocity distribution of ions as will any charge-exchange collisions with neutral atoms. These concerns are minor, however, in comparison to the electron dynamics within the thruster. Since the electron Larmor radius, or gyroradius, is much smaller than the characteristic length of a Hall thruster channel, their dynamics are more complex than the mainly electrostatic acceleration the ions undergo. The electron dynamics play a significant role in establishing the potential profile within the thruster and the electron temperature affects many plasma parameters. Electron populations

Parameter	Value
Channel length	25 mm
Channel width	20 mm
Plasma density	10^{15}–10^{17} m^{-3}
Ion mean free path	1–5 m
Ion gyroradius	0.5–1 m
Electron gyroradius	1–10 mm
Electron Debye length	0.05–0.1 mm

Table 2.1: Length scales for an SPT-100 thruster.

arising from ionization events and from secondary electron emission from the walls may also affect the plasma flow within the thruster that are not perfectly captured by a single electron population fluid model. There is still much ongoing research in the area of Hall thruster electron dynamics, but modeling the electrons as a fluid is presently the prevailing method as it offers fair representation of the electron dynamics with a reasonable amount of computational expense.

One of the main advantages of fluid-based methods is that they offer much quicker calculations than particle-based methods. It is for this reason that a fluid-based method is chosen to represent the plasma flow and to calculate the ion fluxes to the walls. One of the motivations for this work is to develop a tool that would be useful for the Hall thruster design process. Thus, a quick turnaround for the calculation of results is attractive. There is a wide array of fluid plasma codes for Hall thrusters that have been developed.[5, 13, 59, 60, 84, 94] Fluid models can range from one-dimensional to quasi one-dimensional, incorporating sheath and wall effects, to axisymmetric in the nature of their simulation domains. The models can converge to a steady-state solution or can produce time-dependent flowfields. Different solution methods are also employed to solve the discretized governing equations including finite-difference, finite-element, and finite-volume. The fluid model presented in this work, the hydrodynamic model described in Chapter III, employs a two-dimensional axisymmetric finite-volume method.

2.3.2 Particle-Based Methods

Particle methods model the ions and neutral atoms as particles. Occasionally the electrons are modeled as particles as well.[102] As described in the previous section, the electron dynamics within a Hall thruster are complex and difficult to model with full accuracy. Modeling the electrons as particles is an approach that offers the ability to capture the electron dynamics in a more robust behavior since it can include different electron populations. However, due to the very low mass of electrons, the timestep required to resolve their dynamics is prohibitively small. Even artificially increasing the electron mass or the permittivity of free space to allow for larger timesteps does not greatly alleviate the computational expense of modeling electrons as particles.[102] The prevailing trend recently is to model the electrons as a fluid while keeping a particle representation for the ions and neutral atoms in a hybrid approach.[38] These hybrid models offer a significant speed improvement over the fully particle schemes, since the simulations do not need to be run at the electron time scale. However, hybrid methods inherit the same issues involved with modeling the electrons as a fluid as do fully fluid methods described in the preceding section.

Particle-based methods are based upon reconstructing the Boltzmann equation, or for the collisionless case, the Vlasov equation, through the appropriate particle distributions to represent the ions and neutral atoms. The prevailing method in use, presently, is Particle-In-Cell (PIC), which is a particle-particle method. Simulated macroparticles, often representing a very large number of physical ions, are accelerated according to a potential field that is evaluated on a mesh. Other approaches, including particle-cluster methods, such as treecodes,[12] or cluster-cluster methods, such as the fast multipole method,[47] have not yet been widely used for Hall thruster simulations, though a treecode method has been developed for ion thruster optics simulations.[37] Further work continues to build upon the hybrid PIC model framework incorporating greater detail through the handling of the electrons, the sheath, and other aspects of Hall thruster physics.[49,63] Hybrid PIC models have also begun to incorporate preliminary erosion modeling as well.[3, 44, 52, 98]

The total wall clock time required to compute an erosion simulation depends on many factors. The size of the domain, how finely the domain is discretized, how many particles are simulated, the length of a timestep, the relaxation time for a simulation system to reach steady state, how many times a system is sampled, and the desired length of total simulation time are some of the factors that influence the time required to acquire simulation results. In general, however, fluid methods are significantly faster, often requiring seconds to minutes to achieve a solution for a particular domain. Hybrid particle methods, where the electrons are modeled as fluids, can require many hours, from six to twenty-four,[63] to achieve a solution, and fully particle methods will need even greater amounts of time, up to days and weeks.[102] This is compounded for erosion simulations, since a series of evolving domain geometries will need to be modeled sequentially to capture the effects of thousands of hours of erosion. Thus, fluid simulations can require more than an hour for a full erosion simulation, while particle methods may require days or even weeks of simulation. From a design perspective, a quicker approach is more attractive and thus is one of the main motivations behind choosing a fluid model for the erosion work presented in this thesis.

2.4 Sputtering Models

Once the fluxes of ions to the walls have been modeled, their effect on the resulting sputter yields needs to be found in order to be useful for erosion and lifetime analyses. Often a relation between the volumetric sputter yield and the ion current is formed. The sputter yield is dependent on the wall material, the ion species, the ion energies, and the incident angles. At higher ion energies, experimental data are not too difficult to obtain for most materials. However, for low ion energies, especially near the sputter threshold value, obtaining accurate measurements of sputter yield data presents challenges. For Hall thrusters operating with about a kilowatt of power, or discharge voltages in the hundreds of volts, a majority of the ions impacting the walls will be in this low-energy region where sputter yield data are scarce. Models are required to reconstruct the data in this region. These range from empirical extrapolations to first-principles analysis tools. Many of these models are based on the sputtering mechanisms and background analytical work performed by Sigmund.[96,97] This work has also been extended to multicomponent materials, which is of interest here.[15] Apart from the semi-empirical and analytical models, two particle methods, the binary collision approximation and the molecular dynamics methods, are highlighted here due to their use in sputter modeling.

It is important to model the sputter yield as accurately as possible since it has a significant impact on the resulting erosion predictions. Figures 2.2 and 2.3 show the effects on the beginning-of-life erosion rates under identical conditions except for the sputter yield curve fit and the assumed sputter threshold energy, respectively.[116] For this reason, the molecular dynamics approach is chosen as the main sputter modeling method for this work. Though it is more computationally intensive than the other methods, accurate results are the main goal, so it is desired to reduce the number of assumptions as much as possible. Since the sputter data only have to be calculated once

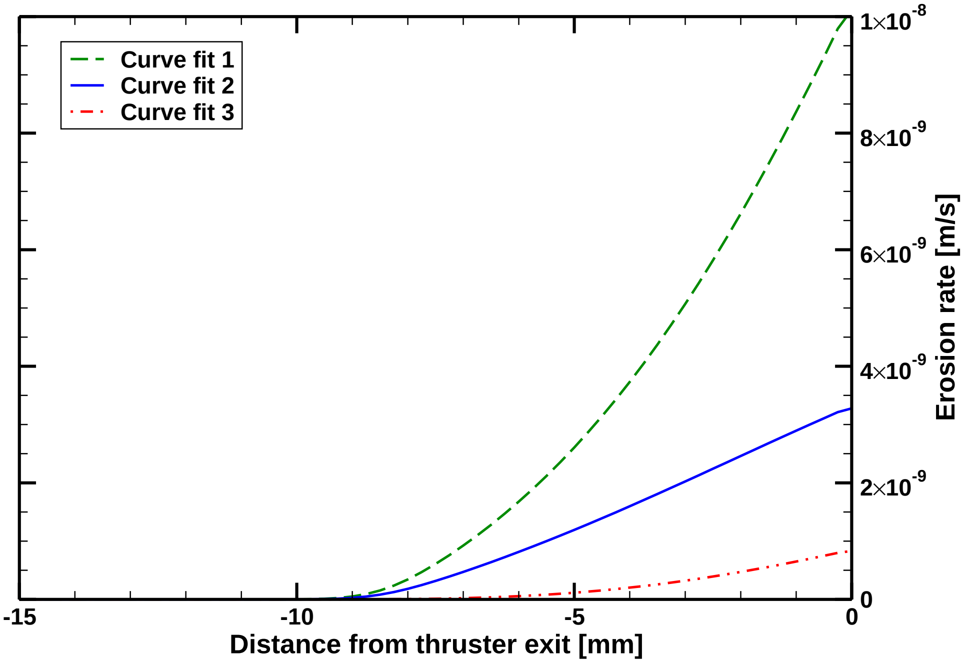

Figure 2.2: Calculated erosion rates using different sputter yield curve fits.

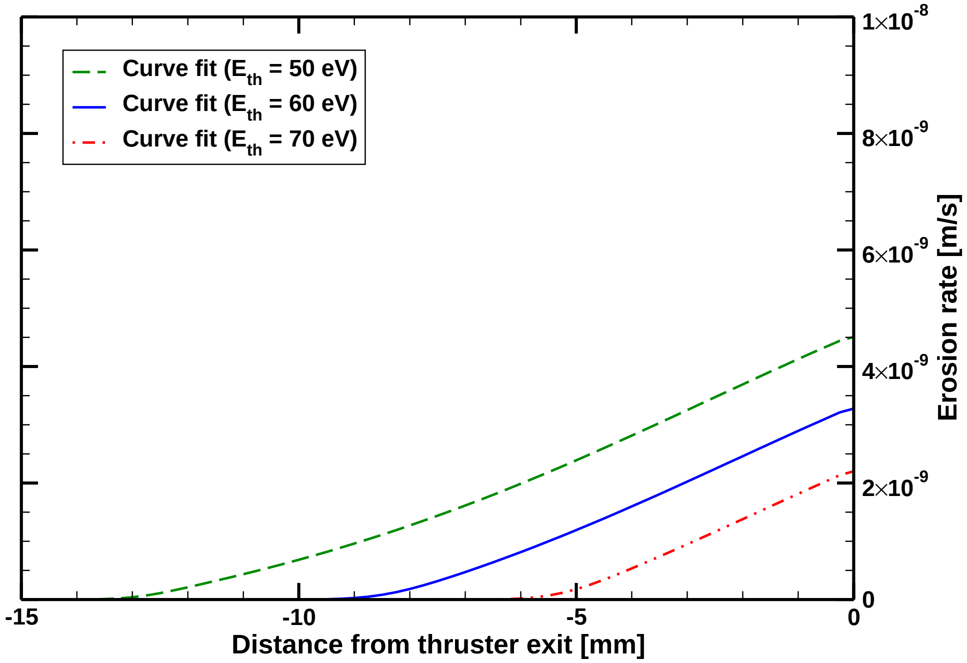

Figure 2.3: Calculated erosion rates using different threshold energies.

for a material and then can be used repeatedly in the erosion models, the computational time required is of less importance.

2.4.1 Empirical Models

The simplest approach towards estimating sputter yields is to develop and then extend trends observed from available experimental data points. For the material of interest in this work, boron nitride, a linear fit is suggested for experimental results obtained by Garnier *et al.* for xenon ion impingement taken for the range 350 eV to 1000 eV.[43] At lower energies, experimental data are scarce, so extrapolations are necessary. A logarithmic fit is suggested to provide a trend for energies approaching an estimated threshold value.[77] For an energy threshold of 60 eV, a proposed logarithmic fit to the Garnier data at normal incidence is

$$Y = 0.0156 \ln E - 0.0638 \tag{2.1}$$

which is valid for ion energies, E, up to the keV range. For the angular dependence of sputtering, polynomial curve fits are often used.[41,43,77] A quartic fit to the Garnier data for BN normalized by the value at normal incidence is

$$\hat{Y} = -4.45 \times 10^{-7}\theta^4 + 4.91 \times 10^{-5}\theta^3 - 9.72 \times 10^{-4}\theta^2 + 3.44 \times 10^{-3}\theta + 1.00 \qquad (2.2)$$

for angles, θ, in degrees. Multiplying the value of Eq. (2.1) by normalized value of Eq. (2.2) will provide an estimate of the sputter yield for a particular ion energy and incidence angle.

2.4.2 Semi-Empirical and Analytical Models

Semi-empirical models improve upon simple regression curves by incorporating elements of sputtering theory in the development of their formulae. Much of the theoretical analysis of the sputtering process was pioneered by Sigmund.[96] The derivation of the sputter yield is based on the random slowing down of particles through a collision cascade in an amorphous target material. At low energies—less than a few hundred volts—the sputter yield formula derived by Sigmund is[96]

$$Y = \frac{3}{4\pi^2}\frac{4m_i m_a E}{(m_i + m_a)^2}\frac{\alpha}{U_s} \qquad (2.3)$$

where α is a function of the mass ratio between the ion and target atom. For cases where the ion mass is much greater than the target mass, $m_i \gg m_a$, the value $\alpha \approx 0.15$ and Eq. (2.3) reduces to

$$Y = \frac{3}{\pi^2}\frac{m_a}{m_i}\frac{0.15}{U_s}E \qquad (2.4)$$

where U_s is the surface binding energy. Essentially, the relation between the ion energy and the sputter yield is found to be linear in this formulation. Sigmund asserts that sputter yields are linear down to somewhat below 100 eV for heavier ions, based on experimental measurements.[96] However, several assumptions behind the derivation of the formula may not hold at low ion energies, namely of the random slowing down, the binary collisions, and the calculations of the cross sections.[96] The surface binding energy is also not a readily available value for the target material. No first-hand data exist, though an approximation may be backed out of experimental sputtering results.

Sigmund also provides a more well known formula for the sputter yield from heavy ions at energies in the keV range,[96]

$$Y = 0.042 \frac{\alpha S_n}{U_s} \tag{2.5}$$

where S_n is the elastic stopping power for the ion and is dependent on the ion energy. Several researchers have tried to extend this formula into a more general form that would allow it to incorporate the threshold energy and therefore lower energy sputtering as well.[18,81] Bohdansky alters the Sigmund formula through modifications due to deposited energy and momentum distribution of recoil atoms and results in[18]

$$Y \approx \alpha S_n \left[1 - \left(\frac{E_{th}}{E}\right)^{2/3}\right] \left[1 - \frac{E_{th}}{E}\right]^2 \tag{2.6}$$

for low energy sputter yield calculations. Bohdansky also argues that energy dependence of S_n is small compared to the two bracketed terms on the right hand side of Eq. (2.6) and assumes S_n is approximately constant. The expression is fit to empirical sputter data of monatomic solids at low ion energies and normal incidence and generally shows good matching up to roughly ten times the assumed threshold energies.[18]

Matsunami *et al.* also modifies the Sigmund formula to incorporate the threshold energy, but has more interest in matching sputter yield trends over a larger range of energies, not just for the lower energy range. Through empirical matching of a large set of monatomic sputtering data, they also add a term similar to one that Bohdansky uses, but with an exponential of 1/2 rather than 2/3[81]

$$Y = 0.042 \frac{\alpha S_n}{U_s} \left[1 - \sqrt{\frac{E_{th}}{E}}\right] \tag{2.7}$$

Yamamura and Tawara perform further work on the Matsunami expression, expanding it to improve its accuracy with respect to high-energy, light-ion sputtering.[113] The Yamamura formula,

$$Y = 0.042 \frac{\alpha}{U_s} \frac{S_n}{1 + \Gamma s_e / s_n} \left[1 - \sqrt{\frac{E_{th}}{E}}\right]^s \tag{2.8}$$

incorporates the influence of the reduced electronic stopping power, s_e, through a factor Γ in relation to the reduced nuclear stopping power, s_n. This expression is used to provide fits to a large number of sputter data sets and generally show good agreement overall.[113] Several researchers have used a simplified form of this formula in Hall thruster erosion studies since some of the parameters, such as the surface binding energy, are unknown for boron nitride and other thruster wall materials. They reduce the Yamamura formula to

$$Y = AS(E)\left[1 - \sqrt{\frac{E_{th}}{E}}\right]^{2.5} \tag{2.9}$$

where the function $S(E)$ is represented as either[26]

$$S(E) = \frac{E^{0.474}}{1 + BE^{0.3}} \tag{2.10}$$

or as[3, 41, 52]

$$S(E) = \sqrt{E} \tag{2.11}$$

with A and B as fitting coefficients.

Zhang and Zhang also derive a sputter yield formula based on the work of Matsunami and Yamamura. Their work is focused more on obtaining differential sputter yields, but an expression for the total sputter yield is obtained by integrating over the solid angles,[118, 119]

$$Y = 0.042\frac{\alpha S_n}{U_s}\left[1 - \sqrt{\frac{E_{th}}{E}}\cos\theta\right] \tag{2.12}$$

where θ is the ion incidence angle from the surface normal. An approximate form of Eq. (2.12) can be used to fit to sputter yield data through

$$Y = As_n(E)\left[1 - \sqrt{\frac{E_{th}}{E}}\cos\theta\right] \tag{2.13}$$

where the nuclear stopping power is[122]

$$s_n(E) = \frac{\ln(1 + 1.1383E/\epsilon_0)}{2\left(E/\epsilon_0 + 0.01321(E/\epsilon_0)^{0.21226} + 0.19593(E/\epsilon_0)^{0.5}\right)} \tag{2.14}$$

$$\epsilon_0 = \frac{Z_i Z_a(m_i + m_a)(Z_i^{0.23} + Z_a^{0.23})}{32.53m_a} \tag{2.15}$$

with Z as the atomic numbers of the ion and target atoms. A and E_{th} are fitting coefficients for the Zhang formula.

In addition to energy dependence, research to fit the angular dependence of sputter yields has been performed as well. Going back to the work of Sigmund, an angular dependence for the normalized sputter yield is provided as[96]

$$\hat{Y} \approx (\cos\theta)^{-0.94} \tag{2.16}$$

which is nearly the well known inverse cosine law originally proposed from experimental observations of the angular sputtering dependence. This relation, however, is based on a Rutherford scattering assumption, which is typically more applicable to light ions. Equation (2.16) is also only valid for relatively low values of θ, the ion incidence angle from the surface normal. At more oblique angles, the inverse cosine is a poor fit.

Yamamura proposes an empirical law that accounts for the behavior at high incidence angles. For heavy ions, the following relation is proposed,[112]

$$\hat{Y} = (\cos\theta)^{A} \exp\left[-B\left(\frac{1}{\cos\theta} - 1\right)\right]\left[\frac{1-\sqrt{(E_{th}/E)}\cos\theta}{1-\sqrt{(E_{th}/E)}}\right] \tag{2.17}$$

where A, B, E_{th} are all essentially fitting coefficients. Yamamura also offers a simpler formula that is functionally equivalent to his light ion formula of

$$\hat{Y} = (\cos\theta)^{-A} \exp\left[-B\left(\frac{1}{\cos\theta} - 1\right)\right] \tag{2.18}$$

except for heavy ions, A is no longer a fitting coefficient, but depends on the threshold energy,

$$A = A'\left(1 + 2.5\frac{\sqrt{E_{th}/E}}{1-\sqrt{E_{th}/E}}\right) \tag{2.19}$$

There are still three fitting coefficients for Eq. (2.18) with A', B, and E_{th}.

All of the semi-empirical expressions given above are based on Sigmund's initial work and are tuned using experimental results given for particular ion-surface systems often providing good comparisons to those results. However, for the energy regime of interest for this work, at low ion energies approaching the threshold energy, there are a couple of concerns with using the above formulae. One main issue is the validity of the assumptions made for the Sigmund expression. Most of these semi-empirical expressions are based on Eq. (2.5), which is intended for use with heavy and medium mass ions in the keV range, instead of Eq. (2.3) which Sigmund derived for ions below 1 keV. Also, as mentioned before, some of the assumptions behind Sigmund's work do not necessarily hold at very low energies. These include assumptions of binary collisions and random slowing down. In addition, these fits are mainly compared against monatomic materials and the effect of multicomponent materials, such as boron nitride, are not as extensively studied. These issues should be kept in mind when applying these fits for use in a Hall thruster erosion simulation model.

A different model that is not based on Sigmund's work uses an approach based on quantum-statistical mechanics. This method provides an analytical approach based on first principles that can be used to describe sputtering systems.[107, 108] Probabilities of an atom being sputtered from the surface derived from quantum and statistical mechanics concepts are used to calculate a formula for the sputter yield. This approach is predicated on a three-body interaction assumption—where an ion impacts a surface atom and a second surface atom quasi-simultaneously, causing it to sputter. This quantum-statistical analysis assumes this mechanism to be the dominant mode of sputtering for impacts involving ions with low energies near the sputtering threshold value. This quantum-statistical approach is presumed to be valid for ion energies below 100 eV.

The basis of this approach lies in evaluating the probability that a surface atom will undergo being sputtered based on a three-body interaction process. Wilhelm derives an expression for the expected sputter yield,[108]

$$Y \approx \frac{1}{24} h_{2/1} \sigma(E_{th}) n^{2/3} \left(\frac{(m_a/m_i)^2}{1 + 2m_a/m_i} \right)^{3/2} \frac{(E - E_{th})^2}{E_{th}^2} \tag{2.20}$$

where S is the sputter yield, E and E_{th} are the energy and threshold energy respectively, $h_{2/1}$ is a dimensionless coefficient dependent on the perturbation operator of the Hamiltonian of the system between the initial and final states and their corresponding volumes, σ is the total scattering cross section, n is the number density of the atoms in the solid, and m_i and m_a are the mass of the ion and the target atom respectively. The theoretical sputter yield trends from this formula are compared to experimental results for monatomic polycrystalline materials.[108] Since all of the parameters required for Eq. (2.20) are not known, particularly for a multicomponent material such as boron nitride, only a qualitative form of the equation is used in this work for comparative purposes. Specifically, Eq. (2.20) is simplified to

$$Y \approx A(E - E_{th})^2 \tag{2.21}$$

where A is a fitting coefficient.

To provide a qualitative comparison of the various fit formulae, Fig. 2.4 displays sample normalized profiles with the same threshold energy. Two of the fits, the empirical logarithmic regression fit given in Eq. (2.1) and the Zhang expression of Eq. (2.13), show a monotonic concave curve. The Wilhelm quantum-statistical fit, from Eq. (2.21), is monotonically convex and the Sigmund low-energy formula, Eq. (2.3) is linear. Both of the Yamamura approximations, given by Eqs. (2.9)-(2.11), as well as the Bohdansky expression of Eq. (2.6) are convex near the threshold energy and go through an inflection point and end up from nearly linear to concave at higher energies. Another way to compare the profile shapes is to adjust the coefficients such that the slopes are similar at the normalization point, shown in Fig. 2.5. This type of comparison matches sets of data with that slope around that point. The more concave curves, the Zhang or the logarithmic, result in higher threshold values, while the more convex curves, the Wilhelm or Yamamura, provide lower threshold energies.

The expected true sputter yield curve is most likely convex towards the threshold energy, as the studies most focused on the very low energy regime, the Wilhelm and Bohdansky relations, show convex behavior at very low energies.[18,108] Asymptotic behavior towards the threshold energy is also sensible as microscopic surface conditions will vary to an extent where a gradual decrease in sputter yield is expected rather than a sharply

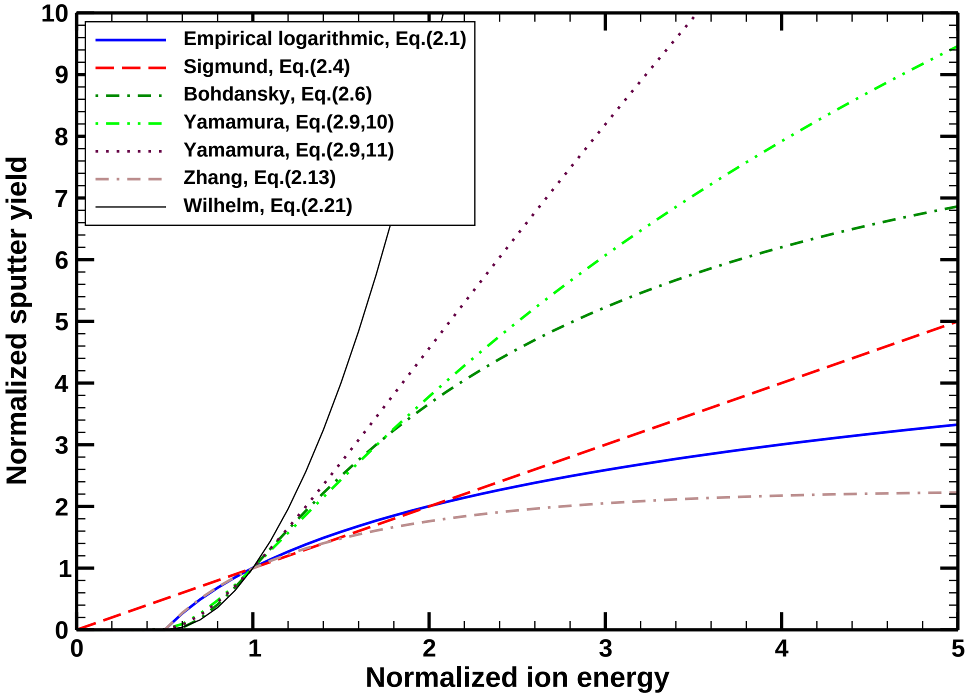

Figure 2.4: Normalized sputter yield fit profiles with the same threshold energy.

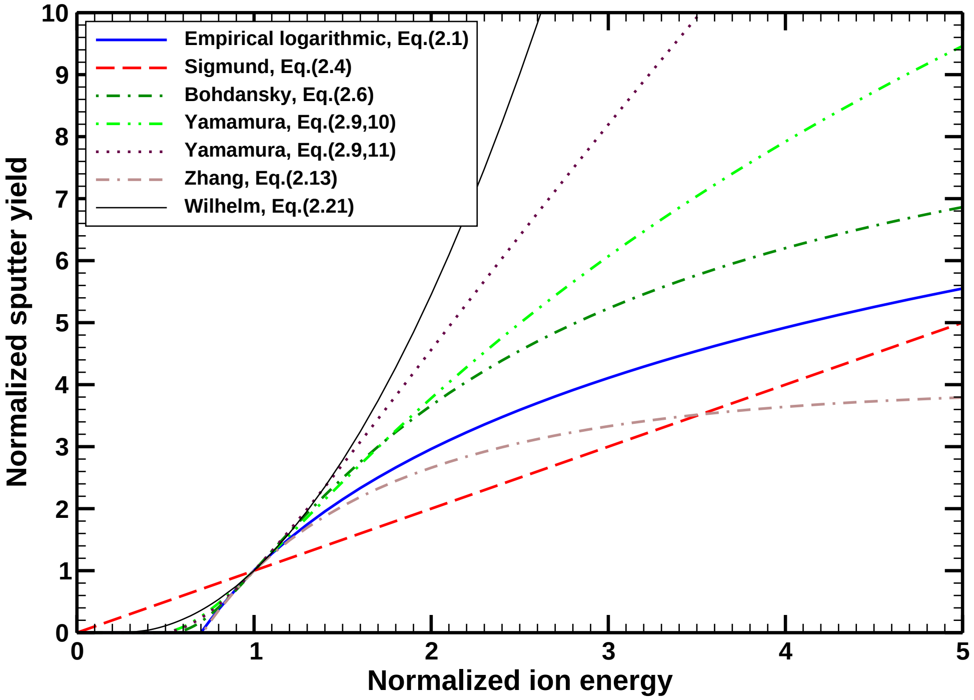

Figure 2.5: Normalized sputter yield fit profiles with the same matching slope.

defined cutoff point. At higher energies, a concave sputter yield profile is expected as per the analysis performed in the derivation of the Sigmund and related expressions. The concave nature of the sputter yield curve has also been observed many times experimentally.[112] Thus, a sputter yield with an inflection point is to be expected. The Bohdansky relation may prove to be a good single expression fit, though combination of fits may prove to be useful as well.

Figure 2.6 shows angular dependence fits normalized to unity at normal incidence and with equal peak values for profile shape comparison. As mentioned earlier, the Sigmund approximation, the near inverse cosine law given in Eq. (2.16), is only valid for low values of the incidence angle and is unsuitable for oblique angles. The two Yamamura fits, from Eqs. (2.17) and (2.18), have only minor differences between the two. They differ from the empirical quartic regression fit of Eq. (2.2) mainly in the behavior at glancing angles beyond roughly 70°. The Yamamura formulas show a quicker reduction in the sputter yield as the incidence angle increases in that region and is effectively zero beyond 85°. There are much less available data for sputtering yields obtained for glancing ion angles and the behavior is not as well understood in that region.

2.4.3 Binary Collision Approximation

A popular numerical modeling approach for sputtering studies is the binary collision approximation (BCA) method.[16,92] As per its name, this assumption considers only collisions between two atoms at a time. These binary collisions include either the initial ion and a target stationary atom or a moving displaced atom and a target stationary atom. The rest of the surface atoms are ignored. The paths of the incident ion, the primary knockon atom, and any subsequent secondary knockon atoms with sufficient energy are traced to observe the ion-surface interactions including sputtering. This method, in effect then, captures sputtering events arising from a linear collision cascade.

The binary collision approximation is implemented into Monte Carlo schemes to model the sputtering process. One example is the MARLOWE code, which models a

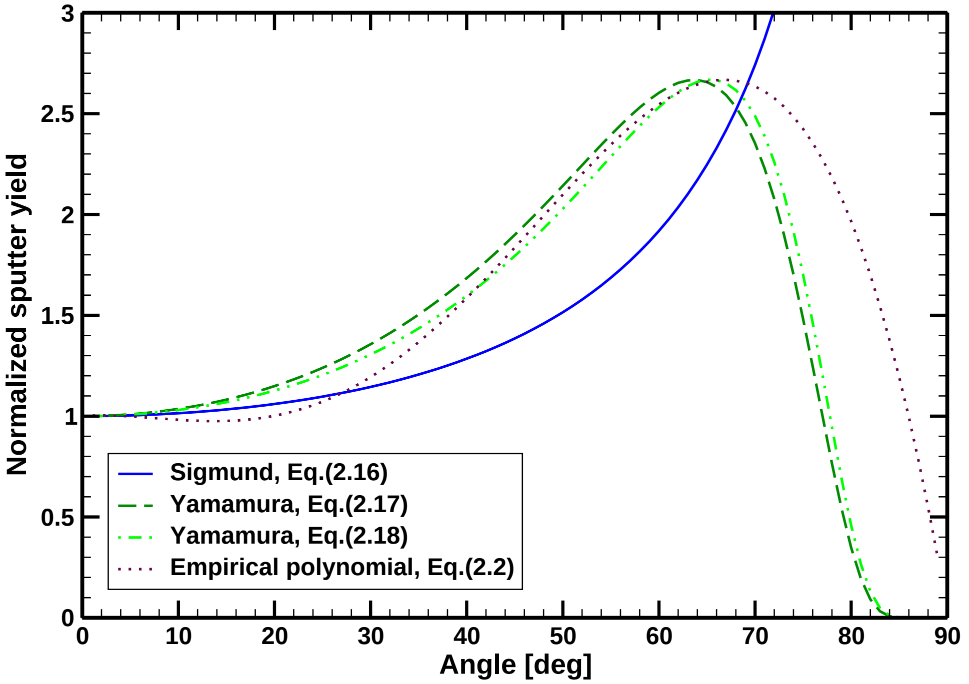

Figure 2.6: Normalized sputter yield profiles for angular dependence fits.

crystalline target material.[92] Another popular code is TRIM, which offers quick calculations of the sputter yield for amorphous target materials.[16] TRIM has been used in an electric propulsion modeling context, where it was applied to model the sputter yields of molybdenum from xenon ions for ion thruster optics erosion studies.[85] The TRIM results can be recalibrated by adjusting the surface binding energy parameter to match the experimental results, though it is unclear how well it performs at very low ion energies. It has also been utilized to model sputtering of other spacecraft materials for EP plume interaction and contamination studies.[20] Most of these studies are for monatomic materials, which was an initial assumption for the TRIM code. A modified version of TRIM that accommodates multi-component sputtering has been developed.[34] A sputtering study of boron nitride due to argon atoms has also been performed using TRIM from a boron nitride plasma processing standpoint.[25] A sensitivity study is performed by adjusting the surface binding energy parameter. Again, however, the data at very low ion energies are speculative and the trends for that regime are uncertain. There are no known uses of TRIM or any other Monte Carlo BCA code for xenon ions sputtering boron nitride.

Though good results have been obtained with the BCA method, one of the main drawbacks to these codes is the dependence of the sputtering results to the surface binding energy parameter, which is not clearly defined; sometimes this parameter needs to be fitted against experimental results. Another possible issue with the BCA-based sputter models is that they only capture sputtering due to a linear cascade of binary collisions. Under some circumstances, such as for very low ion energies, multi-body collisional interactions need to be taken into account. The sputtering of multi-atom molecules and compounds, or cluster sputtering, is also not considered within this approach.

2.4.4 Molecular Dynamics

Molecular dynamics (MD) is a deterministic particle simulation. The motion of each of the atoms in the system is governed by Newton's law of motion which is integrated forward through time. The forces acting on the particles are modeled through interatomic potential functions. Depending in part on the application of these potential functions, an accurate picture of the atomic interactions can be successfully simulated. The MD method has been used successfully in a wide variety of areas including sputtering simulations.[64, 66, 120]

The application of molecular dynamics to sputtering systems presents some challenges.[105] It involves highly non-equilibrium states where a large amount of energy begins in one particle, the ion, and is eventually dispersed among many surface atoms. A large range of interaction distances and energies need to be considered. The target sample surface needs to be large enough to account for the thermal considerations appropriately. The required timestep can be much smaller than the duration of a sputtering event and subsequent relaxation of the surface. Boron nitride as the target material also presents some challenges since it consists of more than one component species. Though there has been a prior attempt to model the sputtering of nitrides, including boron nitride, that work uses a potential function that is purely repulsive.[35,36,91] To compensate for the lack of any attractive forces among the atoms within the materials, a surface energy barrier is added. This approach offers little advantage compared to a BCA method since the sputtering is still dependent on the value of the surface binding energy parameter. The work performed for this thesis presents a full MD method for the modeling of boron nitride sputtering without any additional assumptions or caveats.

2.5 Summary

There are a variety of approaches that can be used to predict the lifetime of a Hall thruster. Empirical and semi-empirical models of thruster lifetimes are often fitted to a particular thruster or operating condition, but a proper lifetime analysis tool should have greater robustness and confidence in the results across a wide range of thruster designs and operational conditions. A full explanation and understanding of the processes involved with wall erosion is also desirable. Thus, an approach that has a more physical grounding is desired.

Presently, the most common approach towards erosion modeling involves a two-part method where a plasma model calculates the ion flux to the walls and a sputter model that calculates the resulting sputter yields. Hall thruster plasma models can largely be divided into two categories, fluid-based methods and particle-based methods. A fluid method, the hydrodynamic method described in Chapter III, is chosen as it offers much quicker turnarounds on producing erosion and lifetime results over particle methods. Though hybrid-PIC codes are currently one of the prevailing methods to model Hall thruster plasma flows, the area of greatest concern in modeling Hall thruster plasmas, the electron dynamics, is modeled in the same manner as fluid methods. Since the same issues with modeling the electron transport arise in both hydrodynamic and hybrid-PIC methods, the emphasis on the speed of the hydrodynamic model is used to choose that method for erosion modeling in this work.

For the sputtering model, the sputter yields only need to be calculated once. Once the sputter yield data are obtained, they can be used repeatedly in erosion simulations without the need to generate new sputter results. Therefore the speed of the method is not as great of a concern and the emphasis is placed on accuracy. In particular, the sputter yields at low ion energies is unknown for the materials of interest. It becomes difficult to obtain experimental sputter data at low energies since increasingly sensitive measurement techniques are required as the sputter yields decrease. Low energy sputter yields are important in determining the upstream location along the Hall thruster channel walls where erosion begins. At ion energies near the threshold energy, however, the assumptions for the semi-empirical models based on Sigmund's work and also for the particle codes based on the BCA do not necessarily hold. The Wilhelm approximation is derived specifically for ion energies near the threshold energy, but does not model the sputter yields well at higher ion energies. The MD method described in Chapter IV is chosen to model the sputtering since there are no assumptions that are invalid at either low or high ion energies.

CHAPTER III

Hydrodynamic Plasma Model

3.1 Governing Equations

The hydrodynamic model uses a fluid description to model each of the species in a plasma flow. Three species are modeled: singly-charged ions, neutral atoms, and bulk plasma electrons. Doubly and other higher charged ions are not yet represented by this model. Electrons emitted from the walls as secondary emission electrons are not explicitly modeled as a separate species, though they are incorporated in the calculations of sheath parameters. For each of the three species that are included, they are governed by their own set of conservation equations. The solution scheme of the overall method centers primarily around the ion conservation equations. The equations of the neutral atoms and electrons provide calculations of the plasma properties that are incorporated as source terms in the ion equations.

In a fluid description, conservation equations are used to characterize the properties of the flow. Usually these governing equations include conservation of mass, momentum, and energy. Beginning with conservation of mass, if a sample test volume, $\mathcal{V}$, is placed in the flow of interest, then the mass of the species in the volume changes over time due to the net effects of the inflow and outflow of the species into the test volume as well as any creation or destruction events occurring within the volume. This is represented clearly through the integral form of the continuity equation,

$$\frac{\partial}{\partial t}\iiint_{\mathcal{V}} \rho d\mathcal{V} = -\iint_{\mathcal{S}} \rho\vec{v}\cdot\vec{n}d\mathcal{S} + S_{\text{cont}} \tag{3.1}$$

The change in the density ρ of the species over time in a volume $\mathcal{V}$ is equal to the change in density due to the flow with velocity $\vec{v}$, passing through the surface $\mathcal{S}$ of the volume with normal vector $\vec{n}$, plus any source terms S_{cont}.

Similarly for the momentum equation, the change in momentum inside of a test volume is equal to the change in momentum flowing in and out of the volume as well as changes due to forces acting on the species—both external surface forces as well as internal body forces. The general integral form of the momentum conservation equation is given as

$$\frac{\partial}{\partial t}\iiint_{\mathcal{V}} \rho \vec{v} d\mathcal{V} = -\iint_{\mathcal{S}} \rho \vec{v}\vec{v} \cdot \vec{n} d\mathcal{S} - \iint_{\mathcal{S}} p \vec{n} d\mathcal{S} + \iiint_{\mathcal{V}} \rho \frac{\vec{F}}{m} d\mathcal{V} + S_{\text{mom}} \tag{3.2}$$

where the second term on the right hand side represents the change in momentum due to surface forces—here, viscous effects are ignored for the plasma and only pressure, p, is considered—and the third term represents the change in momentum due to body forces, $\vec{F}$. Any other means through which momentum can be altered may be represented by more source terms through S_{mom}.

Finally for energy conservation, the change in the specific internal energy, e_{int}, in a control volume over time is equal to the energy flowing in and out of the volume as well as source terms adding to or reducing the energy, this includes work performed by forces as well as heat sources and sinks.

$$\frac{\partial}{\partial t}\iiint_{\mathcal{V}} \rho e_{\text{int}} d\mathcal{V} = -\iint_{\mathcal{S}} \rho e_{\text{int}} \vec{v} \cdot \vec{n} d\mathcal{S} + S_{\text{energy}} \tag{3.3}$$

These equations also have a corresponding differential format. Two theorems of vector calculus allow for the transformation. The Divergence Theorem equates the surface integral of any vector to the volume integral of the divergence of that vector,

$$\iint_{\mathcal{S}} \vec{v} \cdot \vec{n} d\mathcal{S} = \iiint_{\mathcal{V}} \nabla \cdot \vec{v} d\mathcal{V} \tag{3.4}$$

The Gradient Theorem allows for a change from the surface integral of any scalar to a volume integral of the gradient of that same scalar,

$$\iint_{\mathcal{S}} p\vec{n}d\mathcal{S} = \iiint_{\mathcal{V}} \nabla p d\mathcal{V} \tag{3.5}$$

Using these two theorems, the integral conservation equations can be converted to their differential forms. The general differential form of the mass conservation equation is given by

$$\frac{\partial}{\partial t}\rho + \nabla \cdot (\rho\vec{v}) = S_{\text{cont}} \tag{3.6}$$

The differential form of the momentum equation is

$$\frac{\partial}{\partial t}(\rho\vec{v}) + \nabla \cdot (\rho\vec{v}\vec{v}) + \nabla p = \rho\frac{\vec{F}}{m} + S_{\text{mom}} \tag{3.7}$$

For the energy equation,

$$\frac{\partial}{\partial t}(\rho e_{\text{int}}) + \nabla \cdot (\rho e_{\text{int}}\vec{v}) = S_{\text{energy}} \tag{3.8}$$

The above differential equations, built upon basic conservation principles, are used to model each of the species in the plasma flow. Different properties and assumptions made for each species are used to tailor the conservation equations accordingly. Further details are described in the following sections.

3.1.1 Ion Conservation Equations

The ions are modeled using the axisymmetric forms of the conservation equations. A cylindrical coordinate frame is useful to describe the annular geometry of the acceleration channels for Hall thrusters. Symmetry of the flow about the thruster centerline is assumed so use of a full three dimensional description, with its associated increase in computational time and complexity, is not necessary.

The axisymmetric ion continuity equation, written in conservative form, is

$$\frac{\partial \rho}{\partial t} + \frac{\partial(\rho v_z)}{\partial z} + \frac{\partial(\rho v_r)}{\partial r} = \beta n_a \rho \tag{3.9}$$

Included as a source term on the right hand side of the equation is the creation of ions due to ionization events. This term includes β, the volumetric ionization rate, which is defined in Section 3.1.4.

For the momentum equations, a body force is present in the form of the Lorentz force, which describes the interaction of electric and magnetic fields on a charged particle. It is given as

$$\vec{F} = q\left(\vec{E} + \vec{v} \times \vec{B}\right) \tag{3.10}$$

For typical Hall thruster parameters, the magnetic field strength is set such that the electrons are magnetized while the ions are not. A rough gauge of the relative magnetization of a charged particle is its gyroradius, or the mean radius the particle orbits a magnetic field line. The gyroradius depends on the thermal velocity,

$$v_{\text{th}} = \sqrt{\frac{kT}{m}} \tag{3.11}$$

and the gyrofrequency, or the frequency with which the particle circles a magnetic field line,

$$\omega = \frac{eB}{m} \tag{3.12}$$

The gyro, or Larmor, radius can then be calculated as

$$r_L = \frac{v_{\text{th}}}{\omega} = \sqrt{\frac{mkT}{e^2B^2}} \tag{3.13}$$

Since the mass of an ion is several orders of magnitude greater than that of an electron, its gyroradius is also substantially larger. So for a certain range of magnetic field strengths, the gyroradius for the ions can be set to be larger than the length of the discharge channel while the gyroradius of the electrons is much smaller than the length of the channel. Then the Lorentz force can be considered to be reduced to a purely electrostatic acceleration for the ions.

Two components, the axial and the radial, of the ion momentum equation are considered. The conservative form of the axial component of the ion momentum equation is

$$\frac{\partial\left(\rho v_z\right)}{\partial t} + \frac{\partial\left(\rho a^2 + \rho v_z^2\right)}{\partial z} + \frac{\partial\left(\rho v_z v_r\right)}{\partial r} = enE_z + \beta n_a v_a \rho \tag{3.14}$$

For isothermal ions, the equation of state is $p = \rho a^2$ where a is the local acoustic speed. The first source term on the right hand side of Eq. (3.14) represents the force resulting from the axial component of the electric field, E_z. The second source term is a frictional drag force due to ionization collisions of the neutral atoms. The conservative form of the radial component of the ion momentum equation is

$$\frac{\partial\left(\rho v_r\right)}{\partial t} + \frac{\partial\left(\rho v_z v_r\right)}{\partial z} + \frac{\partial\left(\rho a^2 + \rho v_r^2\right)}{\partial r} = enE_r + \frac{\rho a^2}{r} \tag{3.15}$$

Here, the force due to the radial component of the electric field is represented in the source terms as well as a term that arises due to the axisymmetric nature of the formulation.

The energy conservation equation is ignored for the ions. The ion temperature is much lower than the electron temperature within Hall thruster dynamics and can be considered negligible.[4] Then through the cold ion assumption, the ion energy equation is not necessary anymore and can be eliminated, simplifying the set of governing equations.

3.1.2 Neutral Atom Conservation Equations

The neutral atoms are modeled as a one dimensional flow through the acceleration channel. Only the continuity and axial momentum equations are considered. They are similar in form to the corresponding ion equations and are given as

$$\frac{\partial n_a}{\partial t} + \frac{\partial\left(n_a v_a\right)}{\partial z} = -\beta n n_a \tag{3.16}$$

$$\frac{\partial\left(n_a v_a\right)}{\partial t} + \frac{\partial\left(n_a a^2 + n_a v_a^2\right)}{\partial z} = 0 \tag{3.17}$$

The source term for the continuity equation is negative since neutrals are depleted for ionization. The creation of neutral atoms due to ion recombination at the walls is low compared to the bulk population, around an order of magnitude lower, so it is ignored. No source terms are considered for the momentum equation.

3.1.3 Electron Conservation Equations

For the electrons, the continuity equation can be eschewed for a quasi-neutrality assumption as long as the simulation mesh lengths are larger than the electron Debye length. The bulk plasma within the channel is assumed to be electrically neutral. With only singly-charged ions considered in this model, this allows for the electron number densities to be set equal to the calculated ion number densities. The two remaining conservation properties, of momentum and energy, are not used to explicitly calculate the electron velocities or energies. Rather, the momentum equation is used to calculate the electric field while the energy equation is used to solve for the electron temperature.

The momentum equation for the electrons is given as

$$\frac{\partial}{\partial t}\left(\rho_e \vec{v}_e\right) + \nabla \cdot \left(\rho_e \vec{v}_e \vec{v}_e\right) + \nabla p_e = -en\left(\vec{E} + \vec{v}_e \times \vec{B}\right) - \frac{m_e m_h}{m_e + m_h} n \nu_e \left(\vec{v}_e - \vec{v}_h\right) \quad (3.18)$$

Apart from the Lorentz force, the source terms include a frictional force due to collisions with the heavy particles, both ions and neutral atoms collectively represented by the subscript h, that occur with a frequency of ν_e. The relative time scales of electron motion, as evidenced by the gyrofrequency in Eq. (3.12) for example, are much lower than that of the ions due to the low mass of the electron. In solving for the electric field profile, the primary concern is with the ion motion, thus it is assumed that the electrons are mobile enough on the ion time scale to reach a time-averaged equilibrium. In that case, the time-dependent term on the left hand side of Eq. (3.18) drops out. The electrons can also be considered inertia-less under this assumption. Then the second term on the left hand side is also neglected. Finally, the velocity term in the Lorentz force on the right hand side can also be ignored under the time-averaged assumption. The electrons are constrained to revolve around the magnetic field lines, but are free to move along the magnetic field lines. In a time-averaged case, then, the motion of the electrons around the magnetic field lines cancels out. The net motion will then be only along the magnetic field lines; this is also known as the guiding center motion. Since the guiding center moves in the same direction as the field lines, the cross product of the Lorentz force cancels out. Further simplification of the source terms is possible in the collisional drag term, since $m_h \gg m_e$ and $v_e \gg v_h$. The electron momentum conservation equation is reduced to

$$\vec{E} = -\frac{1}{en}\left(\nabla p_e - m_e n \nu_e \vec{v}_e\right) \tag{3.19}$$

Further manipulation of the formula using the equation of state,

$$p_e = nkT_e \tag{3.20}$$

and the definitions of electron current density,

$$\vec{j}_e = -en\vec{v}_e \tag{3.21}$$

and of electron mobility,

$$\mu_e = \frac{e}{m_e \nu_e} \tag{3.22}$$

leads to the following equation for the electric field,

$$\vec{E} = \frac{1}{en}\left(\frac{\vec{j}_e}{\mu_e} - \nabla\left(nkT_e\right)\right) \tag{3.23}$$

The calculation methods to obtain the electron current density and the electron mobility are described in Section 3.1.4.

Calculation of the electron temperature is found through the electron energy equation. Following the time-averaging approach that is performed for the momentum equations, the time-dependent term is discarded from the energy equation. The density and velocity in the flux term is reformulated into the electron current density through Eq. (3.21) while the internal energy is used to represent the electron temperature through

$$e_{\text{int}} = \frac{3}{2}\frac{kT_e}{m_e} \tag{3.24}$$

The electron temperature can be represented as a balance of various heat sources and sinks.[65] The electrons are assumed to be thermalized along the magnetic field lines resulting in constant electron temperatures along those lines. Then only a one dimensional profile of the electron temperature needs to be calculated. In the axial direction,

$$\frac{3}{2}\frac{\partial\left(j_e kT_e/e\right)}{\partial z} = Q_{\text{joule}} - Q_{\text{ion}} - Q_{\text{wall}} - Q_{\text{el}} \tag{3.25}$$

The energy gain is primarily due to Joule heating of the electrons,

$$Q_{\text{joule}} = j_e E_z \tag{3.26}$$

Three energy loss mechanisms are considered. The first is energy loss due to electron impact ionization of neutral atoms,

$$Q_{\text{ion}} = enn_a E_{\text{ion}}\beta \tag{3.27}$$

where E_{ion} is the ground state ionization energy for the propellant in consideration. Energy is also lost due to collisions with the walls,

$$Q_{\text{wall}} = \nu_{\text{wall}} ne\left(2kT_e + (1-s)\phi_s\right) \tag{3.28}$$

which is dependent on the wall collision frequency, ν_{wall}, the secondary electron emission coefficient, s, and the potential drop across the sheath, ϕ_s. These parameters, along with other important plasma properties, are described in more detail in Sections 3.1.4 and 3.2.1 which deal with plasma and sheath properties respectively. The final electron energy loss mechanism included is elastic relaxation with the neutral atoms,

$$Q_{\text{el}} = 3\frac{m_e}{m_i} n\nu_{ea} k(T_e - T_a) \tag{3.29}$$

where ν_{ea} is the collision frequency of the electrons with neutral atoms.

3.1.4 Plasma Properties

In order to solve the governing conservation equations for each of the species, a number of plasma properties need to be calculated. These supplemental equations close the system structured on the conservation equations highlighted in the previous section. This section primarily focuses on the ionization rate, the electron current density, and the electron mobility.

3.1.4.1 Ionization Rate

Appearing in the source terms for the ion and neutral atom continuity equations as well as the ion momentum equation is the volumetric electron impact ionization rate represented by β. The ionization rate is modeled in this work as[6]

$$\beta = \sigma_{\text{ion}} v_{\text{th}} \left(1 + 2\frac{kT_e}{eE_{\text{ion}}}\right) \exp\left(-\frac{eE_{\text{ion}}}{kT_e}\right) \tag{3.30}$$

The calculation of the ionization rate involves the ionization collision cross-section, σ_{ion}, the electron thermal speed, v_{th}, and the ionization energy, E_{ion}. Both the ionization collision cross-section and the ionization energy are properties of the propellant species. Here, for simplicity, a constant is used to approximate a representative cross-section, though the ionization collision cross-section is typically dependent on the electron energy.[99] The ionization energy used is the first ionization energy, the minimum energy required to remove an electron from the ground state of the neutral atom.

3.1.4.2 Current Density

For the calculation of the electric field in Eq. (3.23), the electron current density needs to be known. For Hall thrusters, one of the adjustable parameters is the total discharge current of the device. The total discharge current is composed of the ion and electron current contributions,

$$I_D = I_i + I_e \tag{3.31}$$

where the ion current can be found from integrating the ion current density over the cross-sectional area of the acceleration channel, A.

$$I_i = \int_A env_z dA \tag{3.32}$$

The electron current density is assumed to vary only in the axial direction and is found from dividing the electron current by the cross-sectional area.

$$j_e = \frac{1}{A}\left(I_D - \int_A env_z dA\right) \tag{3.33}$$

3.1.4.3 Electron Mobility

Also required for the electric field calculation is the electron mobility. As given in Eq. (3.22), the electron mobility is dependent on the electron collision frequency. Classical mobility depends on the electrons colliding with ions or the neutral atoms. Electron-ion interactions are dominated by small angle Coulomb collisions. These interactions between charged particles occur with a frequency of[86]

$$\nu_{ei} = \frac{ne^4 \ln \Lambda}{2\pi\epsilon_0^2 m_e^2 v_e^3} = \frac{ne^4 \ln \Lambda}{2\pi\epsilon_0^2 m_e^2 (3kT_e/m_e)^{3/2}} \tag{3.34}$$

where the Coulomb logarithm,

$$\ln \Lambda = \ln\left(n\lambda_D^3\right) \tag{3.35}$$

is dependent on the electron Debye length,

$$\lambda_D = \sqrt{\frac{\epsilon_0 kT_e}{ne^2}} \tag{3.36}$$

The electron-neutral atom collision frequency is modeled by

$$\nu_{ea} = \sigma_{ea} n_a v_{\text{th}} \tag{3.37}$$

where σ_{ea} is the electron-neutral atom collision cross-section. Similar to other collision cross-sections, it is dependent on the electron energy, but here is represented as a constant for the range of energies typical within a Hall thruster.

However, as has been noted by many other researchers developing plasma models to describe the flow in a Hall thruster, the mobility calculated in this manner is often found to be far lower than necessary.[17] Classical mobility is not sufficient in itself to explain the transport of electrons across the magnetic field lines. Thus other contributions to the electron mobility are offered. One is Bohm, or anomalous, diffusion. It is simply modeled as

$$\nu_B = \alpha_B \omega_e \tag{3.38}$$

where ω_e is the electron gyrofrequency. The Bohm coefficient, α_B, has a classical value of 1/16, though it can be empirically adjusted. The physical underpinning of Bohm diffusion is often explained as being due to plasma turbulence. Another contribution to the electron mobility may be due to electrons colliding with the walls of the channel. The electron-wall collision frequency is modeled as[59]

$$\nu_{\text{wall}} = \alpha_{\text{wall}} \frac{v_{\text{th}}}{h} \exp\left(-\frac{e\phi_s}{kT_e}\right) \tag{3.39}$$

This expression is based on the thermal velocity of the electrons divided by the channel width, h, times a factor that incorporates the fraction of electrons with temperature T_e able to penetrate through the sheath potential. The exact nature of the electron-wall interactions within SPT Hall thrusters is not well understood and explanations ranging from a dominant electron repelling sheath, allowing for a very slow electron-wall collision rate, to secondary electrons cascading down the walls, leading to a very high electron-wall collision rate, have been proposed. A coefficient, α_{wall}, is introduced for the wall-collision frequency to adjust this parameter.

The total electron collision frequency used in the calculation of the electron mobility is then a sum of the collision frequencies of electrons with ions, electrons, and the walls along with the Bohm diffusion term. There is also a correctional term that is applied to the electron mobility that adjusts for mobility across magnetic field lines. The final result for the cross field mobility is then

$$\mu_{e_\perp} = \frac{\mu_e}{1 + (\omega_e/\nu_e)^2} = \frac{e/(m_e \nu_e)}{1 + (\omega_e/\nu_e)^2} \tag{3.40}$$

where

$$\nu_e = \nu_{ei} + \nu_{ea} + \nu_{\text{wall}} + \nu_B \tag{3.41}$$

3.1.5 Magnetic Field Considerations

The magnetic field profile plays an important role in affecting the plasma dynamics within a Hall thruster. As mentioned before, the magnetic field strength of these devices is set such that the electrons are magnetized and constrained mainly to the field lines while the ions are largely unmagnetized. Since models of Hall thruster plasmas are often run on the ion time scale, the electrons are assumed to be mobile enough to equilibrate with one another along the magnetic field lines. This allows for simpler calculation of electron properties within the channel.

3.1.5.1 One-Dimensional Approximation

A significant simplification can be made to the model if a one-dimensional approximation is made of the magnetic field configuration. The magnetic field profile is assumed to vary only in the axial direction such that the magnetic field lines lie along the radial direction. This effectively sets all dynamics in the radial direction to be along the magnetic field lines and sets all the cross-field dynamics to be in the axial direction. This is of the most benefit in solving for the momentum equations for the ions as well as the electrons.

The electric field calculation from the electron momentum equation in Eq. (3.18) is kept for the axial component, as it is still across magnetic field lines, but a simpler version can be used to represent the radial component of the electric field. Since the electrons are assumed to thermalize along magnetic field lines, the electron temperature can be considered to be constant along those lines. Also, there is no net electron current that runs along those field lines, and thus the radial component of the electron current density can be ignored. Then the electric field in the radial direction is reduced to

$$enE_r = -\frac{\partial\left(nkT_e\right)}{\partial r} = -\frac{kT_e}{m_i}\frac{\partial \rho}{\partial r} \tag{3.42}$$

Under this form, the radial electric field can be moved from the source terms on the right hand side into the conservative left hand side of the equation. This is performed through establishing a new effective sound speed of

$$a^* = \sqrt{a^2 + \frac{kT_e}{m_i}} \tag{3.43}$$

Basically, the electron and ion pressure terms are combined together to make this new parameter that is constant along magnetic field lines. A similar manipulation can be performed for the axial electric field and ion momentum equations, though now it is across magnetic field lines. The resulting ion momentum equations can be rewritten as

$$\frac{\partial\left(\rho v_z\right)}{\partial t} + \frac{\partial\left(\rho\left(v_z^2 + a^{*2}\right)\right)}{\partial z} + \frac{\partial\left(\rho v_z v_r\right)}{\partial r} = \frac{j_{e_z}}{\mu_e} + \beta n_a v_a \rho \tag{3.44}$$

$$\frac{\partial\left(\rho v_r\right)}{\partial t} + \frac{\partial\left(\rho v_z v_r\right)}{\partial z} + \frac{\partial\left(\rho\left(v_r^2 + a^{*2}\right)\right)}{\partial r} = \frac{\rho a^2}{r} \tag{3.45}$$

This formulation of the ion momentum equations lends itself towards greater stability of the solution scheme, particularly in the radial direction. The radial electric field source term is reduced to a balance of the electron pressure, which is folded into one of the conservative flux terms on the left hand side. The only remaining source term in the radial direction is the axisymmetric adjustment term. In the axial direction, the ionization drag term remains on the right hand side as well as the component of the electric field dependent on the cross-field electron mobility.

3.1.5.2 Two-Dimensional Axisymmetric Case

Though the one-dimensional approximation of the magnetic field offers benefits such as simplifying and improving the stability of the method, the effects of the full magnetic field profile can not always be ignored. The magnetic field profile influences the structure of the plasma and can therefore impact the consequent wall erosion. This is most noticeable in affecting the location where erosion begins, and it can also affect the wall erosion profiles. Depending on the particular configuration of the Hall thruster and its magnetic field, proper modeling of the full two-dimensional profile of the magnetic field and its effect on the thruster plasma can be important to accurately capturing the thruster erosion.

The concept of the thermalized potential proposed by Morozov is used to incorporate the effects of the two-dimensional profile of the magnetic field into the model.[84] Under the assumption of the electrons reaching a thermal equilibrium along the magnetic field lines, the electron momentum equation can be considered as a balance between the electric field and the electron pressure as in Eq. (3.42) for the radial component, for example. The electric field can be integrated in space to find the potential,

$$\phi = \phi^* + \frac{kT_e}{e} \log\left(\frac{n}{n^*}\right) \tag{3.46}$$

where ϕ^*, the thermalized potential, and n^* are reference values. The reference values are found on the channel centerline. They can be calculated in the same manner as the axial terms in the one-dimensional magnetic field profile case. Since the thermalized potential is constant along a magnetic field line, the potential field within the channel can be found from the centerline potential profile. For each point in the channel, the magnetic field lines are traced from the point of interest to the centerline. The field lines are constructed using the streamfunction of the magnetic field. Since the divergence of a magnetic field is zero, following one of Maxwell's laws of electromagnetism, a two dimensional streamfunction of the magnetic field can be constructed such that

$$B_z = \frac{1}{r}\frac{\partial \psi}{\partial r} \tag{3.47}$$

$$B_r = -\frac{1}{r}\frac{\partial \psi}{\partial z} \tag{3.48}$$

A linear interpolation is applied to find better estimates of the location where the streamfunction value lies on the centerline. From the potential field, the resulting electric field profile within the channel can be found from the spatial derivatives.

3.2 Boundary Conditions

The hydrodynamic model simulates the plasma discharge within a Hall thruster acceleration channel from the anode to the exit plane. The domain is an axisymmetric slice of the channel that is bounded by the inner and outer walls. As the walls erode away, the domain is altered to accommodate the new thruster geometry. The domain is covered using a regular structured Cartesian mesh. Ghost cells are employed to set the boundary conditions around the domain. At the anode, the neutral and electron temperatures are set. Assumed conditions for the plasma density and ion velocity are also set at the anode boundary. The settings of the inflow neutral atom velocity and number density are based on the neutral atom thermal velocity and the propellant mass flow rate. At the exit plane, zero gradient Neumann outflow conditions are used for the ion, neutral, and electron properties. The lateral boundary conditions along the walls are described in more detail in the following sections.

3.2.1 Plasma-Sheath Interface

The boundary conditions at the inner and outer walls are not set at the actual wall surfaces, but rather at the plasma-sheath interface. The sheath is a plasma phenomenon that occurs for plasmas that are bounded by wall surfaces. Near the walls, the electrons, due to their higher mobility compared to ions, are more quickly depleted as they are absorbed by the walls. Then a potential difference arises that repels electrons away from the walls while attracting ions to the walls. The sheath potential reaches a value such that the net current, from both ions and electrons, to the walls is zero. The resulting potential across the sheath is[50]

$$\phi_s = \frac{kT_e}{e} \ln \left(\frac{1-s}{v_s \sqrt{2\pi m_e/(kT_e)}} \right) \tag{3.49}$$

where v_s is the ion entrance velocity into the sheath and s is the secondary electron emission coefficient. Secondary electron emission accounts for the electrons emitted from the surface due to electron and ion impacts. The influx of a secondary electron species into the sheath affects the plasma-wall interaction. The secondary electron emission coefficient is modeled empirically here after experimental measurements taken of boron nitride.[33]

$$s = 0.54 + \frac{1-0.54}{40} \frac{kT_e}{e} \tag{3.50}$$

If the secondary electron emission reaches a certain limit, the sheath region can become charge saturated and the physics are affected noticeably. The critical secondary electron emission coefficient value occurs at[50]

$$s_{\text{crit}} = 1 - 8.3\sqrt{\frac{m_e}{m_i}} \tag{3.51}$$

When charge saturation is reached, the sheath potential is estimated to be about the electron temperature in that location.

Since several of the assumptions, such as quasi-neutrality, made in the derivation of the governing equations in the previous section no longer hold in the sheath, the boundaries of the hydrodynamic method are set at the plasma-sheath interface. The traditional solution at the sheath edge requires the ion entrance velocity to be equal to the Bohm velocity,

$$v_B = \sqrt{\frac{kT_e}{m_i}} \tag{3.52}$$

This conclusion is reached since the sheath requires an ion velocity greater than or equal to the Bohm velocity for a monotonic potential distribution across the sheath while the bulk quasi-neutral plasma requires ion velocities below the Bohm velocity.[69] Thus, the Bohm velocity appears to be the natural solution at the plasma-sheath interface. However, this choice of the boundary leads to some unresolved issues, namely, the electric field approaches zero from the sheath side while the electric field approaches negative infinity from the plasma side. A more accurate representation may be to include a smooth transition region between the 'edge' of the bulk plasma and the 'edge' of the sheath.[40,46] For the purposes of this model, the work of Keidar *et al.* and Godyak are followed.[45,59] The Bohm velocity is not assumed *a priori* at the plasma edge. If a nonzero electric field is present, a subsonic entrance velocity can still lead toward a monotonic sheath solution. A relation between the ion velocity and the electric field at the plasma edge is presented in Fig. 3.1. The number density at the sheath edge is calculated from the electric field. Again, if the electron momentum equation is reduced to a balance of the pressure and electric field terms, then a relation for the density can be obtained,

$$n_s = -\frac{kT_e \nabla n}{eE} \tag{3.53}$$

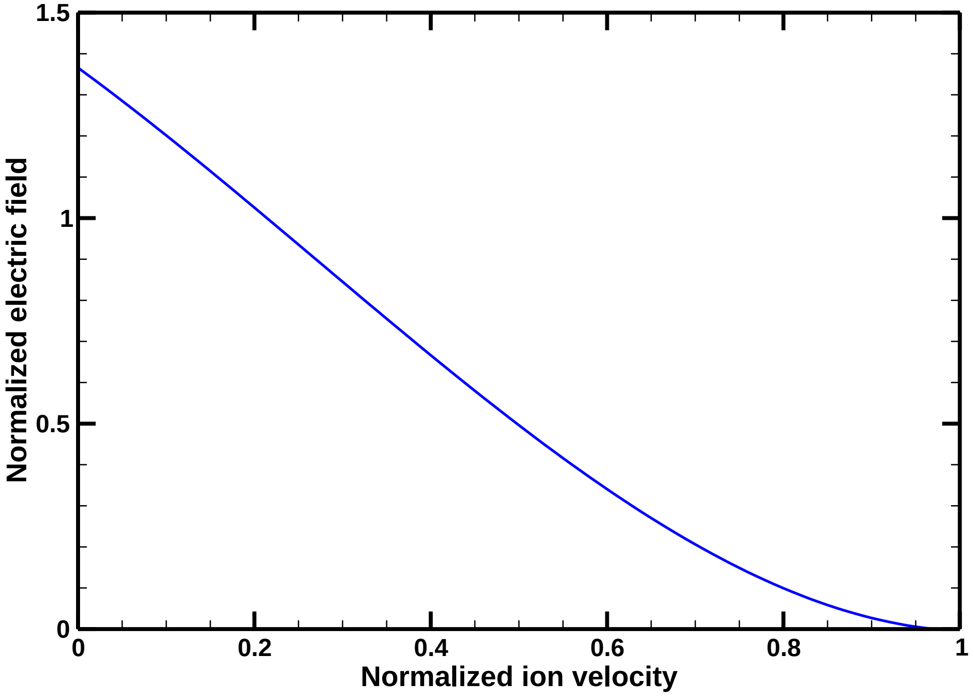

Figure 3.1: The calculated relation between the electric field, normalized by the electron temperature over the Debye length, and the ion velocity, normalized by the Bohm velocity, at the plasma edge.

3.2.2 Cut Cell Eroded Wall Boundaries

The hydrodynamic method is run on a regular axisymmetric Cartesian mesh. To account for the eroded wall profiles that do not lie along the grid points, a cut cell approach is taken.[32,115] The actual calculated wall locations are retained and used to set the location of the boundaries of the domain. When portions of the wall are at an angle to the grid, linear cuts are taken of the rectangular cells to approximate the wall contours. If the cut of the cell leaves less than half of the original cell area in the flow region, then the cut is merged with the adjacent cell that is towards the centerline. Figure 3.2 displays a few examples of cut and merged cells.

Along an angled wall surface, both vertical and horizontal fluxes are calculated from

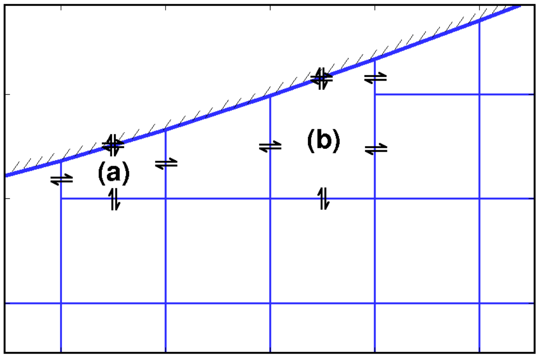

Figure 3.2: Examples of (a) cut and (b) merged cells and associated fluxes.

the sheath ghost cell boundary conditions. Merged cells can also have two fluxes where they are adjacent to two other cells on a side. Both of these situations lead towards multiple fluxes on a side of a cell. The fluxes are weighted according to their relative lengths and these calculations incorporate the volumetric differences due to the axisymmetric nature of the simulated domain.

3.3 Solution Scheme

The hydrodynamic model is solved using a flux-splitting finite volume scheme. Each cell of the simulation domain is treated as a control volume where the integral conservation equations, Eqs. (3.1) to (3.3) are solved. Apart from the contributions of the source terms, the fluxes between each of the cells also affect the conserved values. At each cell interface, the fluxes are calculated following the isothermal version of the Roe solver.[68, 93] The integral form of the axisymmetric conservation equations can be discretized as

$$\frac{U_{i,j}^{t+1}-U_{i,j}^{t}}{\Delta t} = \frac{r_{i-\frac{1}{2},j} l_{i-\frac{1}{2},j} F_{i-\frac{1}{2},j} - r_{i+\frac{1}{2},j} l_{i+\frac{1}{2},j} F_{i+\frac{1}{2},j} + r_{i,j-\frac{1}{2}} l_{i,j-\frac{1}{2}} G_{i,j-\frac{1}{2}} - r_{i,j+\frac{1}{2}} l_{i,j+\frac{1}{2}} G_{i,j+\frac{1}{2}}}{r_c A} + S \tag{3.54}$$

where l is the length of the side, r is the radius of the center of the side segment from the symmetry axis, r_c is the radius of the centroid of the cell, and A is the cell area. Figure 3.3 diagrams a sample cell located at i, j and its associated fluxes. For the ion

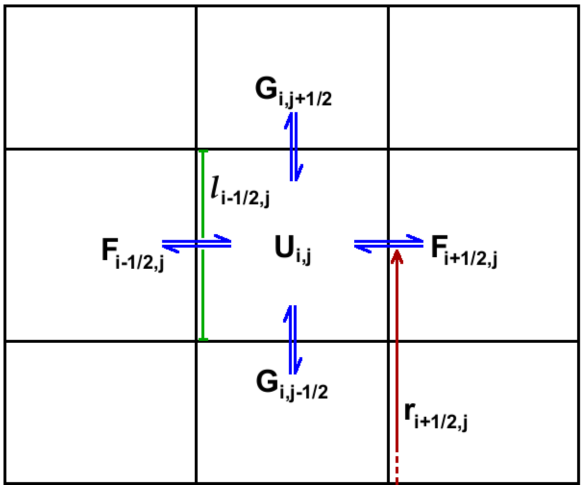

Figure 3.3: A sample cell with associated notation.

conservation equations given in Eqs. (3.9), (3.14), and (3.15), the conserved variables and fluxes are

$$U = \begin{bmatrix} \rho \\ \rho v_z \\ \rho v_r \end{bmatrix}, F = \begin{bmatrix} \rho v_z \\ \rho v_z^2 + \rho a^2 \\ \rho v_z v_r \end{bmatrix}, G = \begin{bmatrix} \rho v_r \\ \rho v_z v_r \\ \rho v_r^2 + \rho a^2 \end{bmatrix} \tag{3.55}$$

The Roe scheme is an approximate Riemann solver that solves for the fluxes—here, the radial flux is shown as an example—through

$$G_{j+\frac{1}{2}} = \frac{1}{2}\left(G_j + G_{j+1}\right) - \frac{1}{2}\sum |\lambda| \alpha R \tag{3.56}$$

where λ are the wave speeds and αR are the wave strengths. To calculate these values, this solver uses the Roe average, which between cells $j-1$ and j, for example, is

$$\bar{v} = \frac{v_{j-1}\sqrt{\rho_{j-1}} + v_j\sqrt{\rho_j}}{\sqrt{\rho_{j-1}} + \sqrt{\rho_j}} \tag{3.57}$$

Then the resulting Jacobian matrix of the system is

$$\frac{\partial G}{\partial U} = \begin{bmatrix} 0 & 0 & 1 \\ -\bar{v}_z\bar{v}_r & \bar{v}_r & \bar{v}_z \\ a^2 - \bar{v}_r^2 & 0 & 2\bar{v}_r \end{bmatrix} \tag{3.58}$$

The eigenvalues of the Jacobian provide the three wave speeds,

$$\lambda = \bar{v}_r - a, \bar{v}_r, \bar{v}_r + a \tag{3.59}$$

The eigenvectors of the Jacobian are

$$R = \begin{bmatrix} 1 \\ \bar{v}_z \\ \bar{v}_r - a \end{bmatrix}, \begin{bmatrix} 0 \\ 1 \\ 0 \end{bmatrix}, \begin{bmatrix} 1 \\ \bar{v}_z \\ \bar{v}_r + a \end{bmatrix} \tag{3.60}$$

To find the wave strengths, the inverse of the matrix containing the eigenvectors is multiplied by the change in the conserved variables,

$$\begin{aligned} \alpha = {} & R^{-1}\Delta U \\ = {} & \frac{1}{2a}\begin{bmatrix} \bar{v}_r + a & 0 & -1 \\ -2a\bar{v}_z & 2a & 0 \\ -\bar{v}_r + a & 0 & 1 \end{bmatrix}\begin{bmatrix} \Delta\rho \\ \Delta(\rho v_z) \\ \Delta(\rho v_r) \end{bmatrix} = \frac{1}{2a}\begin{bmatrix} (a + \bar{v}_r)\Delta\rho - \Delta(\rho v_r) \\ -2a\bar{v}_z\Delta\rho + 2a\Delta(\rho v_z) \\ (a - \bar{v}_r)\Delta\rho + \Delta(\rho v_r) \end{bmatrix} \end{aligned} \tag{3.61}$$

Similar operations are performed to produce the axial fluxes, F. In the one dimensional magnetic field approximation described in Section 3.1.5.1, the only change required is to replace the sound speed, a, with the modified sound speed, a^*, described in Eq. (3.43). For the neutral atoms, the same process is taken, but only performed in a one dimensional setting with just the continuity and axial momentum equations.

The simulation is initialized with a uniform flow based on the inflow conditions throughout the domain. The various plasma properties, based on the electron parameters, needed to calculate boundary conditions and source terms are found. The flux calculations are then carried out throughout the domain, including those at the boundaries involving ghost cells. The cell-centered conserved values are then found from solving the ion and neutral atom conservation equations through the process above. This process is iterated until a representative steady state is reached. The time scale for channel wall erosion is much greater than that of plasma oscillations, and therefore a representative steady state calculation of the plasma flow is sufficient for the needs here.

For Hall thrusters, only a small number of variables are set or observed directly by the experimentalist, operator, or designer. These include the discharge voltage and current, propellant mass flow rate, magnetic field profile, and the thruster geometry. Hall thrusters are voltage regulated devices, so the voltage difference between the anode and cathode are fixed. The discharge current is not fixed, but can be adjusted depending on the mass flow rate and magnetic field configuration. For the hydrodynamic simulations, the magnetic field profile and the thruster geometry are directly applied to the model. The propellant mass flow rate is used to set the inflow neutral atom number density and the discharge current is used to calculate the electron current density within the thruster. The discharge voltage is left as a free parameter to be matched to experimental results. Other parameters that are available for comparison include thrust and measurements of the plasma properties such as the electron temperature or electric field. The unknowns in the simulation inputs are altered to try to match the available measured data. The simulation parameters for this hydrodynamic method that can be varied include the ion boundary conditions at the anode, the electron temperature at the anode, and the electron mobility terms. As with any other simulation model, care must be taken in adjusting these parameters within reasonable values. Ideally, only minor adjustments would need to be made between modeling different thrusters and operating conditions.

CHAPTER IV

Molecular Dynamics Sputter Model

4.1 Governing Equations

Molecular dynamics is a deterministic computational simulation method that models the dynamics of a system of particles. At its very basic roots, this method calculates the positions of each particle by integrating their acceleration through time. The acceleration vectors are found from Newton's law of motion, involving the forces acting upon each particle. The forces are modeled by potential functions describing the interatomic interactions among the atoms. These potentials are functions of particle positions only. Then, at each iteration of the simulation process, the particle positions are updated, the potentials are re-calculated based on the new positions, and the resulting force, and therefore acceleration, is integrated in time to find the new particle positions. Each step of the process is described in more detail in the following sections.

4.1.1 Newton's Law of Motion

Molecular dynamics models a system of particles governed by the classical dynamics of Newton's law of motion,

$$\vec{F} = m\vec{a} = m\frac{\partial^2 \vec{r}}{\partial t^2} \tag{4.1}$$

where each particle with a mass m is accelerated by $\vec{a}$ due to a force $\vec{F}$. The acceleration is also the second derivative of the particle position with respect to time. The forces on each particle are assumed to arise from a conservative force field described by the appropriate potential functions.

4.1.2 Interatomic Potential Functions

A main key to molecular dynamics simulations lies in the potential functions used to describe the system. They often comprise the bulk of the complexity and computational requirements of the simulation and are largely responsible for the fidelity of the model to the actual physics. As stated above, the role of the potential functions is to determine the forces acting upon each particle. Since the force field is conservative, the forces can be calculated from the negative gradient of the potential function

$$\vec{F} = -\nabla\Phi \tag{4.2}$$

To calculate the components of the forces along the directions between each pair of atoms, derivatives of bond lengths and angles with respect to a particular direction need to be found. The full derivation of the force components for the potentials used in this work is provided in the Appendix. The system under consideration for this work is a boron nitride (BN) surface under xenon ion bombardment. Therefore, a potential function that describes the interaction of the boron and nitrogen atoms with one another is needed as well as one to simulate the impacting xenon ions.

4.1.2.1 Boron Nitride Potential Function

The interaction of the boron and nitrogen atoms with other boron and nitrogen atoms is governed by a potential function presented by Albe *et al.*[7,8] This potential is based on the Tersoff potential, a bond order potential, which was originally developed for silicon systems and is well suited for other covalent systems such as BN.[103,104] Bond order potential functions incorporate environmental influences—including the coordination number, bond lengths, and bond angles—for determining the strength of each bond. Thus, if properly tuned, these bond order potentials have good capability to simulate not only ordered lattice structures, but also different structural configurations, such as those that would be present in surface sputtering scenarios. The Albe potential is fitted to a number of two and three-body boron and nitrogen configurations whose structural properties are known, while also maintaining good comparisons to various phases of bulk BN.[8]

The base form of the potential is given by

$$\Phi = \frac{1}{2} \sum_{i \neq j} f_c\left(r_{ij}\right)\left[f_R\left(r_{ij}\right) - b_{ij} f_A\left(r_{ij}\right)\right] \tag{4.3}$$

where f_c is a cutoff function limiting the range of the potential. The f_R and f_A terms are the repulsive and attractive parts of the potential, respectively. The b_{ij} term is a modifier to the attractive force component that takes into account third-body bond stretching and bending, and r_{ij} is the distance from particle i to particle j. The potential is dependent on particle positions only.

The repulsive and attractive components to this potential are similar in form and are based on a Morse potential,[23]

$$f_R\left(r_{ij}\right) = \frac{D_0}{S-1} \exp\left(-\beta\sqrt{2S}(r_{ij} - r_0)\right) \tag{4.4}$$

$$f_A\left(r_{ij}\right) = \frac{SD_0}{S-1} \exp\left(-\beta\sqrt{\frac{2}{S}}(r_{ij} - r_0)\right) \tag{4.5}$$

where D_0 is the dimer energy and r_0 is the dimer separation. S and β are fitting constants. The resulting potential curves from these components are shown in Fig. 4.1. As per a typical pair potential well profile, an attractive force, here due to covalent bonding, draws the two atoms together while the Pauli exclusion principle presents a strong repulsive core when the atoms approach too close to each other. Outside of a certain range, set by the cutoff function, no interaction between the atoms is considered.

The flexibility of bond-order potentials stems from the modifier term b_{ij}, which for this potential is given as

$$b_{ij} = \left(1 + \gamma^n \chi^n\right)^{-1/2n} \tag{4.6}$$

$$\chi = \sum_{k \neq i,j} f_c(r_{ik}) g(\theta_{ijk}) h(r_{ij}, r_{ik}) \tag{4.7}$$

$$g(\theta_{ijk}) = 1 + \frac{c^2}{d^2} - \frac{c^2}{d^2 + \left(m - \cos(\theta_{ijk})\right)^2} \tag{4.8}$$

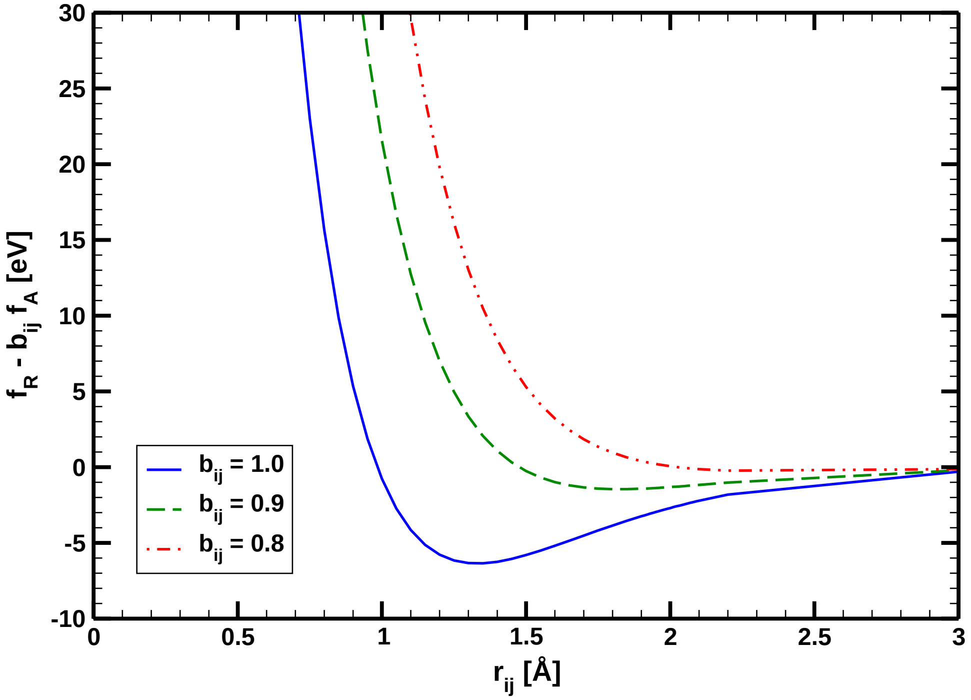

Figure 4.1: Sample potential well profiles.

$$h(r_{ij}, r_{ik}) = \exp\left(\lambda^3 (r_{ij} - r_{ik})^3\right) \tag{4.9}$$

where the index k indicates the third particle under consideration (θ_{ijk} would be the angle between ij and ik) and γ, n, c, d, m, and λ are all constants. The effect of the b_{ij} term on the potential profile is also shown in Fig. 4.1.

The cutoff function, f_c, is changed from the sine-based function used by Albe *et al.*[8]

$$f_c\left(r_{ij}\right) = \begin{cases} 1, & r_{ij} \leq R - D \\ \frac{1}{2} - \frac{1}{2}\sin\left(\pi \frac{r_{ij} - R}{2D}\right), & R - D < r_{ij} < R + D \\ 0, & r_{ij} \geq R + D \end{cases} \tag{4.10}$$

to a different one based on an exponential function[74]

$$f_c\left(r_{ij}\right) = \begin{cases} 1, & r_{ij} \leq R - D \\ \exp\left(\alpha \frac{x^3}{x^3 - 1}\right), & R - D < r_{ij} < R + D \\ 0, & r_{ij} \geq R + D \end{cases} \tag{4.11}$$

$$x = \frac{r_{ij} - (R - D)}{2D} \tag{4.12}$$

where D and R set the radii of the cutoff shell. The cutoff function given by Eqs. (4.11) and (4.12) is equal to zero at both ends up to the second derivative and provides for a smoother transition than the function given in Eq. (4.10). This is seen in Fig. 4.2 where the first derivatives, important for the force calculations, of both cutoff functions are plotted. For the exponential-based cutoff function, the magnitude of the local extremum of the first derivative is minimized when the coefficient α is set to 3.

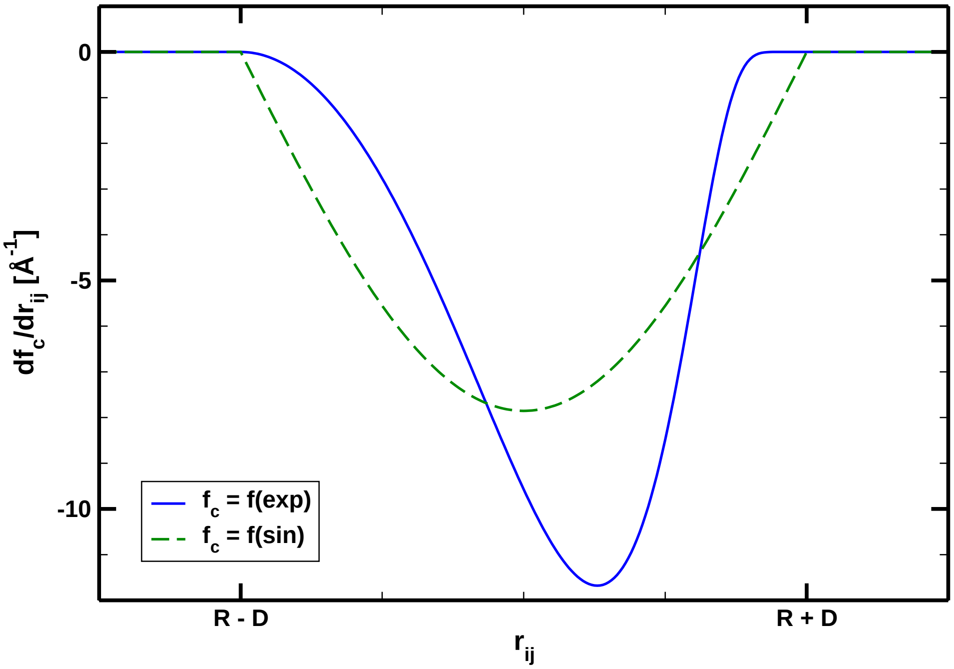

Figure 4.2: The first derivative of the sine-based (Eq. (4.10)) and exponential-based (Eq. (4.11)) cutoff functions.

A second modification is made to this potential. The original form of the potential has a very high sensitivity to bond angles for bonds involving boron-boron interactions due to the small value of d used in the final term of Eq. (4.8). Around the critical angle set by m, this portion of the potential function has very large gradients as shown in Fig. 4.3. To traverse these steep slopes properly would require a prohibitively small timestep. Thus, to keep simulations within a reasonable amount of computational time, the sensitivity here is reduced by changing the values of c and d from 0.52629 and 0.001587 to 3.316257 and 0.01 respectively. This maintains the same ratio of c^2 to d^2 in the second term in Eq. (4.8) while reducing the sensitivity of the final term. The values

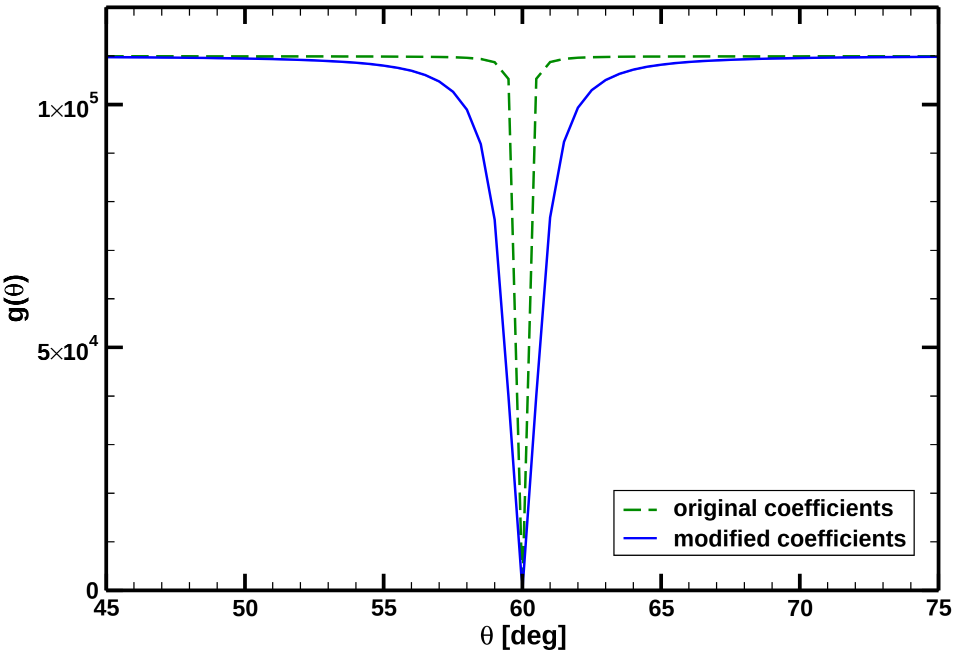

Figure 4.3: Plot showing the sensitivity of the function in Eq. (4.8) for B-B bonds.

of all the coefficients used for this BN potential are given in Table 4.1.

Unfortunately, the bulk form of boron nitride in any phase does not include any boron-boron bonds, therefore it is difficult to ascertain the extent of the effects of the modification to the potential. Typical parameters that would be tested, such as the bulk modulus and other elastic properties of BN, are unaffected by the change. Running a series of cases with the unmodified potential to calculate the sputter yields to compare results with the modified potential would require a considerable amount of computational time and resources, so that is not a viable option either. The modifications made here to c and d in Eq. (4.8) are made in the interest of allowing for a reasonable timestep for resolution of the potentials while maintaining energy conservation, but this is an area that might warrant further investigation.

4.1.2.2 Xenon Potential Function

According to sputtering theory, the xenon ion is assumed to be neutralized before impact by an electron from the surface; electrostatic effects do not need to be considered.[108] The impacting ion is treated as a neutral atom in the sputtering simulations, but to

	B-B	N-N	B-N
R [Å]	2.0	2.0	2.0
D [Å]	0.1	0.1	0.1
D_0 [eV]	3.08	9.91	6.36
r_0 [Å]	1.59	1.11	1.33
β [Å^{-1}]	1.5244506	1.92787	2.043057
S	1.0769	1.0769	1.0769
n	3.9929061	0.6184432	0.364153367
γ	0.0000016	0.019251	0.000011134
c	3.316257	17.7959	1092.9287
d	0.01	5.9484	12.38
m	0.5	0.0	-0.5413
λ [Å^{-1}]	0.0	0.0	1.9925

Table 4.1: Coefficient values used for the boron nitride potential function.[8]

distinguish it from the surface atoms, it will continue to be designated as the "ion". A purely repulsive potential, such as a Molière potential or a "universal" Zeigler, Biersack, and Littmark (ZBL) potential function, is often used to describe the ion interactions. Since the van der Waals attraction of the xenon with the boron and nitrogen atoms is much weaker than the covalent attraction the boron nitride has within itself, a purely repulsive force is acceptable.[57] The Molière potential function is used to model the xenon ions in this work. It is based on a screened Coulomb repulsion and has the form

$$\Phi = \frac{Z_i Z_j e^2}{4\pi\epsilon_0 r_{ij}} \left[0.35\exp\left(-0.3\frac{r_{ij}}{a_F}\right) + 0.55\exp\left(-1.2\frac{r_{ij}}{a_F}\right) + 0.10\exp\left(-6.0\frac{r_{ij}}{a_F}\right)\right] \tag{4.13}$$

where Z_i and Z_j are the atomic numbers of the atoms in question, e is the elementary charge, and ϵ_0 is the permittivity of free space. The potential depends on a_F, the Firsov screening length, which is based on calculations involving the Thomas-Fermi function,[87]

$$a_F = \frac{0.8853a_0}{\left(\sqrt{Z_i} + \sqrt{Z_j}\right)^{2/3}} \tag{4.14}$$

where a_0 is the Bohr radius.

4.1.3 Leapfrog Scheme

Once the forces on each particle have been calculated from the potential functions, the particle velocities and positions can be updated. A finite difference method is typically used to integrate forward through time. These schemes are based on the Taylor series expansions of the positions,

$$\vec{r}\,(t+\Delta t) = \vec{r}(t) + \vec{v}(t)\Delta t + \frac{1}{2}\vec{a}(t)\Delta t^2 + \dots \tag{4.15}$$

A common approach is to use the Verlet method. This scheme results from combining the forward step expansion given in Eq. (4.15) with the backward step expansion,

$$\vec{r}\,(t-\Delta t) = \vec{r}(t) - \vec{v}(t)\Delta t + \frac{1}{2}\vec{a}(t)\Delta t^2 - \dots \tag{4.16}$$

The result is

$$\vec{r}\,(t+\Delta t) = 2\vec{r}(t) - \vec{r}(t-\Delta t) + \vec{a}(t)\Delta t^2 + O(\Delta t^4) \tag{4.17}$$

The Verlet method is a stable third-order method with wide application in molecular dynamics. It does have its drawbacks, however, the main one being that it does not explicitly calculate the particle velocities which are useful in computing energies and temperatures. Thus, an equivalent form of the Verlet method, the leapfrog scheme, is used instead. The leapfrog method staggers the position and velocity calculations by a half timestep

$$\vec{v}\,(t+\Delta t/2) = \vec{v}\,(t-\Delta t/2) + \vec{a}(t)\Delta t \tag{4.18}$$

$$\vec{r}\,(t+\Delta t) = \vec{r}(t) + \vec{v}\,(t+\Delta t/2)\,\Delta t \tag{4.19}$$

The leapfrog scheme is simple, yet robust and accurate enough for sputtering studies. Higher order schemes, such as predictor-corrector methods, are not used in this work due to their increased complexity and their need for more force calculations per timestep. To initialize the simulations, the starting positions of the particles at time $t = 0$ are set to the equilibrium lattice configuration. The initial velocities at time $t = \Delta t/2$ for each particle are chosen randomly from a Gaussian distribution around the equilibrium temperature for each axis direction through

$$v = \sqrt{-\ln q_1} \cos(2\pi q_2) \sqrt{\frac{2kT_0}{m}} \tag{4.20}$$

where q_1 and q_2 are random numbers between zero and unity. A correction is applied to the velocities to ensure the bulk velocity of the entire system is zero in every direction. The system is then stepped forward through time using the leapfrog scheme.

4.2 Domain Configuration

The system of interest for this work ultimately should model the behavior of the surface of a Hall thruster acceleration channel wall under xenon ion bombardment. The acceleration channel wall material for SPT-type Hall thrusters is often boron nitride or a BN compound. For the boron nitride, it is typically the hexagonal boron nitride (h-BN) allotrope that is used. For the molecular dynamics simulations, a small sample of h-BN is modeled and simulated to undergo impacts from xenon ions.

4.2.1 Boron Nitride Lattice

Hexagonal boron nitride is structurally similar to graphite. Alternating boron and nitrogen atoms are placed in hexagonal lattices which are arranged as a series of sheets. Equilibrium dimensions[8] and a sample view are shown in Table 4.2 and Fig. 4.4, respectively.

Three domain sizes are used to model the BN surface. The lateral dimensions need to be large enough to contain the area of effect of an ion impact as it imparts momentum and energy cascades across the surface. As sputtering events typically only involve a few layers of atoms closest to the surface, the height of the BN block is often shorter in length than the other two dimensions. The energy of the impacting ion will dictate the domain size necessary as higher energy ions will require larger domains to contain the full effect of the impact without overlap. The smallest domain, used for ion energies at 100 eV or below, consists of 24 sheets that are 18 hexagons wide and 10 hexagons

Dimension	Length [Å]
a	2.496
c	3.245
s	1.441

Table 4.2: Dimension lengths of h-BN.

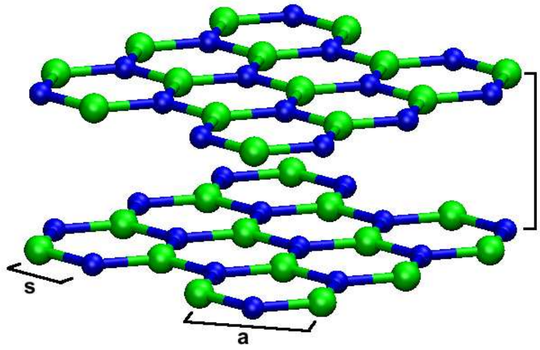

Figure 4.4: Sample view of an h-BN lattice.

high, resulting in a 7.8 nm × 7.8 nm × 2.5 nm BN block. A larger domain, used for ion energies between 100 and 250 eV, is 32 sheets of 24 × 12 hexagons, or a 10.4 nm × 10.4 nm × 3.0 nm block. The largest domain, for ion energies at 250 eV and above, has 40 sheets of 30 × 12 hexagons, or a 13.0 nm × 13.0 nm × 3.0 nm block.

4.2.2 Boundary Conditions

Periodic boundary conditions are applied in the lateral directions. Particle interactions and movement wrap around to the opposite edge. Benefits of periodic boundary conditions include proper particle dynamics at the system boundaries, instead of affecting momentum or energy as fixed or damped boundary conditions would. One thing to consider with periodic boundary conditions for sputtering simulations, however, is that they represent an infinitely repeating domain of closely impacting ions. This leads to a much greater ion flux than measured in sputtering experiments or expected for Hall thruster operation. The simulation domain size should be large enough such that the energy cascading from the ion impact does not cross over and influence the same region. This can be tested for, in part, by examining the sputter yields calculated, since higher energies can be expected to lead towards a higher sputtering rate. Domain size independence, with respect to the calculated sputter yields, is established for the three sizes used in this work at the energies tested.

A fixed boundary condition is applied to the bottom layer of boron and nitrogen atoms that is the furthest away from the surface. The interaction of these atoms with other atoms is not altered in any way, but their position is kept fixed. This is to prevent translation of the domain in any direction. The next two layers of atoms directly above the fixed layer have a thermostat applied to them for temperature regulation of the BN block which is described in further detail in Section 4.3.1. Figure 4.5 displays an end-on view of the h-BN block with the immobile and thermostat layers highlighted. The surface layer of atoms is kept as a free boundary. A region of free space is maintained above the surface where ions and sputtered particles can traverse between the bulk BN block and the boundary with free space.

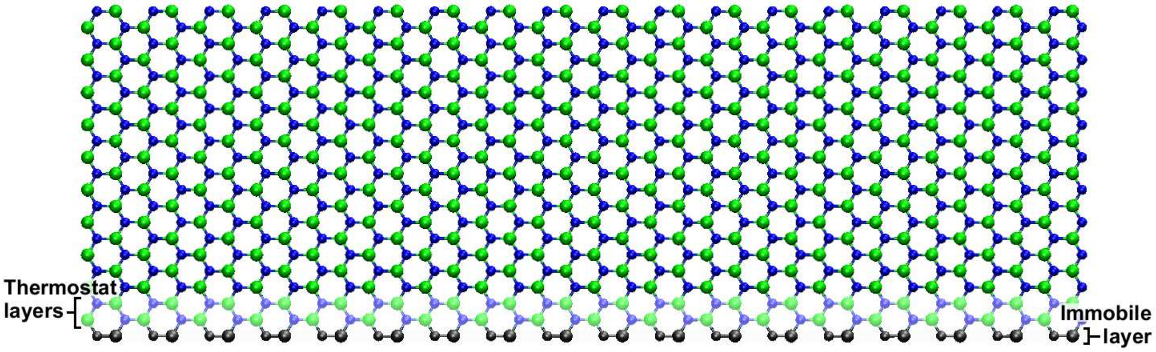

Figure 4.5: An end-on view of h-BN showing the fixed and thermostat layers.

4.3 Simulation Methodology

The basic procedure for running a sputtering simulation begins with relaxing the BN surface from its lattice structure. Due to atomic vibrations, the structure will not stay in a rigid configuration. Thus, the system is allowed to equilibrate to a more natural state before beginning the sputtering studies. Once the BN structure is ready, an ion is inserted into the simulation at a random location far enough above the surface to be outside the interaction range between it and the atoms of the surface. The ion is given an initial trajectory within the constraints set upon it, such as the angles or its energy. For the simulations run for this work, the lateral angle—the angle with respect to any line running along the plane of the surface—is randomized to reduce the effect that lattice orientation might have on the sputtering. The angle incident from the surface normal is fixed and the energy of the ion is set as needed. After the ion impacts the surface, the system is allowed to relax again before another ion is inserted. This allows for the simulation to capture any sputtering that occurs relatively late after the moment the ion impacts the surface. It also helps to account for the lower ion flux to the surface typically observed in experimental sputtering studies or Hall thruster operation. Thermal regulation of the BN surface is also important in regards to this portion of the simulation.

4.3.1 Temperature Regulation and Monitoring

The temperature of the BN system is regulated through an applied thermostat. Here, the Berendsen thermostat is used on the two layers of atoms right above the immobile layer, as shown in Fig. 4.5. The Berendsen thermostat uses a form of velocity rescaling, which when applied to the velocity calculation in the leapfrog scheme given in Eq. (4.18) becomes[14]

$$\vec{v}(t+\Delta t/2) = \lambda \left[\vec{v}(t-\Delta t/2) + \frac{\vec{F}(t)}{m}\Delta t \right] \tag{4.21}$$

$$\lambda = \sqrt{1 + \frac{\Delta t}{\tau}\left(\frac{T_0}{T} - 1\right)} \tag{4.22}$$

where T is the instantaneous temperature of the thermostat layers and T_0 is the desired equilibrium temperature. The Berendsen thermostat allows the temperature to gradually re-equilibrate; how tightly the system is coupled to the temperature correction is controlled through the use of a relaxation time constant, τ. Larger time constants give a looser coupling, while smaller values of τ enforce a tighter coupling. The ratio of Δt to τ is kept near 0.0025, which is within the typical values for this parameter. The Berendsen thermostat is chosen for its simplicity of implementation. The resulting distribution function for the temperatures does not conform to the canonical, but since most of the dynamics for sputtering occur in the first few layers of the surface, a simpler thermostat applied to a region relatively far from the surface is acceptable.

The temperature of the rest of the BN system apart from the thermostat layers is eventually regulated through conduction as the atoms interact with one another. The thermostat layers represent the relative heat sink of the bulk of the material not represented away from the surface. The thermostat is not applied directly to the whole system since the dynamics of the surface atoms should be left unmodified as much as possible for more accurate modeling of sputter phenomena.

Calculation of bulk temperatures is found through the kinetic energy of the particles,

$$KE = \frac{1}{2}m|\vec{v}|^2 = \frac{3}{2}kT \tag{4.23}$$

Then the instantaneous temperature of the system under consideration is

$$T = \frac{2}{3(N-1)k}\sum_{i}^{N}\frac{1}{2}m_i|\vec{v}_i|^2 \tag{4.24}$$

where N is the number of atoms in the system. Since there can be high statistical scatter in the calculated instantaneous temperature, a way to find an averaged temperature is desired. A sub-relaxation technique is employed to more accurately gauge the macroscopic temperature of the system.[100] This method takes a weighted average of the new instantaneous temperature and the previous average temperature, $\bar{T}$.

$$\bar{T} = \left(1 - \frac{1}{\sigma}\right)\bar{T} + \frac{1}{\sigma}T \tag{4.25}$$

where σ sets the weighting preference. Equation (4.25) provides for a good estimate of the time-averaged temperature, however, after many iterations, the past history accumulates too much weight on the temperature averaging process and the calculated average lags behind the true average. Every σ timesteps during the simulation, the average temperature can be reset to some degree through

$$\bar{T} = \bar{T} + \frac{\left(1-\frac{1}{\sigma}\right)^{\sigma-1}}{1-\left(1-\frac{1}{\sigma}\right)^{\sigma-1}}\left(\bar{T} - \bar{T}_{old}\right) \tag{4.26}$$

$\bar{T}_{old}$ is the average temperature calculated σ timesteps prior to this re-adjustment of the average. Figure 4.6 shows a sampling of calculated instantaneous temperatures and the corresponding sub-relaxation calculated average temperature for a sample test case involving a desired equilibrium temperature of 423 K.

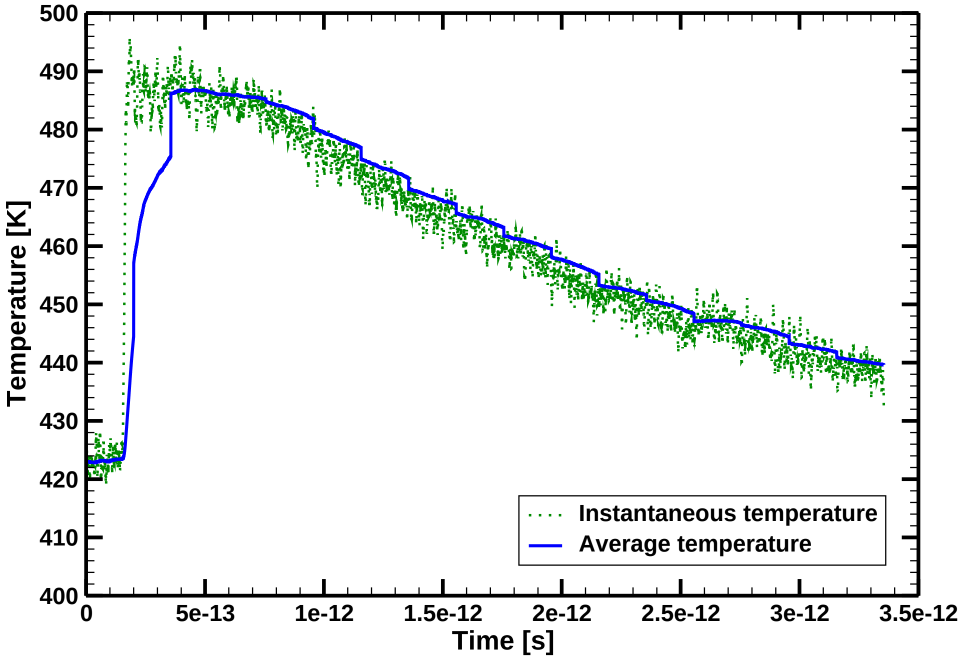

Figure 4.6: Sample output of instantaneous temperatures and sub-relaxation averages.

4.3.2 Speed Up Techniques

The basic unoptimized molecular dynamics algorithm runs on the order of $O(N^3)$ since the force interactions, or at least the distances, of every possible three-body combination in the system needs to be computed. The force calculations are usually the most computationally intensive portions of each iteration, involving expensive calculations such as exponential or trigonometric functions. Also, due to the dynamics of the atomic interactions, the timestep is usually shorter than a femtosecond—for this work, a timestep of 1×10^{-16} seconds is used—whereas sputtering events and proper relaxation of the surface after each ion impact usually requires on the order of picoseconds or tens of picoseconds to resolve. In addition, a sufficient number of ion impact simulations needs to be performed to gather enough data to improve the statistics of the results. Thus, the simulation of sputtering for even a domain only nanometers on a side can require enormous amounts of computation time.

Fortunately, there are a number of techniques to speed up the calculations for molecular dynamics. Two methods take advantage of the short-range nature of the boron nitride potential. Since a cutoff function is applied to the potentials such that interaction beyond a certain range is ignored, the forces and even the distances beyond that radius do not need to be calculated. A Verlet, or neighbor, list can be constructed for each atom that contains all of the surrounding atoms within a radius slightly larger than the cutoff range. Since the atoms do not move a great distance across several timesteps, the Verlet list does not have to be updated every timestep. Then, the force calculations require roughly only $O(N)$ operations since there are a limited number of atoms within each Verlet list. The list generation still requires $O(N^2)$ operations, however. If a cell list is also employed, then the list generation can also be reduced to an $O(N)$ calculation. If the domain is divided into an array of cells, then for the generation of the Verlet lists, only the particles in the same and adjoining cells need to be considered. Using both of these techniques greatly reduces the number of distance and force calculations required to run the simulations.

Another method to reduce the number of computations is to increase the timestep when possible. Though a fairly small timestep is necessary when the fine motion of the atom dynamics needs to be resolved—for sputtering, this includes when the ion impacts the surface and particles are moving relatively fast—larger timesteps can be used during less sensitive phases of the simulation, such as the latter portion of relaxation of the surface back to the equilibrium temperature. For the simulations performed for this work, the criterion of when the energy of every particle falls below a specified level is used to determine when the timestep can be increased.

Finally, the simulation code is parallelized using OpenMP directives. Since most of the calculations that loop over every particle are largely independent of one another, the domain can be decomposed and sent to different processors. OpenMP offers a relatively easy implementation for parallelization on shared memory systems.

4.3.3 Sputter Yield Calculation

Before statistics on sputtering yield can be obtained, the system needs to be primed first. The effects of ion impacts on a surface that is relatively unmodified from the original lattice structure may be different than the sputtering process and results after the surface has already been bombarded by a large number of ions. One visual inspection is that the surface acquires an amorphous region at the very surface of the block. The ion bombardments have broken many of the initial bonds and the boron and nitrogen atoms re-bond into different configurations. This is seen in Fig. 4.7 where the top layers on the surface have undergone a significant change in structure from the relatively unaltered hexagonal layers underneath; this is quite in contrast from the initial configuration shown in Fig. 4.5. Results for sputter yield analyses are gathered after this amorphous layer has been established.

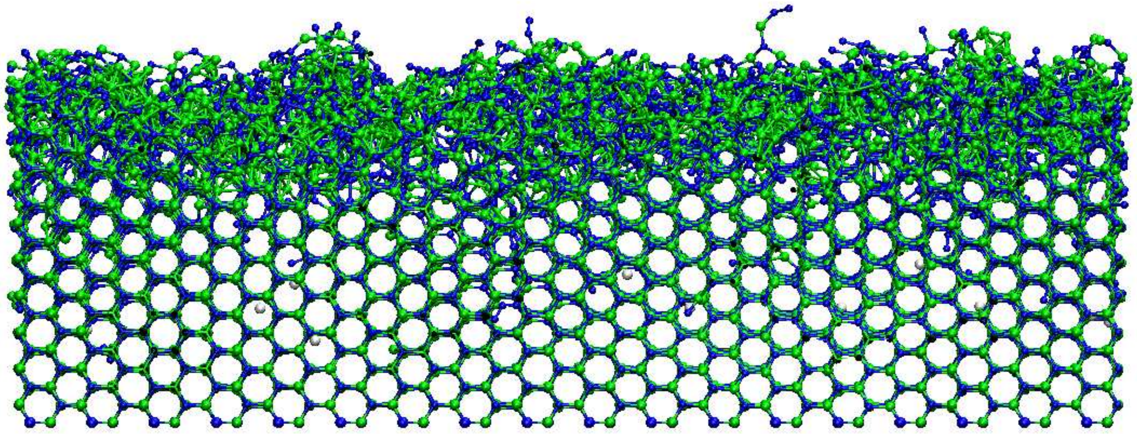

Figure 4.7: An end-on view of h-BN showing the amorphous region on the surface after a number of ion impacts have already occurred.

During each ion impact and subsequent relaxation period, sputtering events are accounted for by tracking any particles that pass the upper boundary set above the surface. For each particle that is counted as a sputtered particle, if it has any neighboring particles, they are considered together as a sputtered molecule. Based on the molecular weights of the particles escaping the domain, the mass-based sputter yield per ion can be calculated. Since the actual number and type of sputtered particles can vary quite a bit for different ion impacts, many ion impact simulations are necessary to generate enough statistics to capture the comprehensive picture of sputtered particles. For each of the sputtered atoms or molecules, the center-of-mass trajectory and energy are recorded as they exit the domain. This allows for differential sputtering analyses to be performed in addition to the total integrated sputter yield.

CHAPTER V

Model Results and Experimental Validation

5.1 Hydrodynamic Plasma Model Results

5.1.1 A Comparison of Xenon and Krypton Propellants for the NASA-173Mv1 Thruster

The hydrodynamic model is used to simulate the plasma discharge within the NASA-173Mv1 Hall thruster for both xenon and krypton propellants. Xenon is currently the predominant species in use as a propellant for Hall thrusters, but there is a growing interest in using krypton as well. Krypton offers several advantages over xenon as a propellant in electric propulsion devices. The most practical reason is the cost, as krypton is more abundant and therefore less expensive than xenon. Krypton also offers a higher specific impulse due to its lower atomic mass than xenon, further lowering mission costs. On the other hand, krypton has been observed to produce lower thruster efficiencies stemming from a higher ionization potential, lower propellant utilization, and increased beam divergence.[78,89] However, a couple of studies have shown that efficiencies comparable to xenon based thrusters can be achieved with krypton.[53,89] To provide a greater understanding of the various effects of krypton as a propellant, the hydrodynamic model is applied to analyze the differences between xenon and krypton and to compare the data with experimental results. This will also provide an opportunity to observe how the hydrodynamic model performs in simulating a Hall thruster plasma flow.

In terms of thruster erosion rates, krypton generally shows a lower sputter yield than xenon for a boron nitride surface,[62] which is primarily due to its lower molecular weight.

The lower sputter yields, however, are offset by possible longer lifetime requirements and higher operating discharge voltages.[70] The longer life requirements, due to krypton's higher specific impulse and lower thrust, necessitate lower erosion rates. Optimization of krypton performance often involves higher discharge voltages, which lead to higher ion energies impacting the channel walls, thus increasing the sputter yields.

5.1.1.1 Background

Experimental work has been performed on the NASA-173Mv1 Hall thruster to characterize some of the differences between using xenon and krypton, particularly in trying to explain the performance issues of krypton.[70–72] Internal plasma measurements were taken and analyzed. Krypton experiences a lower propellant utilization and a larger beam divergence, which appear to be the main contributors to its lower performance characteristics in general. Configuring the magnetic field topography to increase krypton propellant utilization, however, affects the beam divergence as well as other aspects of the plasma flow. A better understanding of the effects of the magnetic field topography as well as other thruster design inputs on the ionization and acceleration of the propellant gas may lead towards improving krypton efficiency in these thrusters.

The experimental data were obtained from tests run on the NASA-173Mv1 Hall thruster in the Large Vacuum Test Facility (LVTF) at the Plasmadynamics and Electric Propulsion Laboratory (PEPL).[70,71] The test chamber is a cylindrical tank 9 m in length and 6 m in diameter. The base pressure is 1.5×10^{-7} torr and 3.3×10^{-6} torr during operation. The High-Speed Axial Reciprocating Probe (HARP) system is used to probe inside of the thruster channel.[48] A floating emissive probe and single Langmuir probe are attached to the HARP system and are swept into the thruster channel at high speeds such that the probes are kept in the channel for approximately 100 ms. Full details of these experiments are discussed in other work.[70,71] The tests were run at the two operation points outlined in the top half of Table 5.1. To provide the best possible basis for comparison, the power levels between the two cases were matched instead of the volumetric or mass flow rates. Comparing the two propellants by matching the power is useful from a mission analysis standpoint while also resulting in similar neutral number densities for krypton and xenon.[70] To keep the same power, the discharge voltage was kept at the same value and the injected mass flow rate of the neutral propellant was adjusted to match the discharge current. The magnetic field configurations were not kept the same between the two cases, but were rather optimized for maximum efficiency at the same power level for both propellants.

The hydrodynamic model is applied to the NASA-173Mv1 thruster to analyze the effects of the two different propellants. The one dimensional magnetic field approximation outlined in Section 3.1.5.1 is used for this study. For both cases, the Bohm mobility term is ignored while a coefficient of 6.0 is applied to the wall collision frequency term. These values are chosen to provide the best match to experimental observations for the potential drop within the thruster. The mesh consists of 190×127 square cells 0.2 mm on a side and represents an axisymmetric domain stretching from the anode to the exit plane, bounded by the inner and outer walls of the acceleration channel. The running time for a simulation requires only a few minutes to reach a representative steady-state solution on a modern single processor desktop computer. The simulation is run with this geometry for both cases of xenon and krypton. In addition to the externally applied differences between the two cases, namely the mass flow rate and the magnetic field profile, the intrinsic differences between the two propellants are also modeled. The relevant values are given in the bottom half of Table 5.1. The ionization energies are for the transition from ground state neutral atom to singly-charged ion. Both the ionization and momentum exchange collision cross sections are dependent on the electron temperature, but representative constants are chosen based on the range of expected electron temperatures within the thruster.[31,55,99]

5.1.1.2 Results

The contour plots of the density and potential fields for the two cases are displayed in Figs. 5.1–5.4. The potential profiles along the channel centerline are shown in Fig. 5.5 for both the experimental data and the model results. The associated error bars for the

	Xe	Kr
V_d [V]	500	500
I_d [A]	9.27	9.27
$\dot{m}$ [mg/s]	10.00	7.77
m_i [kg]	2.18×10^{-25}	1.39×10^{-25}
E_{ion} [eV]	12.1	14.0
σ_{ion} [m^2]	3.6×10^{-20}	2.7×10^{-20}
σ_{en} [m^2]	35×10^{-20}	25×10^{-20}

Table 5.1: Comparison between the xenon and krypton cases for the NASA-173Mv1 thruster.

experimental results, based on the potential drops across the emissive probe presheath and the floating heater power supply, are also shown.[72] The hydrodynamic model does a fairly good job of capturing the overall potential drop within the thruster for the two cases, roughly 175 V for krypton and 275 V for xenon. However, the model fails to accurately capture the steep profiles of the potential drops as well as the location of the start of the acceleration region. The experimental results show a well defined location of where the acceleration region begins and it is clear that for krypton it lies further downstream than xenon. The results of the model stretch the potential drop over a larger region within the thruster. There is no clear demarcation of the start of the acceleration zone, and the two propellants show little difference until a potential drop of more than 50 V has already occurred. Experimental results also show that in addition to starting further upstream, the acceleration zone for krypton is longer than that of xenon. The model does not extend past the exit plane of the thruster, but it can be inferred from the potential profiles within the thruster that, qualitatively, the model also reflects this observation. The longer acceleration region for krypton contributes in part to the greater beam divergence observed for krypton which in turn affects its overall performance.

The above points are made clearer if the axial electric fields are compared. The experimental electric field values are calculated from the measured potential profile and the associated error is based on the error of the plasma potential measurements. Again, it is seen, in Fig. 5.6, that the simulation results show a wider and less sharply

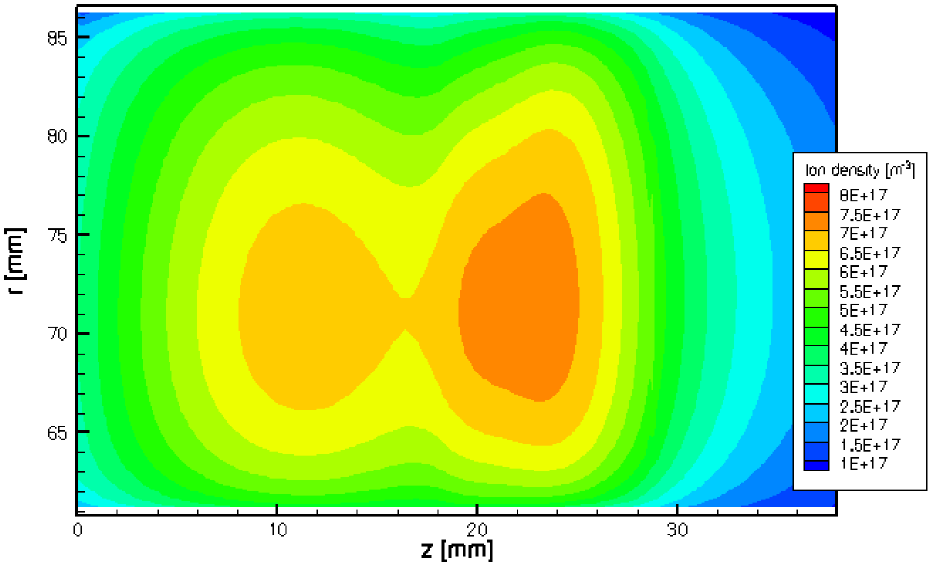

Figure 5.1: Simulated plasma density contours for the xenon case.

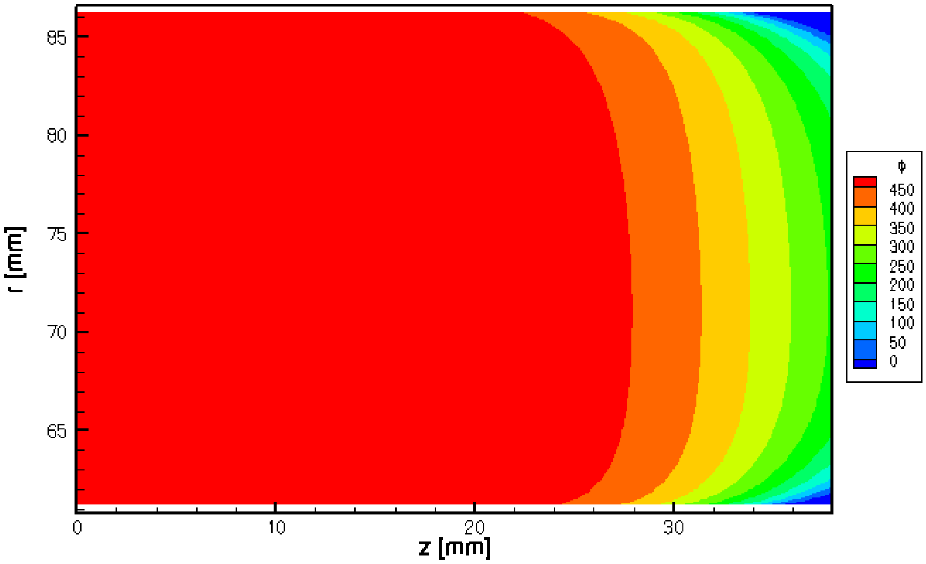

Figure 5.2: Simulated potential contours for the xenon case.

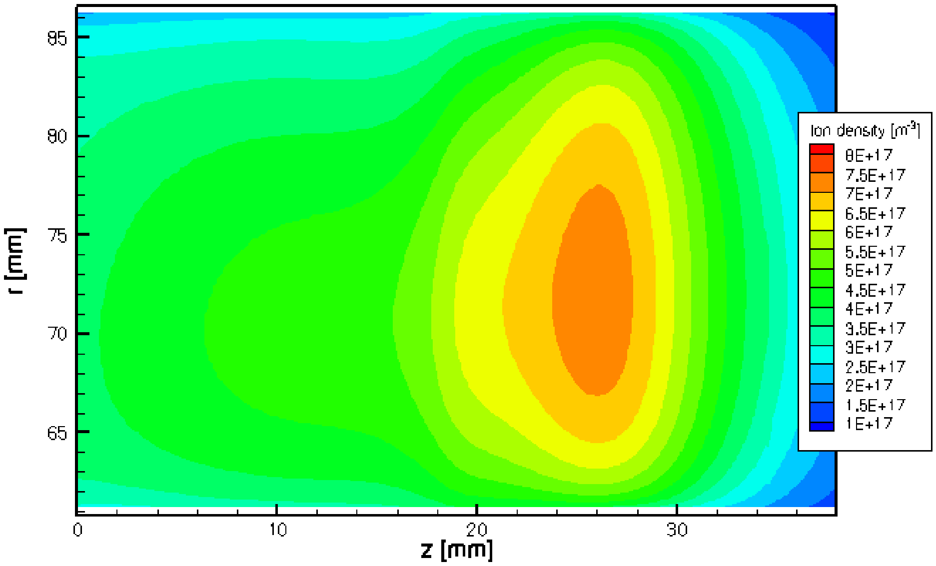

Figure 5.3: Simulated plasma density contours for the krypton case.

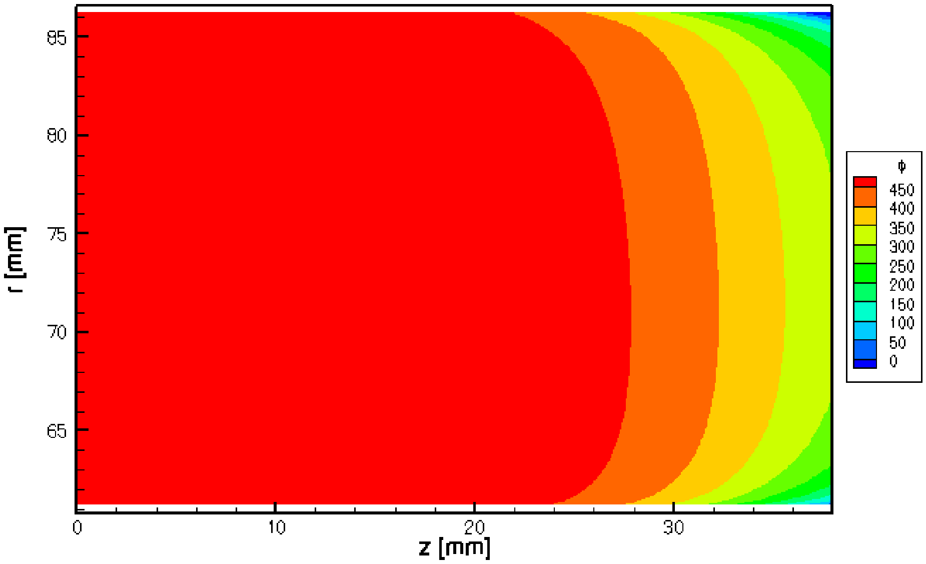

Figure 5.4: Simulated potential contours for the krypton case.

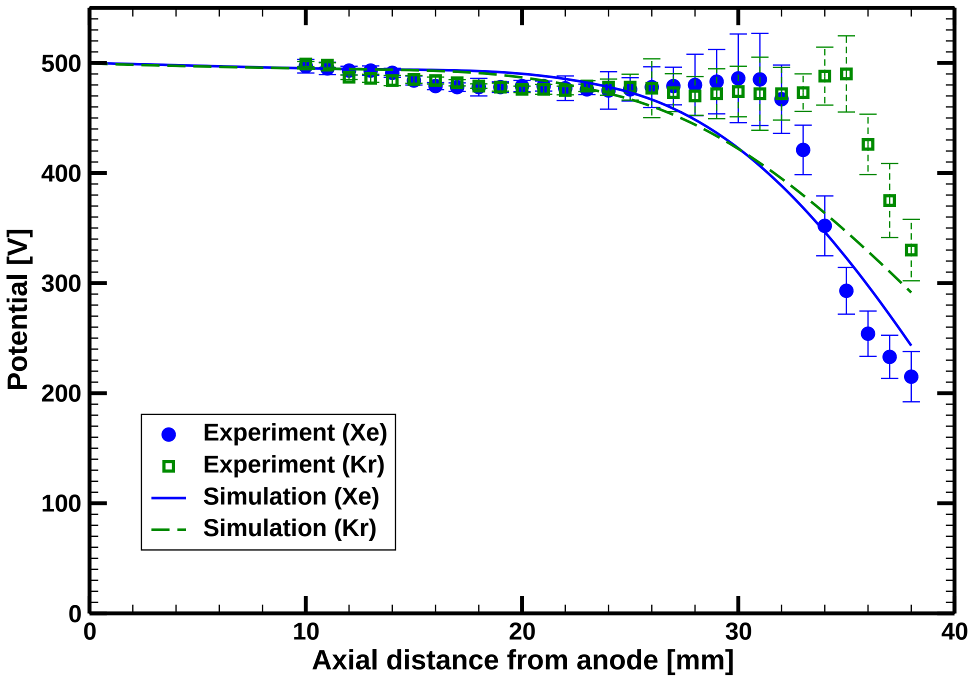

Figure 5.5: The channel centerline potential from anode to thruster exit plane for xenon and krypton for the NASA-173Mv1 thruster.

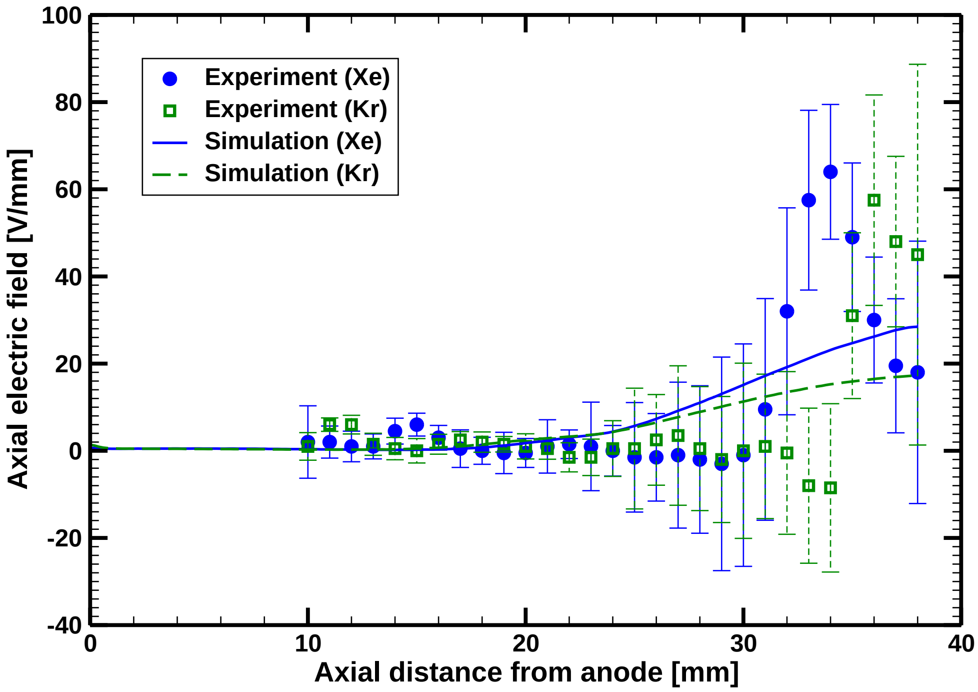

Figure 5.6: The axial electric field along the channel centerline for the NASA-173Mv1 thruster.

defined acceleration zone than do the experimental results. The electric field begins to rise earlier upstream within the model, while the peak is further downstream, past the exit plane. Comparing between the xenon and krypton again, the peak electric field is notably lower for krypton than for xenon in the simulation results, while experimentally the difference between the magnitudes of the peaks is not as significant. Overall, the model underpredicts the electric field in the acceleration region.

The electron temperatures along the channel centerline are also compared. Figure 5.7 displays the results. The error of the electron temperature measurements reflect a tendency for overestimation.[72] The peak temperatures calculated by the model are still somewhat low, however. The model also does not capture the axial location of the peak accurately, especially for xenon. However, the model does predict the axial location of where the electron temperature begins to rise for the xenon case, and to a lesser extent, the krypton case. It does not capture the same profile of a sharper rise in temperature, but rather stretches the temperature increase over a broader axial range, similar to the trends seen in the potential and electric field results.

The axial electron and ion currents are plotted in Fig. 5.8 for the two cases. As expected, the electron current dominates in the region closer to the anode. The drop in the electron current, resulting from a lower cross-field electron mobility, is more pronounced in the xenon case. This corresponds with the higher electric field seen for xenon as well. As the electrons are restrained from freely moving upstream, an electric field arises which accelerates the ions downstream, keeping current conserved. For the krypton case, the decrease in the electron current is more gradual and to a lesser extent overall compared to the xenon case.

Breaking down the differences between the two cases requires further investigation of the possible underlying reasons. One of the benefits of using modeling techniques is the ability to easily change characteristics of the simulations to run virtual experiments, even those that would be difficult or impossible to perform physically. For this specific scenario, the differences between the two propellant cases, presented in Table 5.1, can

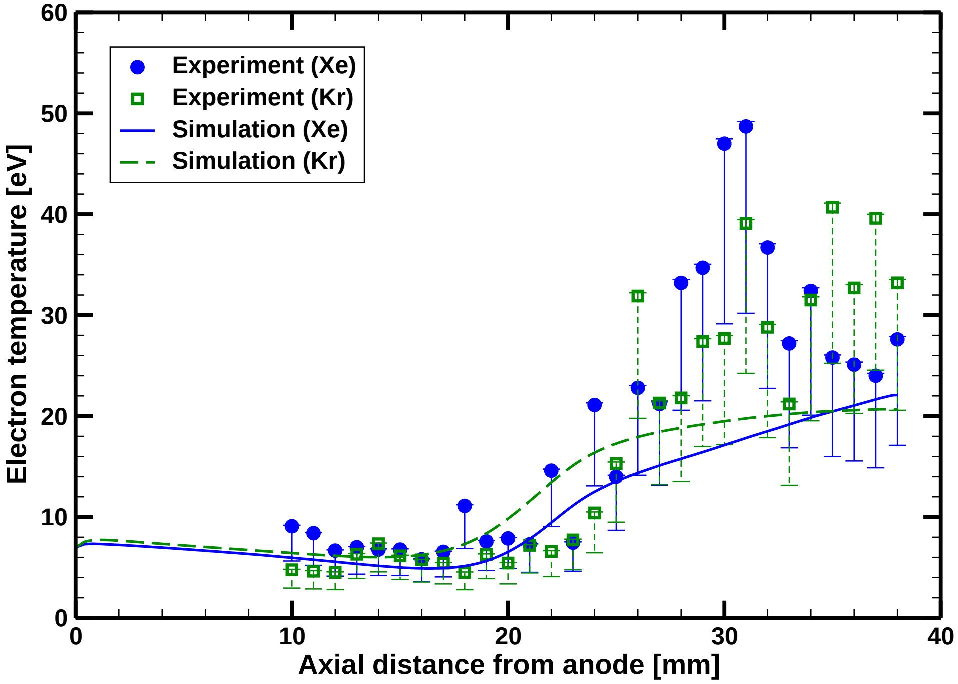

Figure 5.7: The electron temperature along the channel centerline for the NASA-173Mv1 thruster.

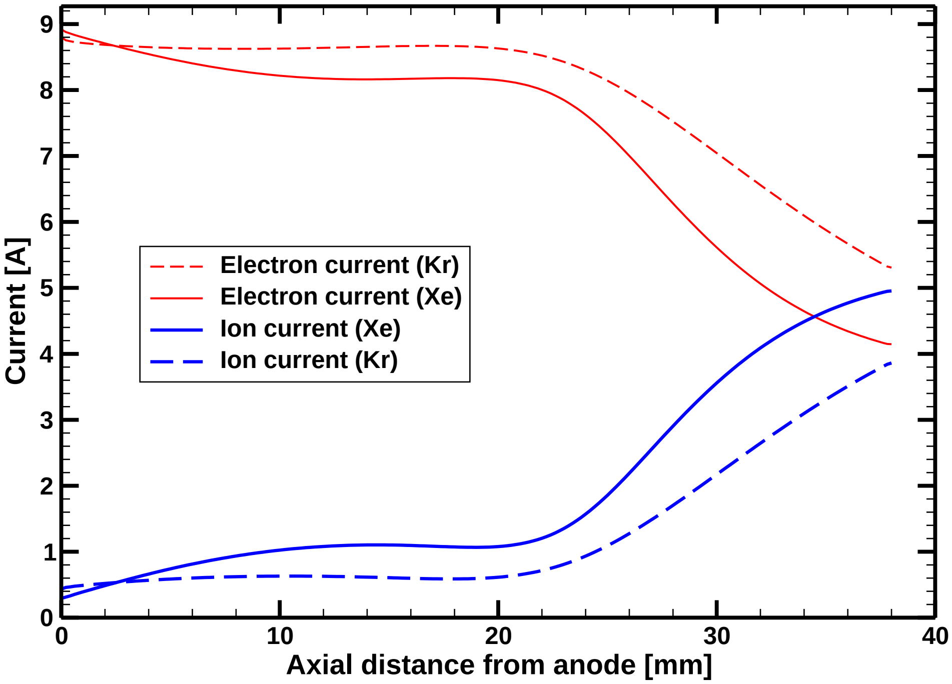

Figure 5.8: The calculated axial electron and ion currents for the NASA-173Mv1 thruster.

be separated into two categories. First are the properties inherent to the two propellant species. These include the atomic mass, collision cross sections, and ionization potentials. The second category includes the externally applied differences, namely the mass flow rate and the magnetic field configuration. Since the mass flow rate is set to match the power levels of the two cases, it is left unmodified. The magnetic field is altered, however, and its effects on the resulting flow are observed.

5.1.1.3 Ionization Rate Considerations

The implemented ionization rate, as given in Eq. (3.30), is a function of the electron temperature and of the propellant species as seen in Fig. 5.9. The shapes of the volumetric ionization rate profiles along the channel centerline, shown in Fig. 5.10, mirror to some degree that of the electron temperature profiles shown in Fig. 5.7 for the two cases. The effects of the lower ionization potential and larger ionization cross section for xenon are clearly seen especially in the downstream portions of the channel. The model does not capture a narrower ionization region, however, as the peak of the calculated ionization rate lies beyond the exit plane. This is due to the similar trends seen in the calculated electron temperature profile for both propellants.

Two aspects of the propellant species affect the ionization rate, the ionization collision cross section and the ionization energy. The ionization collision cross section indirectly represents how likely a neutral gas atom is to encounter an electron impact ionization collision. The collision cross section is proportional to the collision rate and therefore larger values will lead toward a greater number of collisions. The ionization energy is the amount of energy needed to free an electron from a neutral gas atom. Higher energies will tend to lead to lower ionization rates, especially when the electron temperature is on the order of, or lower than, the ionization energy. Since krypton has smaller ionization collision cross sections and a higher ionization energy, both of these aspects contribute to a lower overall ionization rate. To investigate the extent these two parameters affect the ionization rate, simulations are run using the same settings for the original xenon case except the ionization collision cross section and the ioniza-

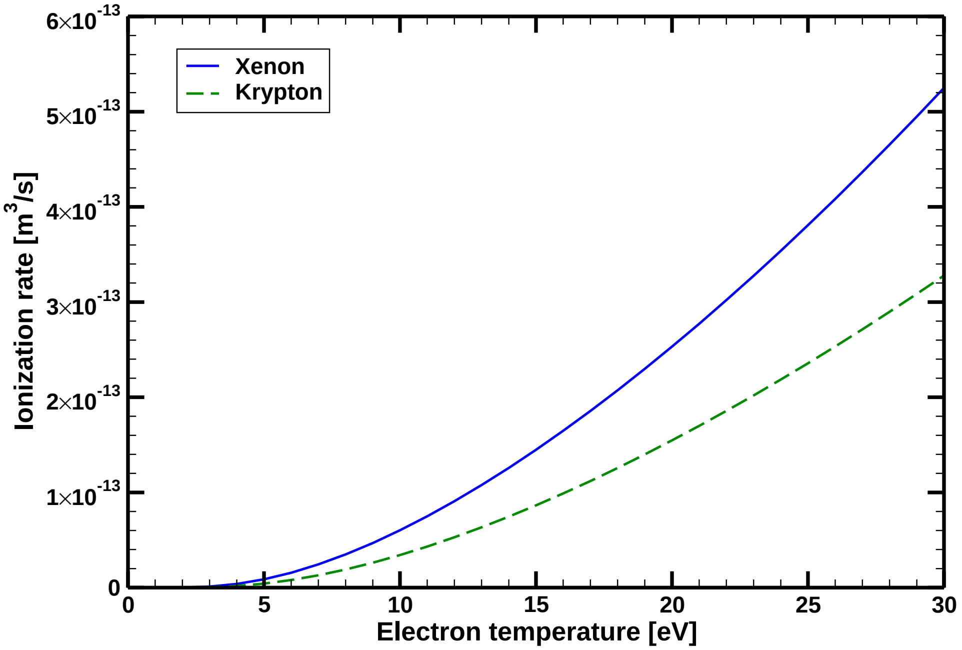

Figure 5.9: The calculated volumetric ionization rate for krypton and xenon as a function of electron temperature.

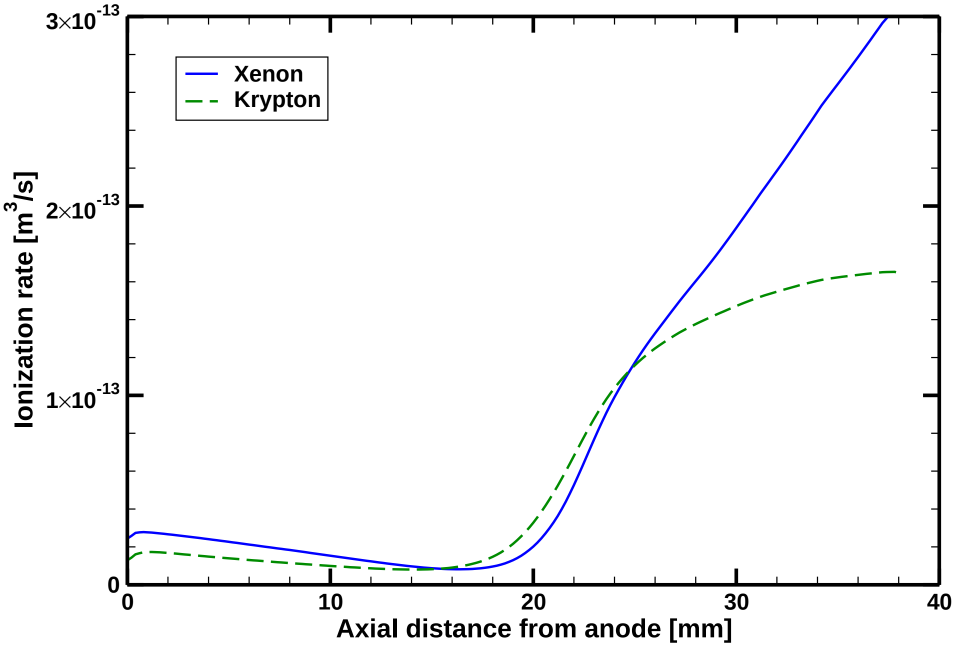

Figure 5.10: The calculated ionization rate along the channel centerline.

tion energies are artificially altered separately to those of krypton. Though the electron temperature profiles, shown in Fig. 5.11, are not significantly affected, there are still considerable effects on the ionization rate as seen in Fig. 5.12. The ionization collision cross section of krypton plays a slightly larger role in reducing the ionization rate than does the ionization energy. As expected, the inherent characteristics of krypton play a significant role in reducing the ionization rate, which in turn contributes to a lower propellant utilization and subsequent loss in performance.

5.1.1.4 Magnetic Field Profile Considerations

Though nothing can be done to change the intrinsic ionization collision cross section or the ionization energy of krypton, the magnetic field profile is one aspect that thruster designers can adjust to try to improve performance. To see the effects of the magnetic field on the performance between the two cases run for the NASA-173Mv1 thruster, the hydrodynamic model is used to simulate a scenario where the original settings for the xenon case are kept except for the magnetic field profile, which is changed to the one used for the krypton case. This is performed to examine the extent the magnetic field profile used for krypton contributes towards lower performance.

The effect of the magnetic field profile on the electron temperature and ionization rate are shown in Figs. 5.13 and 5.14, respectively. Though the ionization rate is not directly dependent on the magnetic field profile, the ionization rate profile along the channel is clearly seen to be significantly affected by the change in the magnetic field. This is due to the change in the electron temperature profile. As noted earlier, the shape of the ionization rate profile strongly mirrors that of the electron temperature profile. The electron temperatures of the xenon case with the krypton magnetic field profile are lower overall particularly near the exit plane. They are closer in value to the original krypton case in that region. Correspondingly, the ionization rates are also lower for the modified case and generally closer in value to the original krypton case in that downstream region. This reduction of the ionization rates is greater than that seen in Fig. 5.12 when the representative ionization collision cross section or the ionization energy is modified.

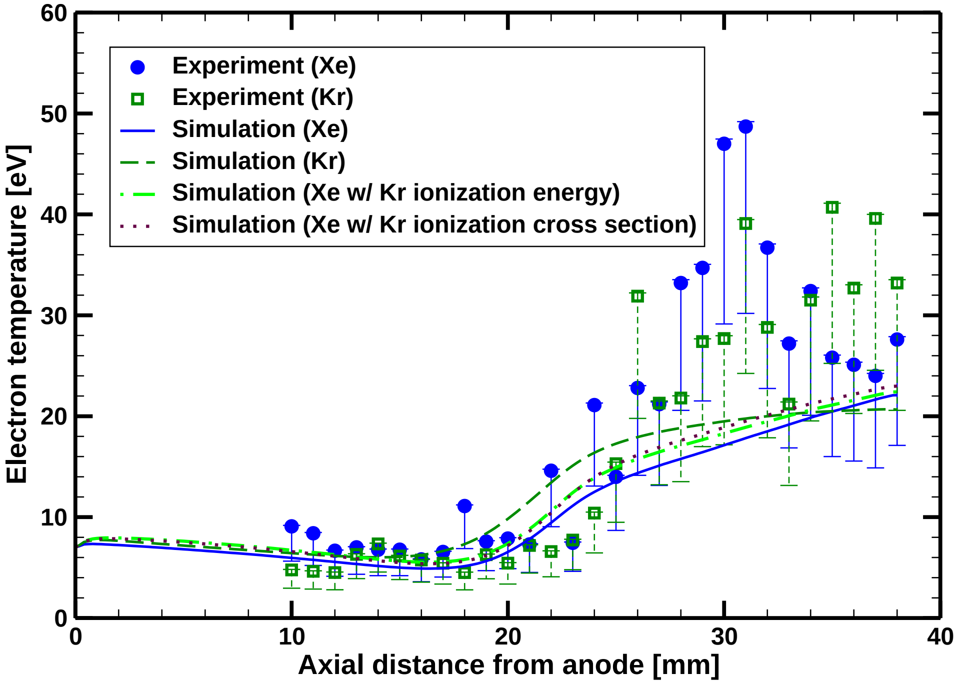

Figure 5.11: The electron temperature profile along the channel when the ionization collision cross section and the ionization energies of xenon are altered.

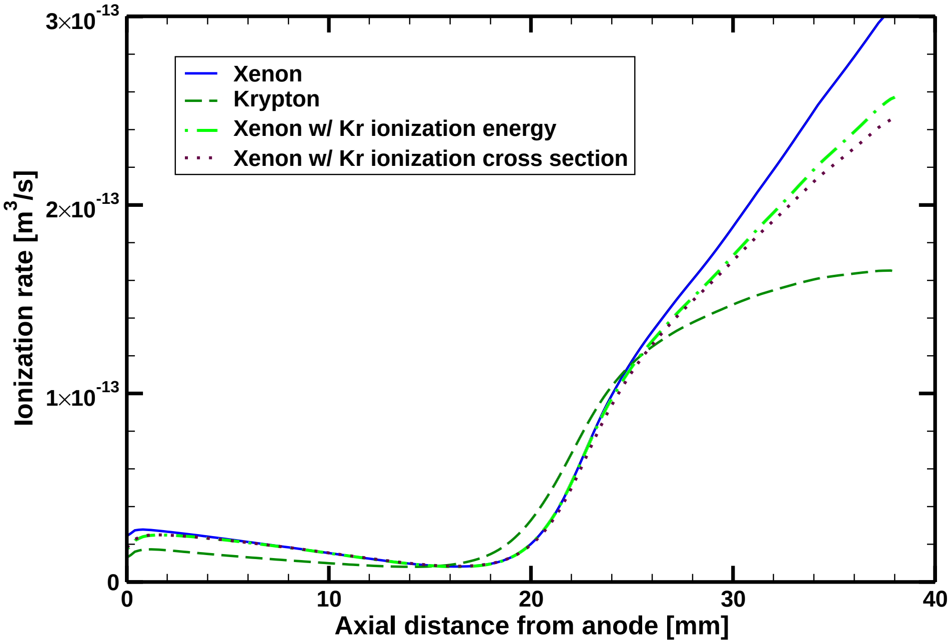

Figure 5.12: The ionization rate profile along the channel when the ionization collision cross section and the ionization energies of xenon are altered.

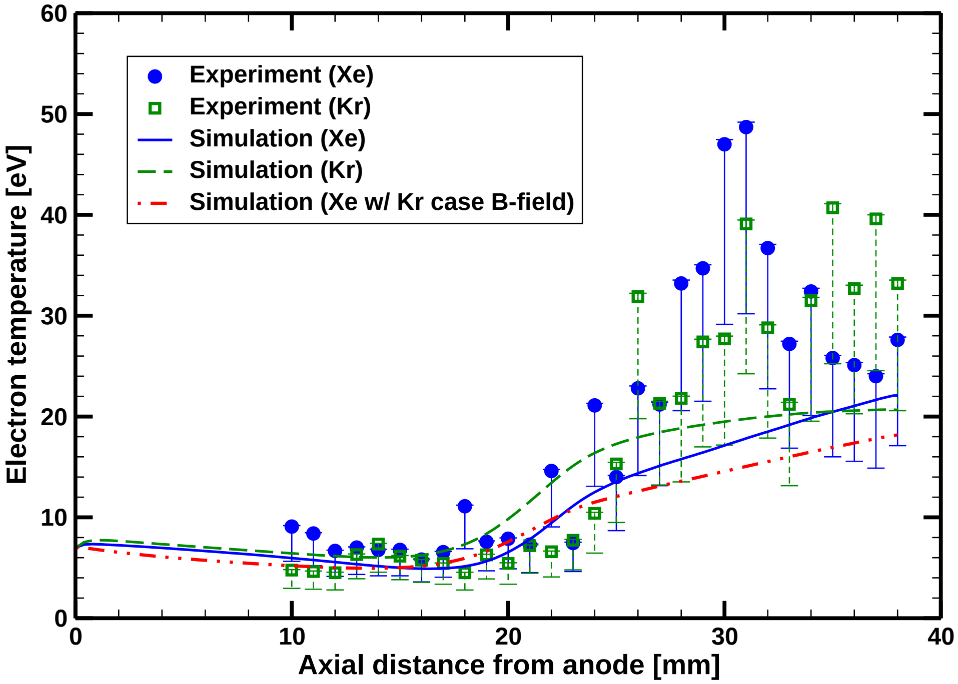

Figure 5.13: The electron temperature profile along the channel when the magnetic field profile is altered.

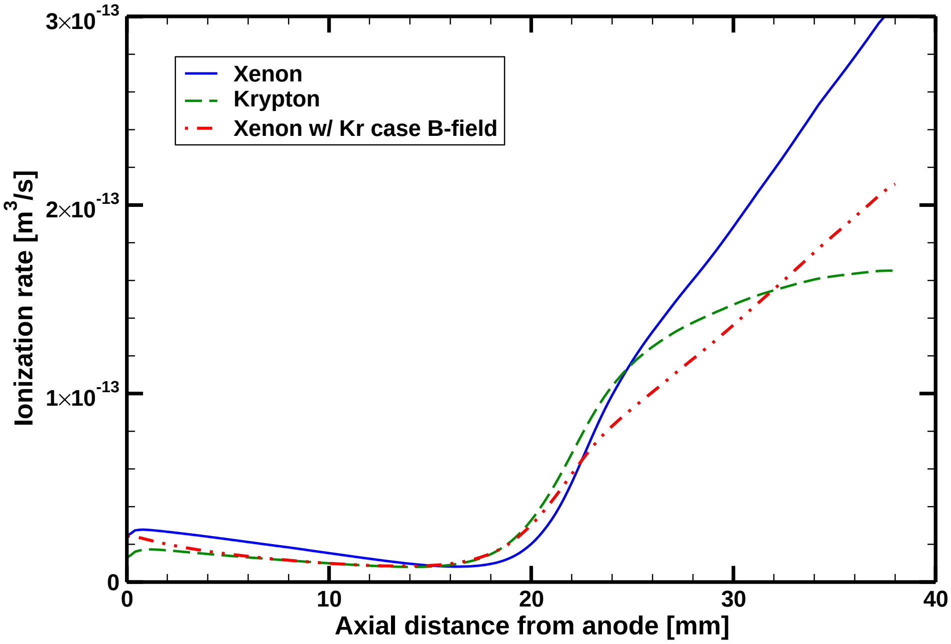

Figure 5.14: The ionization rate profile along the channel when the magnetic field profile is altered.

Thus, the magnetic field configuration certainly plays an important role in performance optimization through propellant utilization as seen from the ionization rate along the thruster channel.

The magnetic field profile also plays a role in affecting the resulting electric field profiles. The most direct effect the magnetic field has in the hydrodynamic model is through the cross field electron mobility presented in Eq. (3.40). The magnetic field configuration for xenon impedes electron mobility across field lines which increases the magnitude of the potential drop, and conversely the magnetic field profile for krypton allows for a greater electron mobility and reduces the change in potential. Thus when xenon propellant is simulated with the magnetic field optimized for krypton, the resulting potential profile, shown in Fig. 5.15, is more comparable to that of the original krypton case than that of the original xenon case. The potential profile for the modified case is considerably worse in some regards than the two original cases. The potential drop is more diffuse and the resulting acceleration region is less defined. A greater portion of the ion acceleration occurs past the exit plane outside of the thruster channel. This can lead toward greater beam divergence and reduced efficiency.

In summary for this section, the hydrodynamic model is used to simulate the plasma flow within the NASA-173Mv1 Hall thruster for two different propellants, xenon and krypton. This analysis is performed to investigate some of the underlying reasons behind the observed performance gap for krypton. The focus of this study is to characterize the extent that the performance gap is attributable to the inherent properties of krypton versus the changes in performance due to externally applied factors. The ionization properties of the two propellants are compared, in particular the ionization collision cross section and the ionization energy are altered for xenon to match the corresponding values for krypton. As expected, this affects the ionization rate, but other properties of the flow, such as the potential and the electron temperature profiles are largely unaffected. Changing the magnetic field for xenon to that of the krypton case, however, does affect the general parameters of the plasma structure and therefore indirectly also

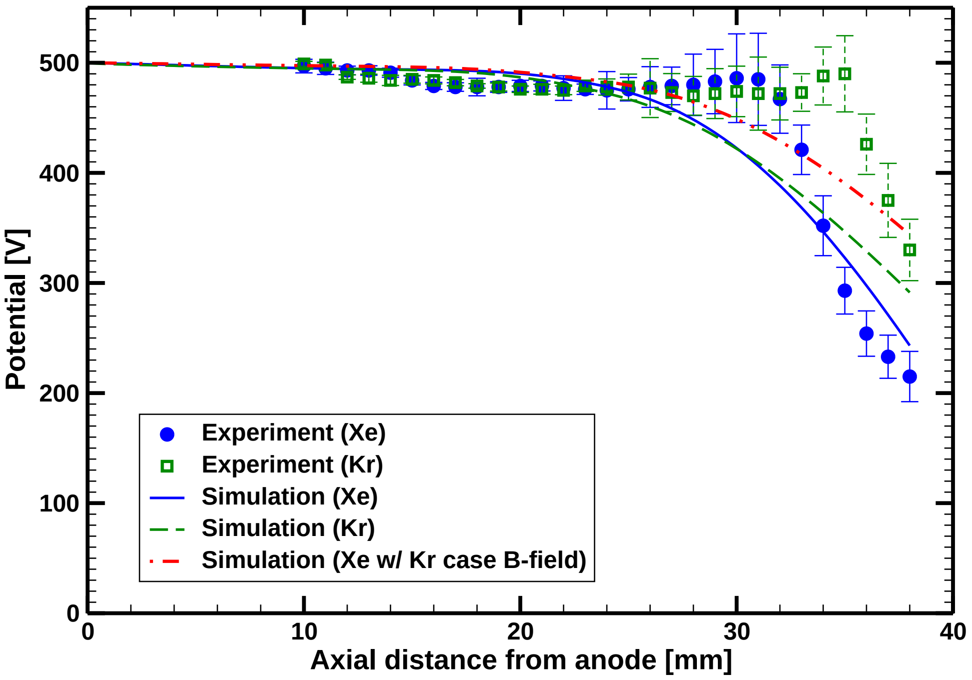

Figure 5.15: The channel centerline potential profile comparing the original and the case with the modified magnetic field for the NASA-173Mv1 thruster.

changes the ionization rate profile. Thus, while the inherent properties of krypton lower the ionization rate in general, thus reducing propellant utilization, the external applied magnetic field profile also affects the acceleration region leading toward greater beam divergence, further lowering the performance. Now, there are many other factors that go into the magnetic field configuration that need to be considered in the thruster design and development process. There are also other parameters that play roles in affecting the performance that are not considered here. However, external adjustable factors play a significant role in determining the performance and it may be possible to reduce the performance gap between the two propellants even to the point where the inherent increased difficulties of ionizing krypton are overcome.

The hydrodynamic model presents a useful means of investigating these properties individually through virtual experiments. There is however much room for improvement in terms of the model capturing experimentally measured aspects of the plasma discharge. Most noticeably the model fails to capture the peaks of the electric field and the electron temperature within the channel. Sharp gradients tend to be smoothed out over a wider range. However, qualitative aspects of the flow, particularly noticeable in comparisons between the two cases, are captured by the model.

5.2 Molecular Dynamics Sputter Model Results

5.2.1 Low Energy Xenon Ion Sputtering of Boron Nitride

The molecular dynamics method is used to model low energy xenon ion impacts onto a boron nitride surface. This is important for Hall thruster erosion applications, but is also of interest for cubic-BN fabrication through thin film deposition.[39] Whether from a propulsive standpoint or a plasma processing perspective, boron nitride sputtering is an area of active research and interest. Previous experimental work performed on BN sputtering started at higher ion energies, from hundreds of eV to keV and higher, mainly because it is easier to obtain data at that energy range.[24,43] However, for Hall thrusters with powers around 1 kW—which translates to a discharge voltage around a few hundred volts—the corresponding range of ion energies impacting the walls will be lower than a couple hundred volts. In that case, the sputtering of wall material due to low energy ions becomes important. Though more advanced and sensitive measurement techniques are being applied to quantify the sputter yields at these levels,[111] modeling techniques offer another approach that can be used to provide additional analysis of the sputter process.

5.2.1.1 Background

There have been several experiments run to obtain sputter yield data of boron nitride from xenon ion impacts. These have involved different groups employing various measurement techniques. Unfortunately, the grade or purity of the boron nitride samples tested is not always reported. This contributes to a rather significant amount of scatter among the sets of sputter yield data.

Yalin *et al.* have worked on three different measurement techniques—weight loss, quartz crystal microbalance, and cavity ring-down spectroscopy—to obtain the sputter yields of boron nitride at low ion energies.[109,110] The weight loss method measures the weight of the BN sample before and after a period of sputtering. The difference in the weight is used to calculate the amount of material sputtered. The quartz crystal microbalance (QCM) offers a sensitive measurement of the mass that accumulates on its surface through changes of the resonant frequency of the quartz crystal. The QCM is swept over the sample as it is sputtered, measuring the differential sputter yield at various angles around the sample surface. The differential sputter yields are integrated to calculate the total sputter yield. It should be noted that the QCM is only able to detect products that condense on its surface. For BN this includes atomic boron and compounds containing boron, but not atomic or molecular nitrogen. Cavity ring-down spectroscopy is another method to increase the sensitivity of sputter measurements. This technology uses the optical absorption of laser pulses to quantify the amount of sputtered particles. A cavity ring-down spectroscopy system to measure BN sputtering is still under development. All of these measurement techniques are used to measure the sputter yields of HBC grade BN. HBC is the grade designation given by General Electric for their highest purity BN products. HBR grade boron nitride, which incorporates calcium borate as a binder substance, was also tested by Rubin *et al.*[95] The measurements were carried out for ion energies ranging from 100 eV to 500 eV for both the weight loss and the QCM method. However, for the weight loss method, measurements made for ion energies below approximately 150 eV approach or go beneath the detection limit determined by the noise floor.[110]

Garnier *et al.* also performed weight loss experiments to measure the sputter yield of BN from low energy xenon ions.[43] They do not specify any characterization of the BN sample tested except that it was obtained from pyrolysis. In addition to BN, they also measured sputter yields for BN with aluminum nitride (BNAlN) as well as BN with silicon oxide ($BNSiO_2$). The sputter yields were measured for ion energies ranging from 350 eV to 1 keV and across a range of incidence angles. They also performed an analysis of surface properties before and after sputtering.

Britton *et al.* used laser profilometry to determine sputter yields of boron nitride.[24] After the initial surface of the sample underwent sputtering, a laser was used to measure the depth of the eroded profile. Then the eroded volume was calculated to determine the sputter yield. This technique differs from the weight loss and the QCM method in that it directly calculates a volumetric sputter yield instead of a mass-based sputter yield. There is no mention of the grade or any other characteristic of the BN samples used for the experiment. Sputter yields resulting from ion energies ranging from 300 eV to 1000 eV were measured.

Abgaryan *et al.* also present sputter yield data for boron nitride in addition to those for borosil and alumina.[1] Though sputter yield data from roughly 100 eV to about 400 eV is presented, there is very little mention about the methodology and other details on how the data were obtained. They used an SPT thruster as the ion source, but nothing about the procedure by which the sputter yields were determined is described.

5.2.1.2 Total Sputter Yields

The total sputter yields are found as an average of the sputtering that occurs from a single ion impact. The response from a single ion impact on a surface can vary from no sputtering to multiple molecules escaping the surface. There are a large number of variables that can affect this result such as the exact location the ion impacts and the configuration of the atoms of the surface including surface roughness effects. From a practical standpoint, however, only the average sputter yield observed over a very large number of impacts is necessary. The variable factors that still need to be accounted for then are the ion energy, the incident ion trajectory angle, and the surface material. Here, the material is restricted to pure hexagonal boron nitride. The ion incident angle is also mostly restricted to 45 degrees from the surface normal. The focus of this part of the study is to determine the energy dependence for the sputter yields of boron nitride.

The molecular dynamics model is used to simulate hundreds of ion impacts onto a boron nitride surface. Ion energies ranging from 10 eV to 100 eV in increments of 10 eV are tested as well as 150 eV, 250 eV, and 350 eV. For ion energies at 100 eV or below, a BN domain size of 7.8 nm × 7.8 nm × 2.5 nm consisting of 18144 atoms is used. For the 150 eV case, a domain size of 10.4 nm × 10.4 nm × 3.0 nm of 38400 atoms is used. The 250 eV and 350 eV cases use the 13.0 nm × 13.0 nm × 3.0 nm block with 60000 atoms.

For the 150 eV and lower ion energy cases, domain size independence is established by running a sample case on a larger domain size and obtaining similar results. Due to computational time constraints, domain size independence is not completely established for the 250 eV and 350 eV cases. Typically, 30 to 45 minutes of wall clock time are required per ion for the lowest domain size on a dual processor machine. For the largest domain size used, roughly 3 to 4 hours are required per ion on the same system. The temperature of the BN surface is regulated to 150°C, or 423 K, as that is the temperature reported by Garnier *et al.*,[43] Yalin *et al.*,[110] and Rubin *et al.*[95] The temperatures of the BN samples are not reported in any of the other experimental work.

The total sputter yields, both experimental and simulated, with a 45° ion incident angle are plotted in Fig. 5.16. The error of the experimental results, if reported, is presented. For the simulation results, the error bars represent the standard deviation of the sputter data collected at that ion energy. Typically 300 ion impacts are simulated to obtain the data at each of the ion energies tested. Only 200 ion impacts are tested at 250 eV and 350 eV, while an extended run of 1500 ion impacts is tested at 50 eV. A few notes about the data presented should be mentioned. For the data from Abgaryan *et al.*,[1] neither the experimental procedure nor the ion incident angle that the data were obtained at is known so their results are not presented here. The data obtained by Britton *et al.*[24] are at an incidence angle of 40° from the surface normal, while the other sets of data are obtained at 45°. The datum point by Rubin *et al.*[95] at 100 eV falls below the detection limit presented by Yalin *et al.*[110] using the same experimental techniques and procedures. Finally, there are two sets of data presented by Yalin *et al.* for the QCM measurements. The 'QCM low' values are the actual values from the QCM measurements. However, these include only condensible products and underestimate the actual BN sputter yield. Yalin *et al.* also include what they believe to be a more accurate estimate by assuming equal stoichiometry between atomic boron and nitrogen, which is represented by 'QCM high' in Fig. 5.16.

There is a substantial amount of scatter among the experimentally obtained data.

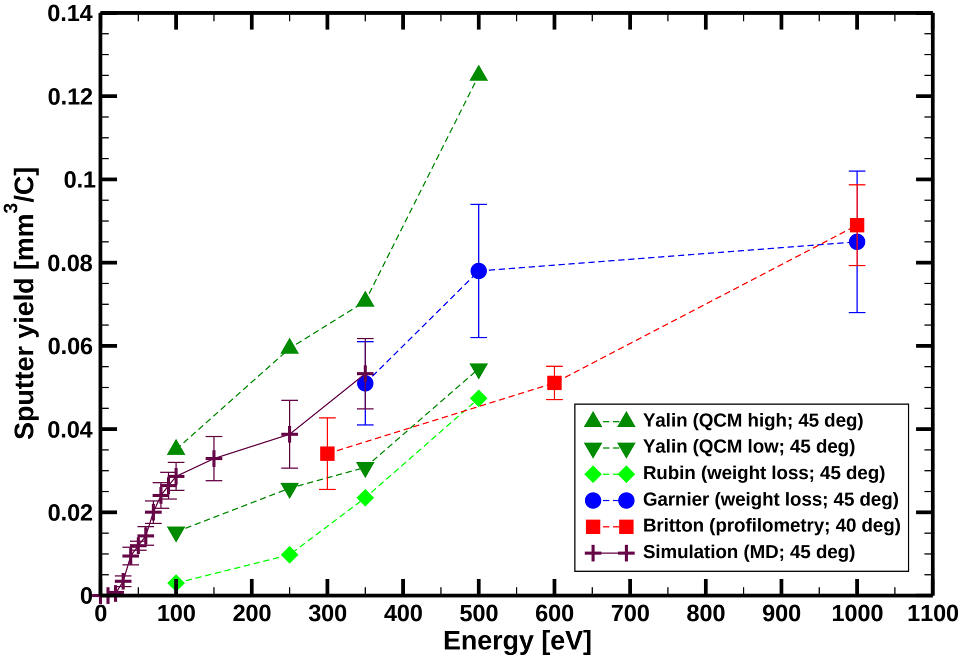

Figure 5.16: The total BN sputter yield versus ion energy with an ion incidence angle of 45 degrees.

This is to be expected to some degree, however, from all of the caveats described above. Whether the grade or purity of the BN samples are unclear, or the incidence angle of the ion beam is different, or the temperature of the samples may differ, or the quality of the ion source, or any other number of possible factors, there are certainly several possible reasons behind the discrepancies among the experimental results.

The molecular dynamics simulation results are for pure h-BN, which correspond the closest to the HBC grade of BN as reported by Yalin *et al.* and Rubin *et al.* Unfortunately, their measurements have a significant disparity between the two methods used: the QCM and weight loss. The molecular dynamics model calculates sputter yields that are higher than those measured by the weight loss method, but lower than the estimated values given by the 'QCM high'. When just the condensible products, atomic boron and compounds containing boron, are considered from the results of the MD simulations, the values are in good agreement with the condensible results actually measured by the QCM, as seen in Fig. 5.17.

Curve fits are applied to the data calculated using the molecular dynamics model

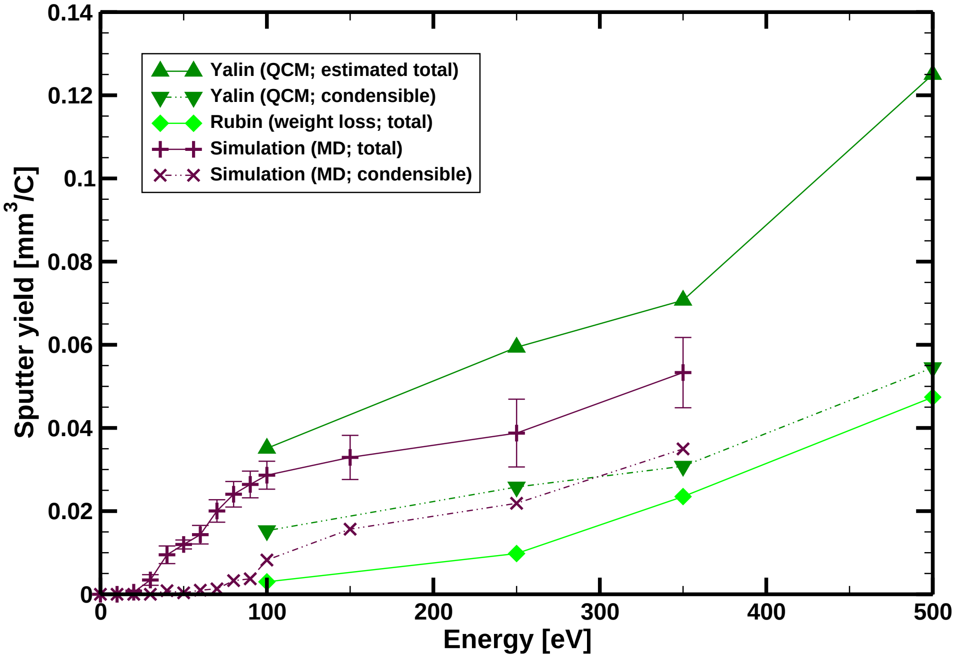

Figure 5.17: Comparison of the condensible sputter yields.

in order to produce a form that is useful for erosion modeling. The semi-empirical fits from Section 2.4.1 are used to provide an expression for the sputter yields. Two separate fits are applied to the MD results. The quantum-statistical approach used by Wilhelm was derived specifically for the very low energy sputter yields near the threshold value. Though the quantum-statistical analysis is claimed to be valid for ion energies below about 100 eV, the fit tends to deviate more so as ion energies approach 100 eV.[108] Thus, the quantum-statistical analysis fit is used for ion energies at 50 eV and below. A least squares fit of Eq. (2.21) is applied to the MD data and shown in Fig. 5.18. The values of the coefficients are altered slightly to match with the fit used for the 50 eV and higher data described below. This results in a threshold energy of 13.0 eV and a value of 7.62×10^{-6} for A.

For ions with energies higher than 50 eV, the fit formula by Zhang and Zhang, modified from Sigmund's original work, is chosen as it is tailored towards low energy sputtering.[119] Though at the very low energies near the threshold energy it does not capture the concavity of the yield profile, it provides a generally good fit at higher

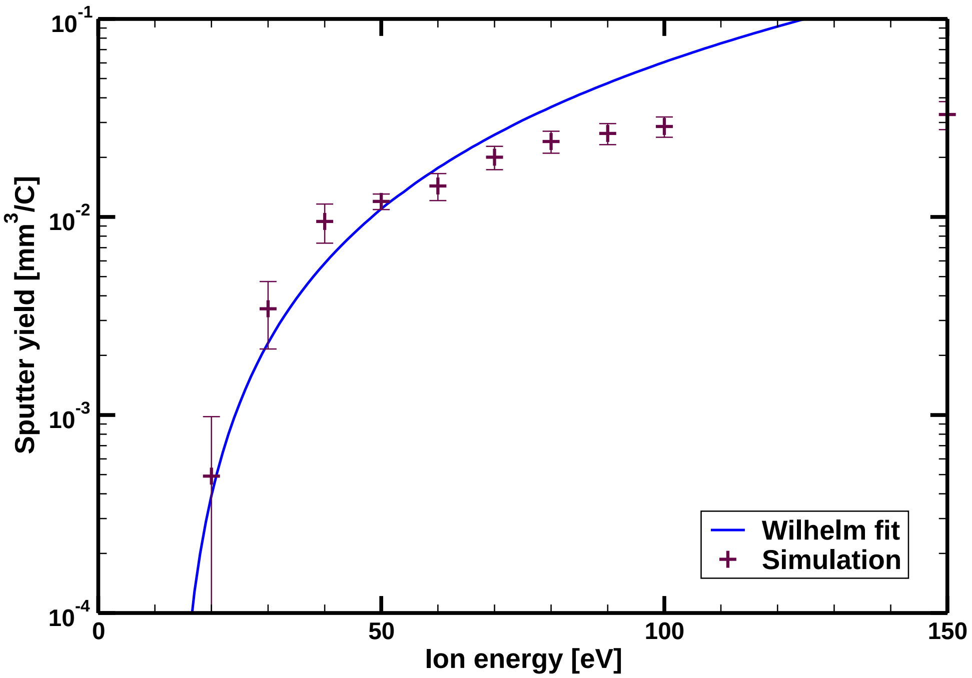

Figure 5.18: A fit based on quantum-statistical analysis applied to the simulation sputter yield data.

energies. A least squares fit is applied using the qualitative form of their equation, given in Eq. (2.13). The coefficient A is set to 0.205 and E_{th}—here not necessarily the threshold energy, but rather a fitting energy—is set to 70.8 eV. The resulting curve is shown in Fig. 5.19 along with the simulation data and the previous quantum-statistical fit. The fit formulae are reprinted here for clarity:

$$Y = \begin{cases} 7.62 \times 10^{-6} \left(E - 13.0\right)^2 & E < 50 \text{ eV} \\ \frac{0.205 \ln(1+1.1383(E/465.0))}{2(E/465.0+0.01321(E/465.0)^{0.21226}+0.19593(E/465.0)^{0.5})} \left(1 - \sqrt{\frac{70.8}{E}} \cos\frac{\pi}{4}\right) & E \geq 50 \text{ eV} \end{cases} \tag{5.1}$$

for ion energies, E, in eV. Equations (5.2) and (5.1) are valid for calculating sputter yields of boron nitride at 423 K resulting from xenon ion impacts occurring at a 45° incidence angle.

If a single function is preferred, the Bohdansky formula from Eq. (2.6) can be used. This formula is based on the work of Sigmund, which was developed based on higher energy ion sputtering, but Bohdansky alters Sigmund's formula with a focus on matching low energy data. The Bohdansky fit also features an inflection point between the very

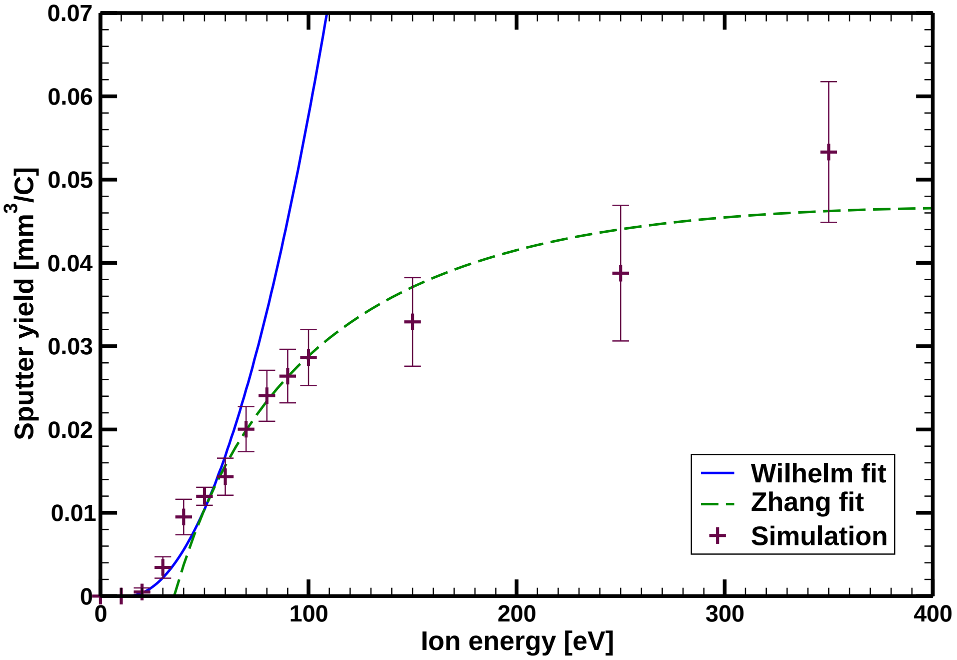

Figure 5.19: The Wilhelm and Zhang fits applied to the simulated sputter yield data.

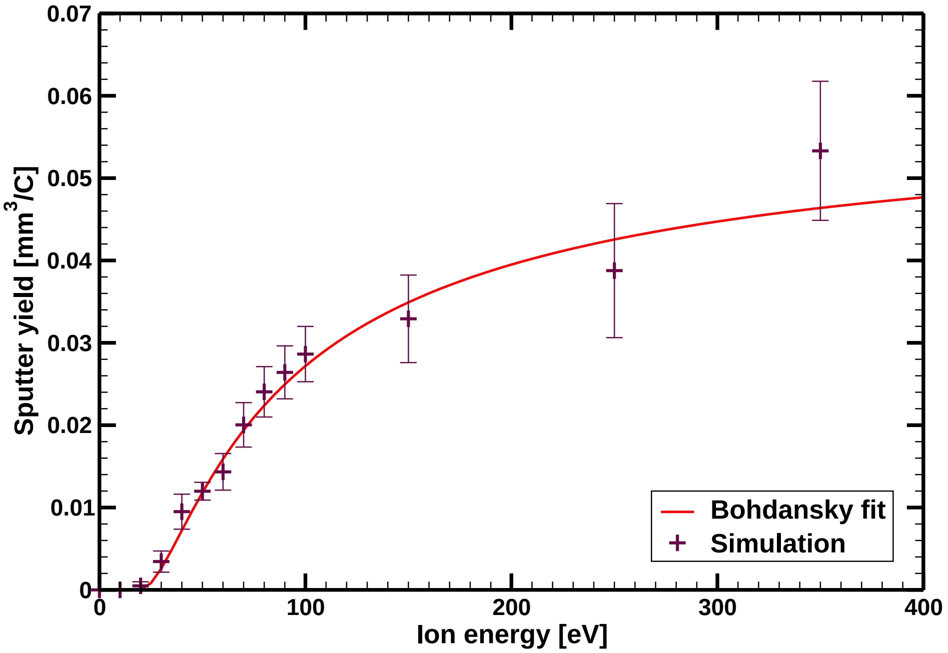

Figure 5.20: The Bohdansky fit applied to the MD results.

low energy data and yields at higher energies.[18] A least squares fit of the Bohdansky expression is applied to the MD results and shown in Fig. 5.20. A coefficient to the overall equation is set to 0.06 and the threshold energy, E_{th} is set to 18.26 eV. The resulting expression is then

$$Y = 0.06\left[1 - \left(\frac{18.26}{E}\right)^{2/3}\right]\left[1 - \frac{18.26}{E}\right]^2 \tag{5.2}$$

In addition to a dependence on the ion energy, the total sputter yields also depend on the ion incidence angle with the surface normal. A set of simulation results ranging from normal incidence to 85° from the surface normal is presented in Fig. 5.21. Experimental data are also shown.[43, 95, 109, 110] Each set of data is normalized by their respective values at 45° incidence. Roughly 300 simulated 50 eV ion impacts are performed for each simulation datum point. The experimental data are obtained at higher ion energies, where diamonds represent 100 eV, squares represent 250 eV, and circles represent 350 eV in Fig. 5.21. For the sets of results in general, the sputter yield generally tends to slightly increase from normal incidence to 45° incidence. A peak is observed around 60°–75° incidence, and a sharp drop off is seen as the incidence angle approaches a trajectory parallel to the surface. There does not seem to be any particular trends that result from different ion energies, but again there is a large amount of scatter present among the different sets of results which makes it difficult to extract definitive conclusions.

Often a normalized form of the angular dependence is used in conjunction with the energy dependence to calculate the total sputter yield based on both energy and angle. For the Hall thruster erosion model, the semi-empirical Yamamura curve fit presented in Eq. (2.18) is used to provide an expression for the normalized angular dependence.[112] Following the work of Cheng *et al.*, the Yamamura fit is applied to the 250 and 350 eV Yalin data with coefficients of $f_s = 5.97563$, $\Sigma = 1.41355$, and $E_{th} = 13.234$ eV normalized by the value at 45° incidence.[26, 110] The Yalin data, as well as the MD results, are shown with the Yamamura fit in Fig. 5.22. The MD results are show higher relative sputter yields compared to the curve fit, but since the Yamamura expression has

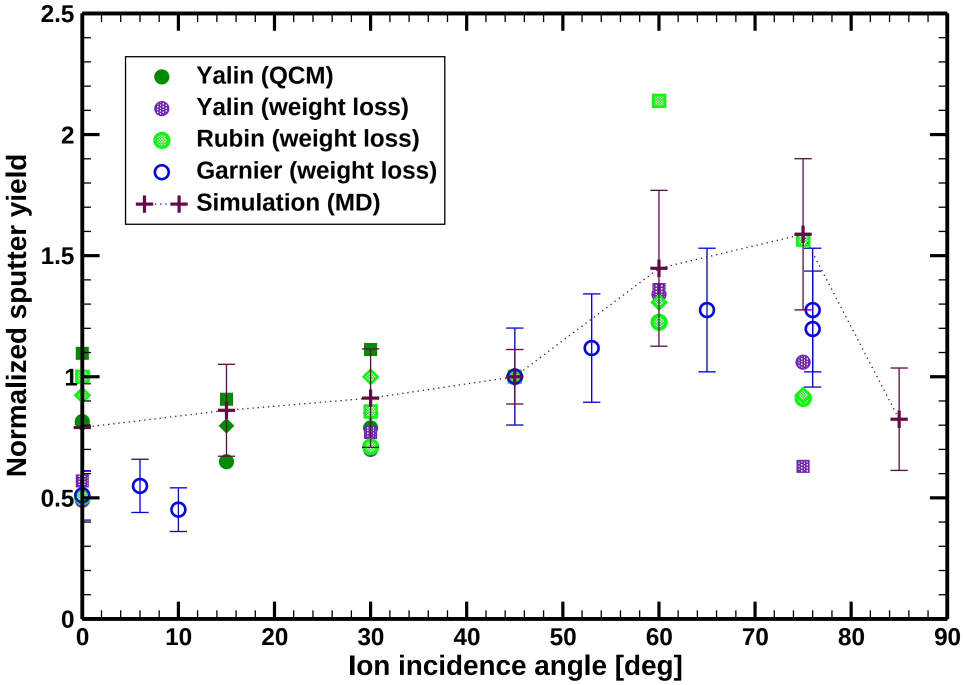

Figure 5.21: Normalized sputter yield dependence on incidence angle.

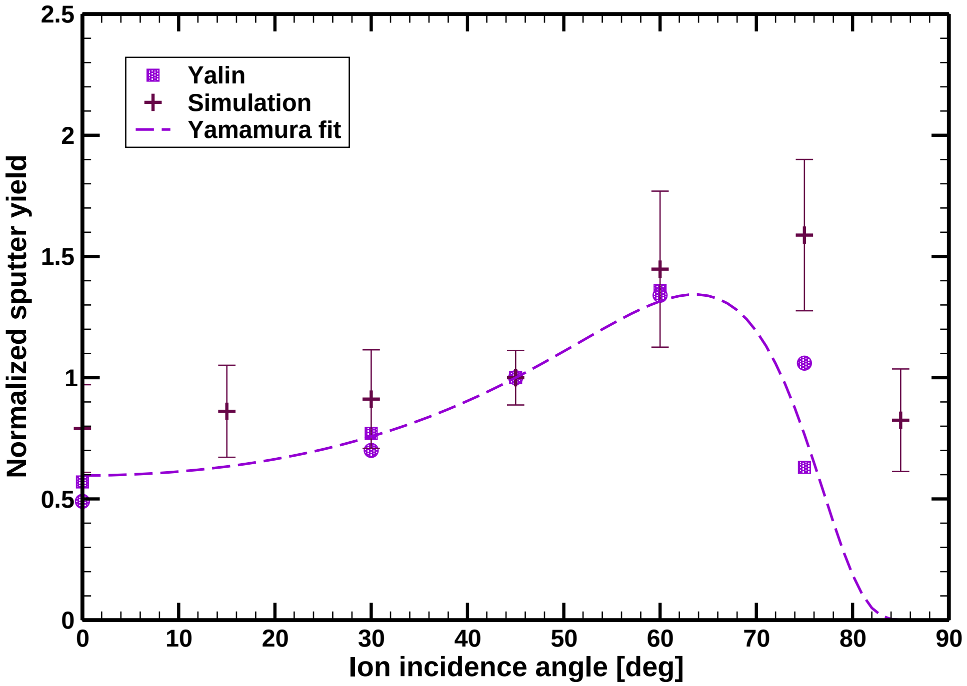

Figure 5.22: Normalized experimental sputter yield with polynomial curve fit for angular dependence.

been tested against a larger set of sputter yield results of different materials at various ion energies, it is used for the erosion simulations instead of a simpler polynomial fit to the MD data.

5.2.1.3 Differential Sputter Yields

The differential sputter yields are also calculated using the MD method. Differential sputter yields provide an observation on the angular distribution of sputtered particles ejected from the surface. This information is useful in a Hall thruster context for determining possible redeposition of the sputtered material, either back onto one of the channel walls or perhaps onto other spacecraft surfaces outside of the thruster. Yalin *et al.* provide differential sputter yield data collected using a QCM.[110] The QCM is revolved around the sample surface as it is being sputtered. Then the sputtered material leaving at a particular solid angle above the surface can be measured. In the molecular dynamics model, the trajectories of the sputtered particles are tracked to calculate the angle they leave the surface. In the case of sputtered molecules or compounds with more than a single atom, the trajectory of the center-of-mass of the system is tracked.

Yalin *et al.* also apply a fit to their differential data.[110] They use a modified form of expressions formulated by Zhang *et al.* for differential sputter yield profiles.[119] The modified Zhang formula used is

$$\begin{gathered} y = \frac{Y}{1-\sqrt{\frac{E^*}{E}}\cos\theta}\frac{\cos\alpha}{\pi}\left[1-\frac{1}{4}\sqrt{\frac{E^*}{E}}\left(\gamma(\alpha)\cos\theta+\frac{3}{2}\pi\sin\theta\sin\alpha\cos\phi\right)\right] \\ \gamma(\alpha) = \frac{3\sin^3\alpha-1}{\sin^2\alpha}+\frac{\cos^2\alpha\left(3sin^2\alpha+1\right)}{2\sin^3\alpha}\ln\left(\frac{1+\sin\alpha}{1-\sin\alpha}\right) \end{gathered} \tag{5.3}$$

where θ is the ion incidence angle, α is the incidence angle of the sputtered particle, and ϕ is the azimuthal angle of the sputtered atom. The energy of the impacting ion is input as E. The two remaining parameters, Y and E^*, are used to fit the expression to the collected data. Following, Yalin *et al.*'s example, Eq. (5.3) is also fitted to the data produced from the molecular dynamics simulations. Unfortunately, due to the relatively low number of sputtered particles, the simulation data are rather scattered and do not produce clear trends. For example, Fig. 5.23 shows differential sputter data calculated for sputtered products ejected 30° azimuthal from the ion's incident trajectory. The ions are at 350 eV with an incidence angle 45° from the surface normal. A sample fit using a modified Zhang curve is also shown. Figure 5.24 displays the normalized mass distribution of the sputtered particles resulting from 350 eV ions arriving from the right side impacting the center of the hemisphere. Applying a modified Zhang fit to that data using least squares fitting, a characteristic energy of 185 eV is obtained. This is compared to an E^* value of 163 eV as measured by Yalin *et al.*[110] Figure 5.25 shows the distribution from the modified Zhang fit to the calculated data and Fig. 5.26 is the distribution as calculated by Yalin *et al.* All of the data are for ions at 350 eV with a 45° incidence angle. Similar fits are applied for the 250 eV and 100 eV cases, shown in Figs. 5.27–5.30, and compared to the fits applied to the experimental data. The calculated values for the three cases are presented in Table 5.2. Generally, the calculated differential sputter data tend to result in a higher characteristic energy for the modified Zhang fits. The difference of the calculated values from the values found by Yalin *et al.*[109] increase as the ion energy becomes lower. This is due to the reduced amount of sputtering data available at the lower energies; the same number of ion impacts at higher energies produce a greater number of sputtered products, increasing the sample size available for the fits. Considering the high amount of scatter in the calculated differential data due to a relatively low number of samples, considerable error is likely present.

Ion energy [eV]	Calc. E^* [eV]	Exp. E^* [eV]	% error
100	43.4	14.3	203
250	129	86.4	49.3
350	185	163	13.5

Table 5.2: Comparison between the characteristic energy values calculated for the modified Zhang fits.

5.2.1.4 Temperature Considerations

The dependence of the sputter yields on surface temperature is also investigated. The sputtering simulations are run with the BN surface regulated to 150°C, or 423 K, as

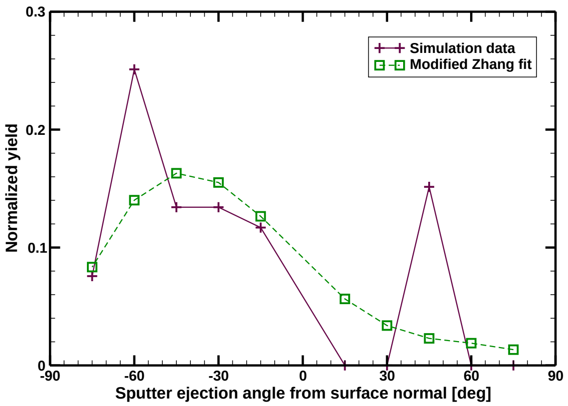

Figure 5.23: Sample differential sputter yields with an applied modified Zhang fit.

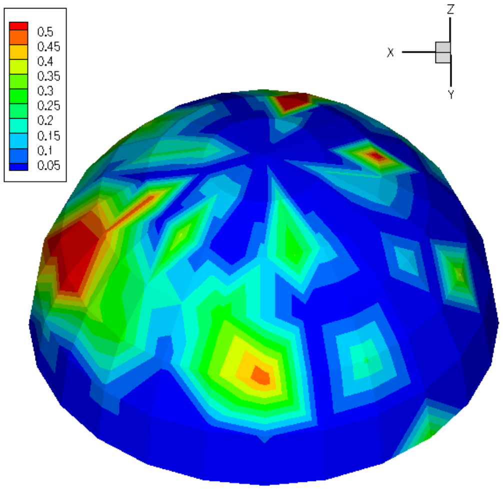

Figure 5.24: The calculated differential sputter yields for 350 eV ions at a 45° incidence.

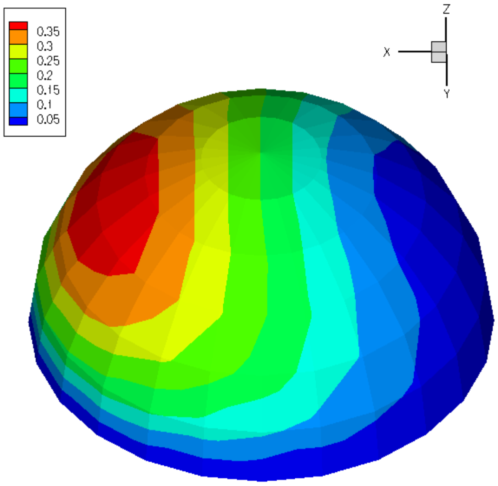

Figure 5.25: A modified Zhang differential sputter yields fit for the simulated 350 eV case.

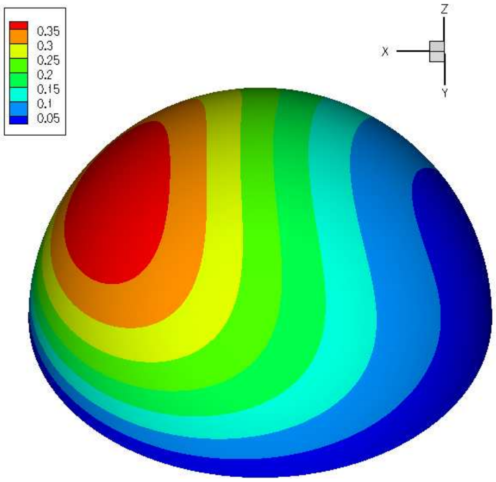

Figure 5.26: A modified Zhang differential sputter yields fit for experimental data obtained by QCM measurements for 350 eV ions.

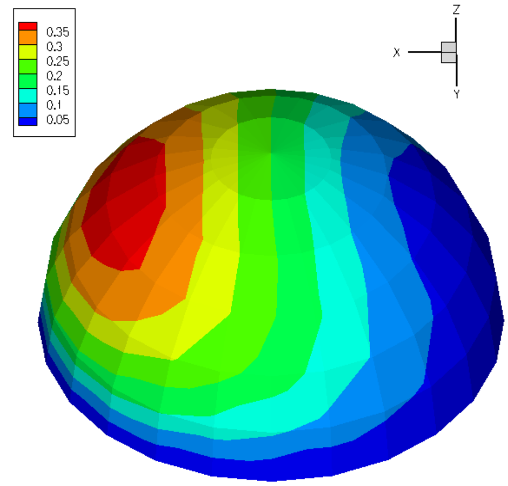

Figure 5.27: A modified Zhang differential sputter yields fit for the simulated 250 eV case.

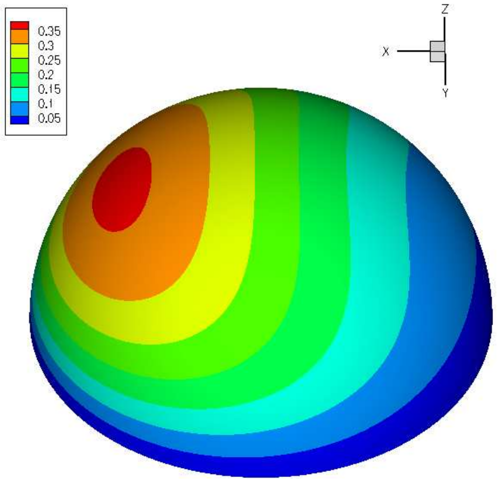

Figure 5.28: A modified Zhang differential sputter yields fit for experimental data obtained by QCM measurements for 250 eV ions.

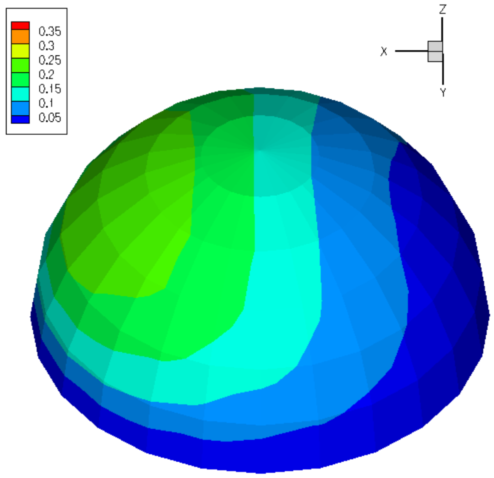

Figure 5.29: A modified Zhang differential sputter yields fit for the simulated 100 eV case.

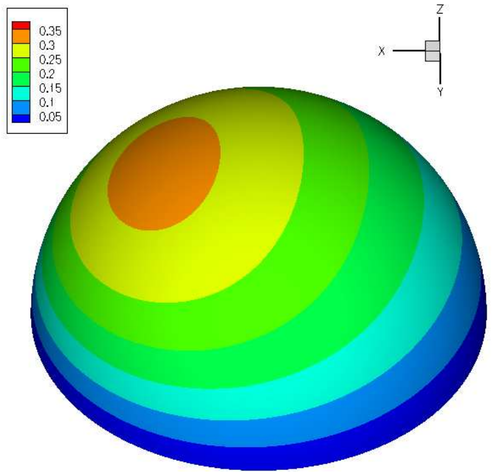

Figure 5.30: A modified Zhang differential sputter yields fit for experimental data obtained by QCM measurements for 100 eV ions.

per the experimental conditions reported by a few of the researchers.[43,95,109] However, the temperature of the channel wall surface for Hall thrusters can reach 850 K and higher.[51] So proper modeling of the wall erosion rate will require proper temperature considerations. Molecular dynamics has been used before to model temperature effects on sputtering.[114] The MD model here is used to calculate the sputter yields at temperatures of 423 K, 650 K, 850 K, and 1050 K. The simulations model 50 eV ions impacting with a 45° incidence angle. Three hundred ion impacts apiece are simulated for the 650 K, 850 K, and 1050 K cases. The results are shown in Fig. 5.31 where again the error bars indicate the standard deviation of the fluctuation in the sputter yield calculations. The change in the sputter yield is significant, as it is roughly twice the rate at 850 K than at 423 K.

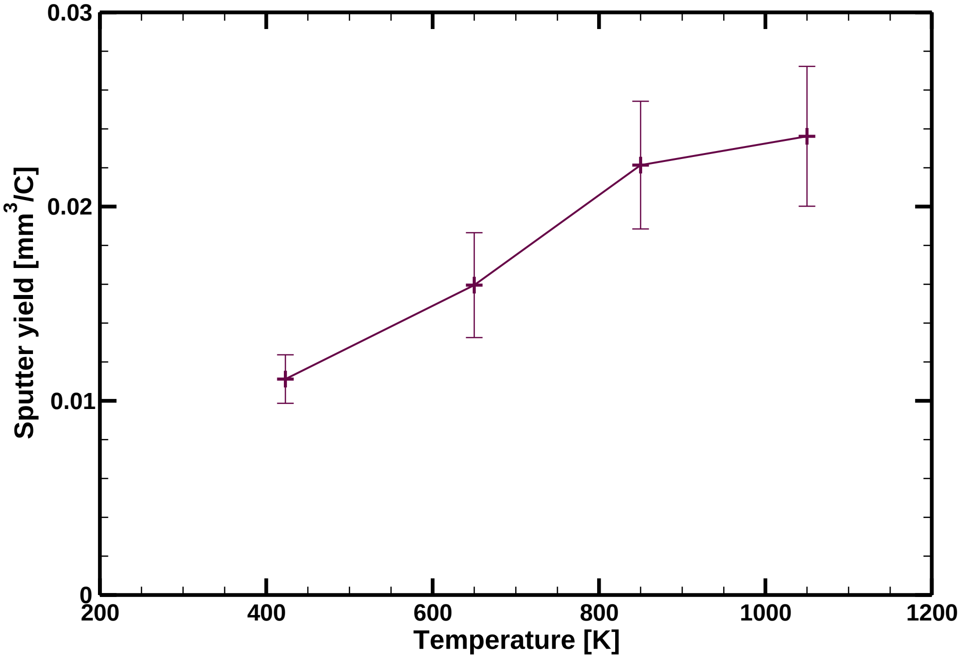

Figure 5.31: The sputter yield of BN at various surface temperatures.

5.2.1.5 Ion Flux and Fluence Considerations

The effect of the ion flux and fluence are also studied using the molecular dynamics model. The ion flux is the rate at which ions impact a specified area of the surface. Due to the limiting constraints for the timestep and the domain size in molecular dynamics

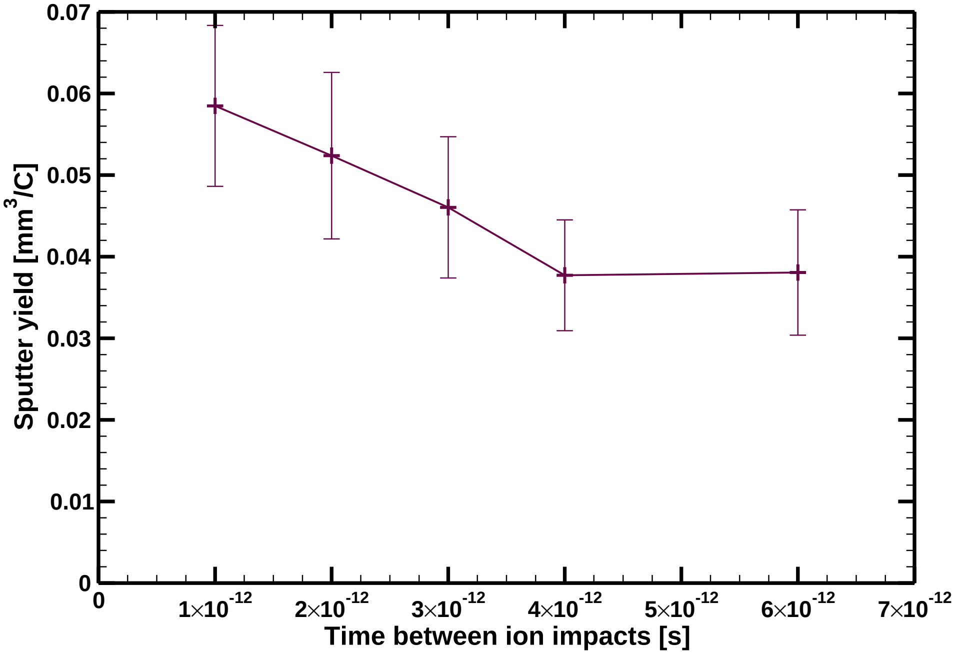

Figure 5.32: The calculated BN sputter yields as a function of the time between ion impacts.

simulations, the actual flux of the ions hitting the surface can not be directly calculated without excessive computational time requirements. Once the main dynamics of the system after the ion impact are resolved and the surface has reached an equilibrium state at the regulated temperature, the rest of the intervening time between ion impacts is composed of thermal fluctuations of the atoms in the system. There can be presumed to be little difference between states once this equilibrium state has been reached, and it would have negligible effects on the sputtering output. It has to be ensured that the system has completely relaxed after an ion impact before injecting the next ion. Sputtering simulations are conducted with varying times between ion injections and are shown in Fig. 5.32. A time interval of roughly 4 ps is sufficient to allow the system to relax before injecting the next ion.

Figure 5.33 shows the distribution of the time it takes from an ion insertion into the simulation to a sputtered particle being registered. This is a representation of the time required for particles to sputter after ion impact if the travel time for the ion to reach the surface and the time for the sputtered particles to escape the domain are

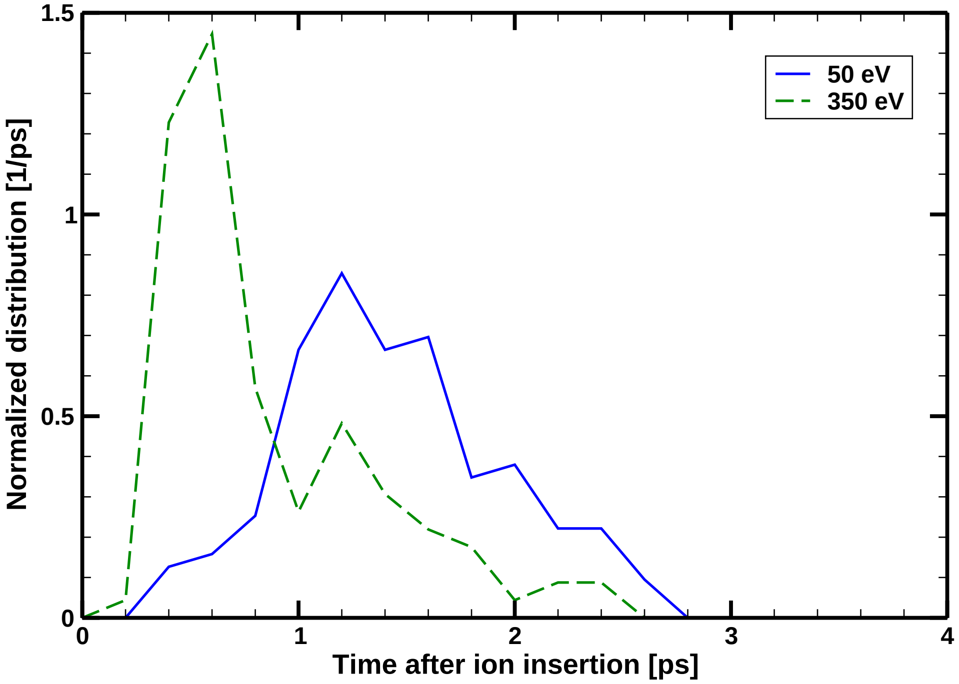

Figure 5.33: The distribution of the time between ion insertion and sputtering observation.

also accounted for. Based on the average distance of the surface from an injection point, a 50 eV xenon ion will take about 0.3 ps to reach the surface while a 350 eV ion requires about 0.1 ps. The time for particles to reach the outer boundary after being sputtered is more difficult to estimate since they are ejected with a wide range of angles and energies. A fast boron atom ejected nearly normal to the surface can require less than 0.1 ps to escape the domain while a slow nitrogen molecule with a trajectory nearly parallel to the surface can require more than 1 ps. However, it can still be noted that the majority of sputtering impacts occur within about 2 ps after ion impact. The peak of the distribution for the 50 eV ions is shifted later than that of the 350 eV ion distribution. In part this is due to the longer time for the ions to reach the surface and for sputtered particles to exit, but there is still evidence that sputtering events occur sooner with higher ion energies.

In addition to the ion flux, the ion fluence may also affect the sputter yields. Fluence is a measure of the total number of ions per unit area that have impacted a surface. Initially, as ions impact the surface and alter its morphology—as well as a number of ions becoming embedded within the surface—the resulting sputter yield can vary from that observed after a large number of ion impacts have already occurred. An extended run is performed with the molecular dynamics simulation to examine to what extent the ion fluence affects the sputter yield. Fifteen hundred ions at 50 eV and with a 45° incidence angle are impacted successively onto the same surface. The calculated average sputter yield versus the number of ion impacts is shown in Fig. 5.34. Both the cumulative average and a moving average calculated over 300 ions are shown. Only after the initial 600 ion impacts does the sputter yield result begin to stabilize. The sputter yield results presented in this work are taken from ion impacts performed from this or other suitable initial states.

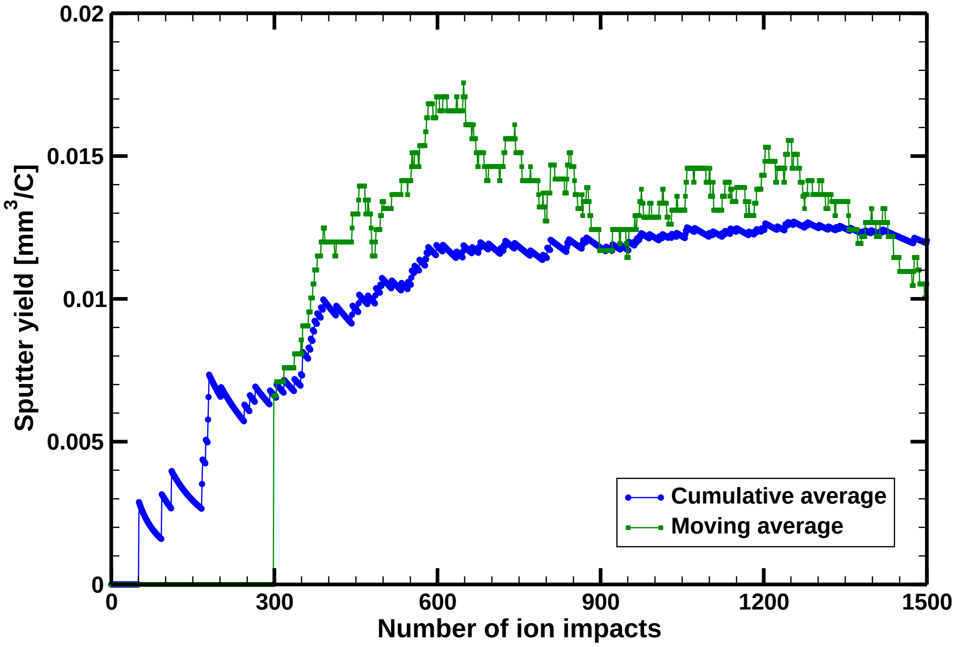

Figure 5.34: The sputter yield as calculated by cumulative and moving averages versus the number of ion impacts.

5.3 Hall Thruster Channel Wall Erosion Modeling

5.3.1 4000 Hour Life Test of the SPT-100 Thruster

The hydrodynamic plasma model and the molecular dynamics sputtering model are used in conjunction to model the erosion of the channel walls of an SPT-100 Hall thruster. The hydrodynamic model calculates the properties of the ion flux to the walls, while the molecular dynamics model is used to provide the sputter yield profiles for the wall material. The resulting erosion rates are used to update the wall profiles and the evolution of the thruster geometry is tracked over time. The lifetime of the thruster can be evaluated in this manner.

5.3.1.1 Background

The SPT-100 thruster has been extensively tested and analyzed over the years.[9,30,42] Most pertinent to the work here, a 4000 hour life test has been performed with the results publicly available.[2] The experimental test was performed in a vacuum chamber at FAKEL with a pressure of 6×10^{-5} torr during thruster operation. The experiments focused on the properties of the plume, particularly the angular distribution of the current density and the ion energy, and the effects of the plume on surfaces external to the thruster, which includes the deposition of material sputtered from the walls. The eroded wall profiles at various time intervals are presented, as are the erosion rates versus time. Unfortunately, the measurement methods, the error estimates, and other desired information directly related to the channel wall erosion are not described in the work.

The thruster nominally operates at a power of 1.35 kW, or a discharge voltage of 300 V and a discharge current of 4.5 A. Xenon is fed into the channel at a rate of 4.9 mg/s. The geometry of the thruster includes a 24.0 mm long channel with an inner radius of 34.3 mm and an outer radius of 50.0 mm. The inner wall is 10 mm thick while the outer wall has a 5 mm thickness. For the simulations, the domain is divided into square cells with sides 0.25 mm long. This results in a mesh that contains 6305 cells at the beginning-of-life (BOL) conditions. The mesh incorporates additional cells as needed as the walls erode away and increase the domain size. At the anode, a plasma number density of 3×10^{17} m^{-3}, an ion velocity of 1000 m/s, and an electron temperature of 3 eV are set similar to the conditions outlined by Keidar *et al.*[59] A coefficient of 1/100 is used for the Bohm mobility term, while a coefficient of 15.0 is applied for the wall collision frequency. These values allow for a stable solution of the hydrodynamic model, while providing reasonable values for the calculated potential drop and thrust.

The hydrodynamic model is used to simulate the flow within the channel of the SPT-100 thruster. Contour plots of the plasma density and potential fields at BOL conditions are shown in Figs. 5.35 and 5.36, respectively. The anode is on the left side of the figure, while the exit plane is at the right border. The white spaces above and below the channel in the figures represent the outer and inner wall thicknesses, respectively, in relation to the channel domain. For the erosion calculations, a Gaussian distribution of the average ion velocity components is used instead of assuming a monoenergetic beam to the walls. The velocity distributions are based on the ion temperature, which can be assumed to be the same as the initial neutral temperature, which in turn is based on a wall temperature of 850 K. The velocity distributions are used to create a distribution of ion angles and energies that factor in the calculations of the resulting erosion.

5.3.1.2 Erosion Results and Discussion

From the ion flux to the walls, the erosion rates are calculated through the sputter yields obtained from the molecular dynamics work. Results from the Bohdansky fit are similar to the Wilhelm and Zhang fits for energy dependence; the erosion results presented in this section are with the Wilhelm and Zhang fits provided in Eq. 5.1. The sputter yields are increased by a factor of two to account for the temperature difference based on the results given in Fig. 5.31, as Hall thruster walls are around 850 K.[51] The yields are further increased by another factor of two as the channel walls of the SPT-100 thruster used by Absalamov *et al.*[2] for their erosion measurements were likely made of borosil rather than pure BN. Experiments by Garnier *et al.*[43] and Kim *et al.*[62] indicate

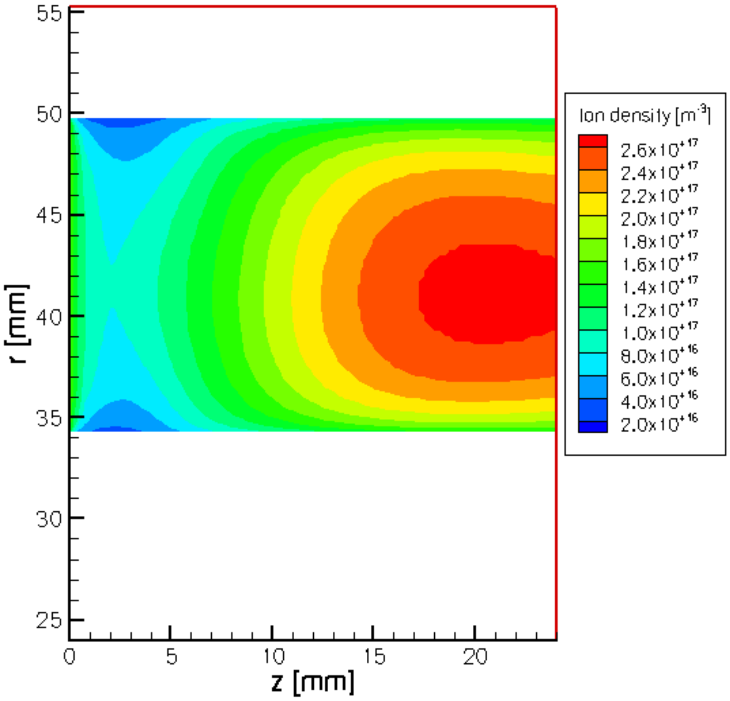

Figure 5.35: The simulated plasma density field within the SPT-100 thruster at beginning-of-life conditions.

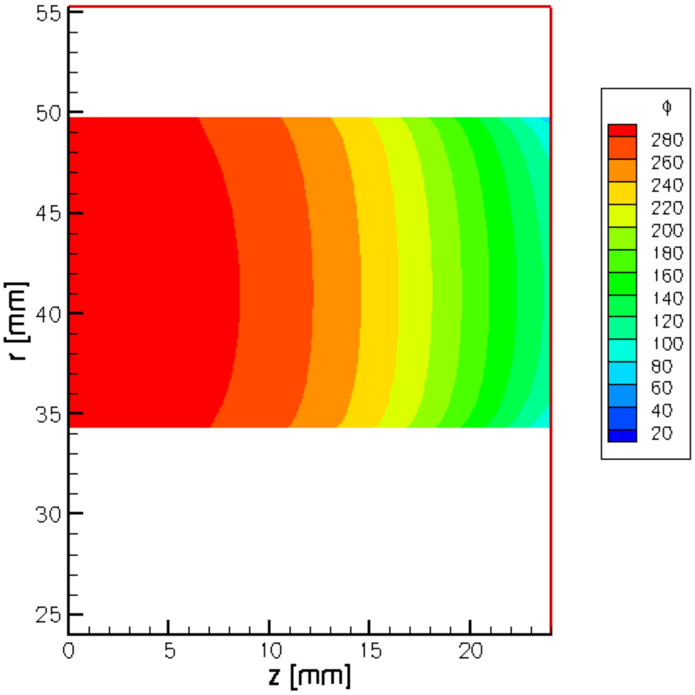

Figure 5.36: The simulated potential field for the SPT-100 thruster at beginning-of-life conditions.

that borosil sputters roughly at twice the rate as BN. The wall profiles are updated at 10 hour time step intervals. For each new set of wall profiles, the hydrodynamic model is rerun to calculate the new ion properties along the walls, which are subsequently used to update the erosion rates and then the wall profiles. Figures 5.37 and 5.38 show sample plasma density and potential fields after 1000 hours of erosion with the altered channel geometry. Calculated wall profiles are obtained after 160, 310, 600, 800, 1000, 2400, 3290, and 4000 hours of operation and compared to the experimental ones in Figs. 5.39 and 5.40 for the outer and inner walls respectively.

There are large discrepancies between the calculated erosion profiles and the experimental ones. The calculated erosion is found to occur much further upstream than actually observed. In the simulation, nearly the entire length of the channel is found to erode, whereas for the experiments, only the final 9 or 10 mm of the channel walls are eroded. The erosion rate at the exit plane is also underpredicted early on, while it is overpredicted at later hours. This transition from underprediction to overprediction occurs around 2400 hours for the outer wall and 3300 hours for the inner wall. This is represented more clearly in Fig. 5.41, where the wall thickness at the exit plane is plotted versus operation time. Two sets of experimental data are available for this measurement and there is a high degree of agreement between them. The simulation results, again, show an underprediction of the erosion for most of the tested time. This is particularly noticeable for the outer wall. The inner wall shows better comparison.

Examining the overall erosion rates of the channel also displays these trends. Figure 5.42 shows the instantaneous total volumetric erosion rate plotted against time. The total erosion rate at BOL is somewhat underpredicted, although for most of the rest of the 4000 hours, the erosion rate is overpredicted. This stems from nearly the entire length of the channel eroding and contributing to the overall erosion rate, as opposed to a shorter segment eroding as seen experimentally. The shape of the erosion rate versus time curve given by the simulation also does not decrease nearly as steeply as expected. The kink around 1600 hours is the point when the outer wall has been eroded com-

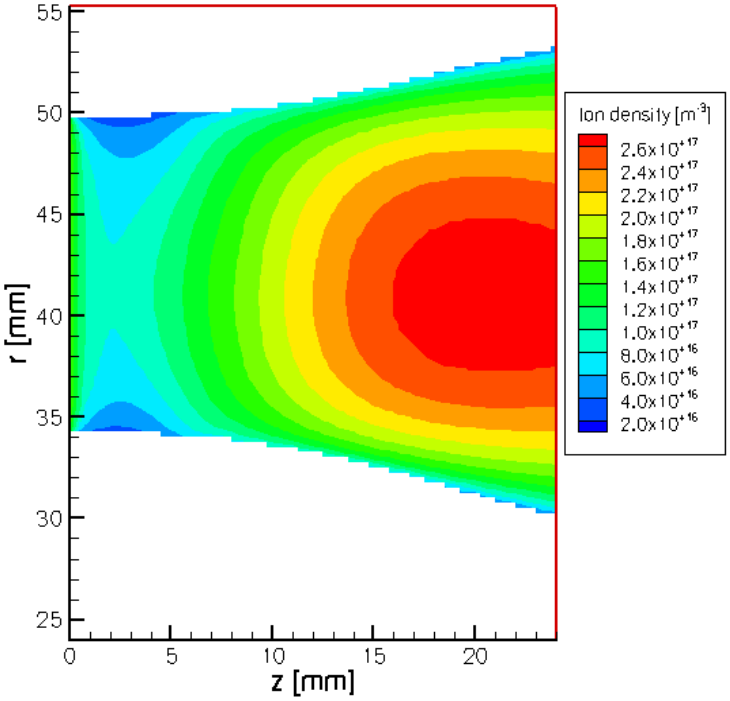

Figure 5.37: The simulated plasma density field within the SPT-100 thruster after 1000 hours.

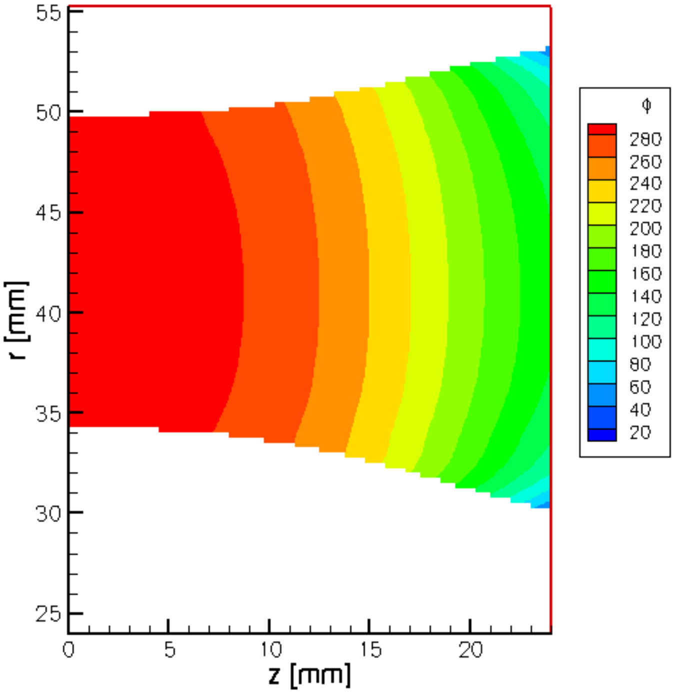

Figure 5.38: The simulated potential field for the SPT-100 thruster after 1000 hours.

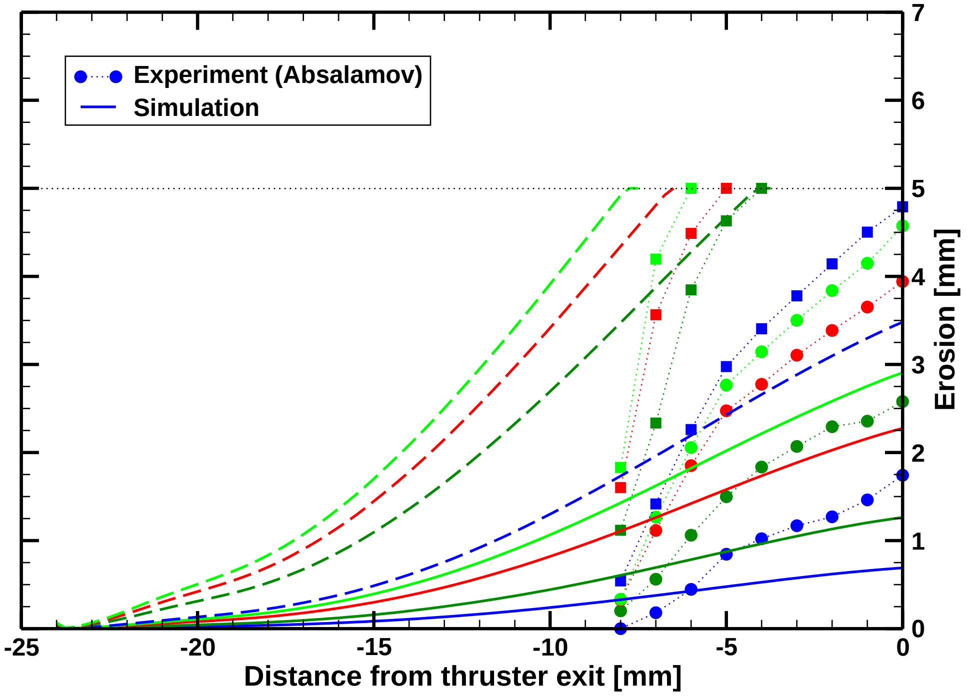

Figure 5.39: The simulated wall erosion profiles for the outer wall of the SPT-100 over 4000 hours.

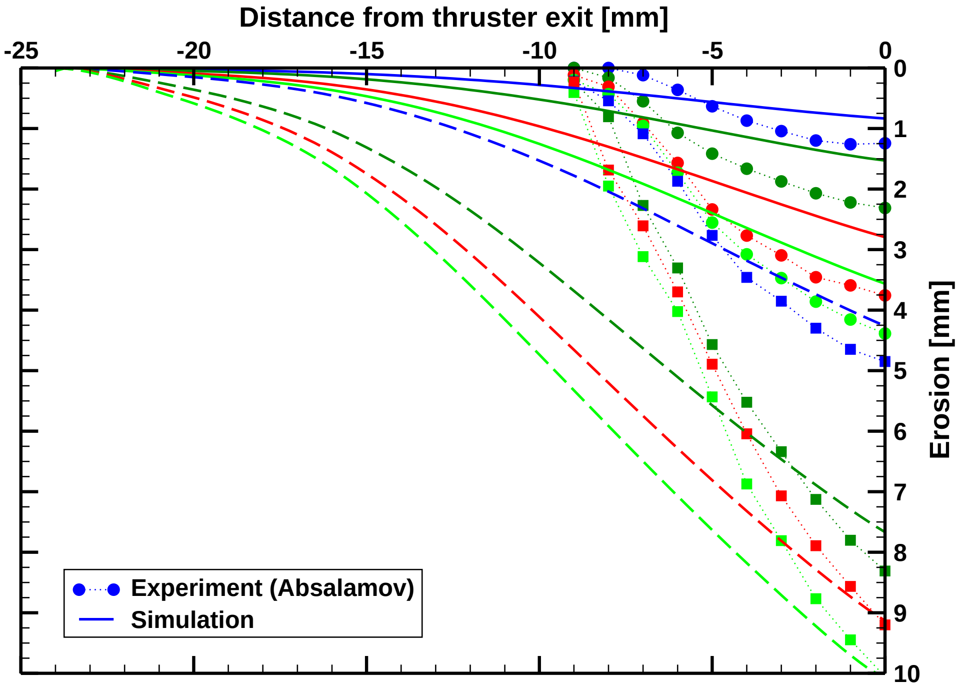

Figure 5.40: The simulated wall erosion profiles for the inner wall of the SPT-100 over 4000 hours.

pletely through at the exit plane. At that point, less channel wall material is available to contribute to the total erosion rate, and therefore the dropoff becomes a little steeper. Overall, the simulation does not capture these experimental trends very well.

In determining the reasons behind these discrepancies and the failures of the model, it is helpful to examine some previous work that was performed prior to the above results. The same hydrodynamic model is used to simulate the plasma flow in the SPT-100 thruster, however, empirical polynomial curve fits applied for the energy and angular dependence of sputter yield are used instead of the data obtained from the molecular dynamics simulations.[77] These are the same ones presented in Section 2.4.1. Figures 5.43 and 5.44 again show the calculated erosion profiles against the experimental profiles. The comparisons are much better for these results. The wall thickness at the exit plane versus time and the total erosion rate versus time are also shown with the empirical polynomial curve fit data in Figs. 5.45 and 5.46, respectively. Overall, there is a much better match to the experimental data, though some erosion is underpredicted at later times.

Though the empirical fits for the sputter yield show better results than those obtained using the sputter yields obtained from molecular dynamics, it should not be concluded that the choice of the sputter yields is incorrect. As seen in Section 2.4, the choice of the sputter yields used can play a significant role in affecting the subsequent erosion results.[116] Thus, the reason the more intensive molecular dynamics simulations are chosen to determine the sputter yields, particularly at very low energies, rather than using the quicker binary collision approximation or even semi-empirical approaches is to improve the fidelity of the sputter yields used.

The plasma model may be the main contributor towards the poor erosion results, rather than the sputter yield model. As observed with the simulation results of the NASA-173Mv1 thruster in Section 5.1, the hydrodynamic model does not readily capture sharp gradients within the plasma flow, but rather smears them out over a wider range. This is observed for the electron temperature, electric field, and plasma potential profiles

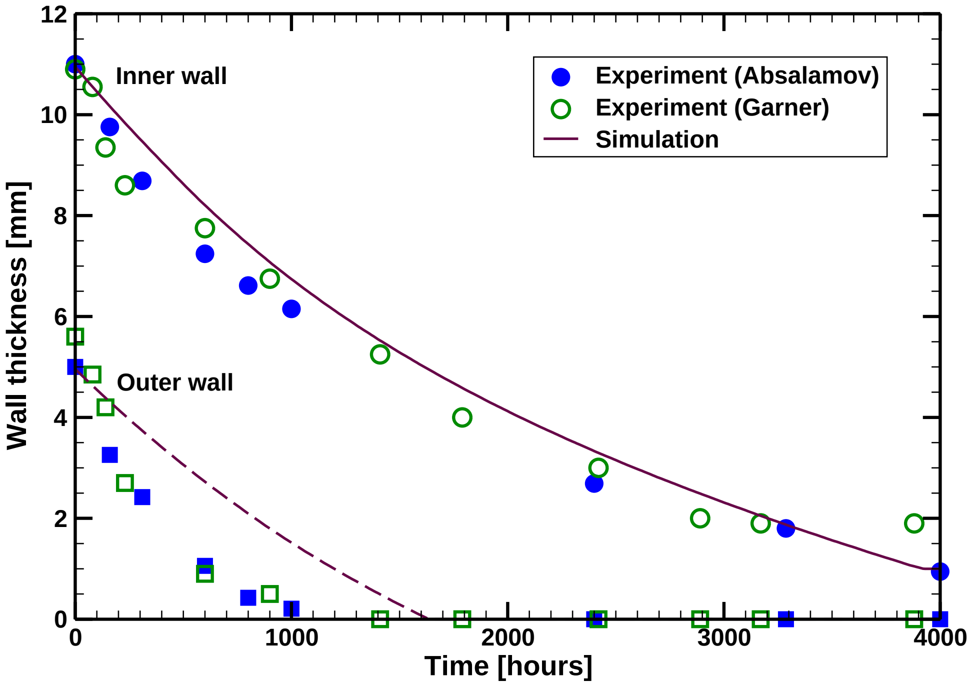

Figure 5.41: The erosion at the exit plane for the SPT-100 thruster.

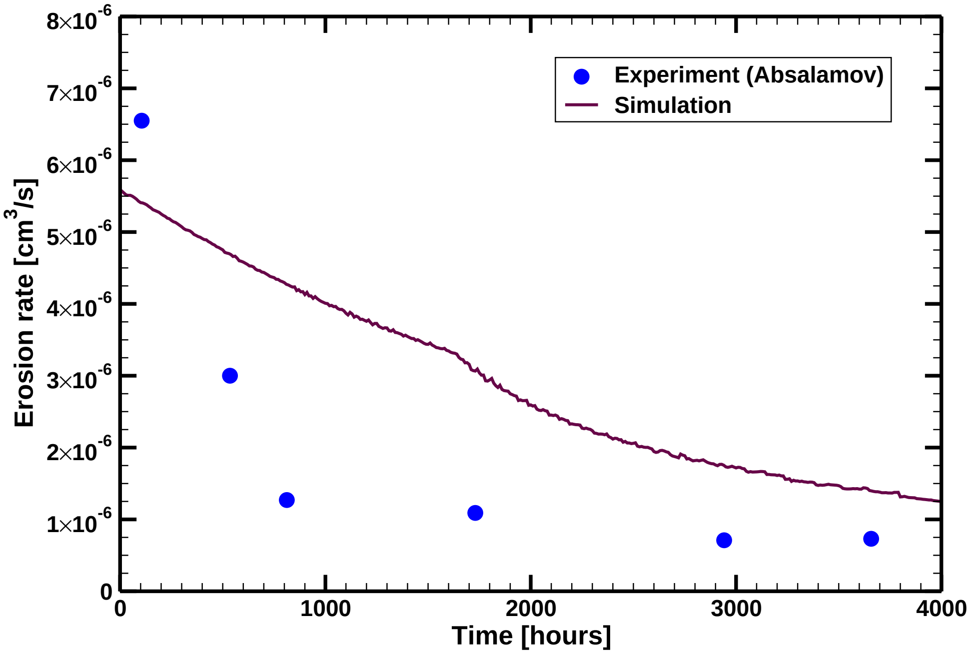

Figure 5.42: The total volumetric erosion rate for the SPT-100 thruster.

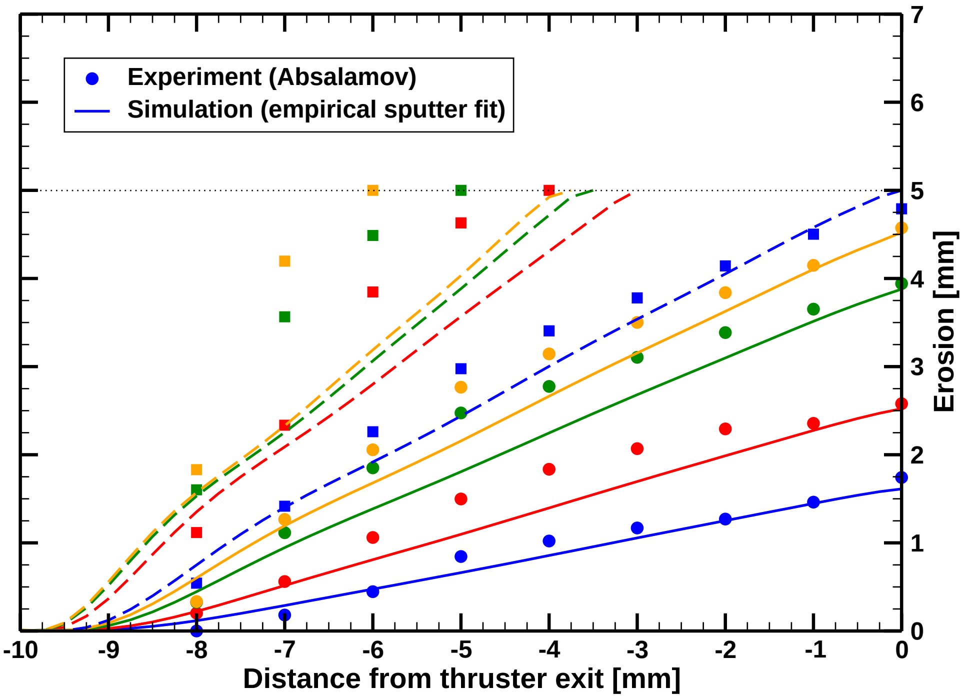

Figure 5.43: The simulated wall erosion profiles for the outer wall of the SPT-100 over 4000 hours using the empirical sputter yield fits.

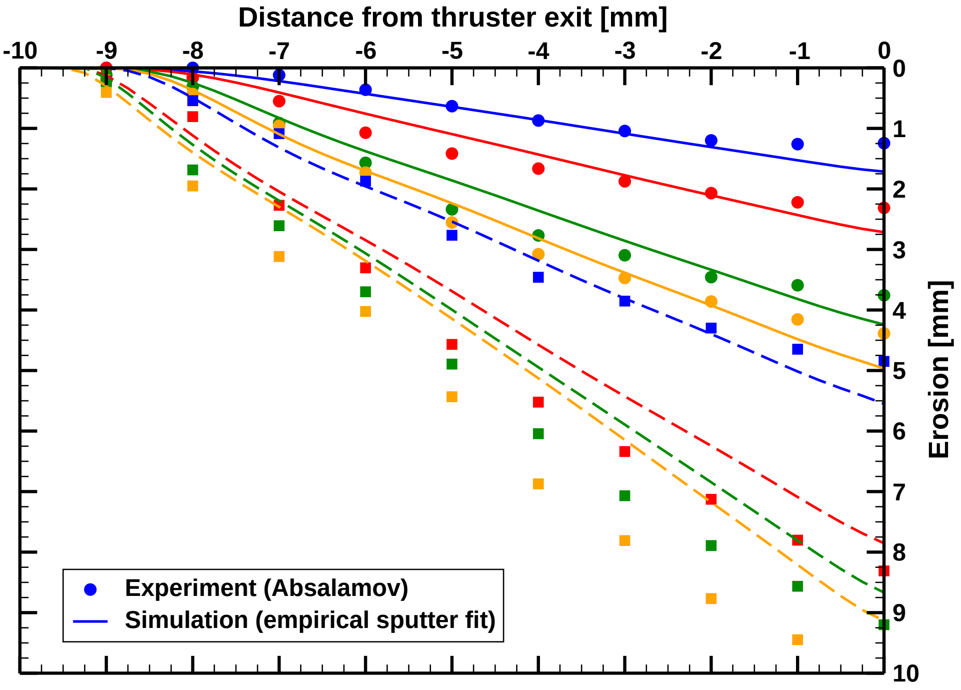

Figure 5.44: The simulated wall erosion profiles for the inner wall of the SPT-100 over 4000 hours using the empirical sputter yield fits.

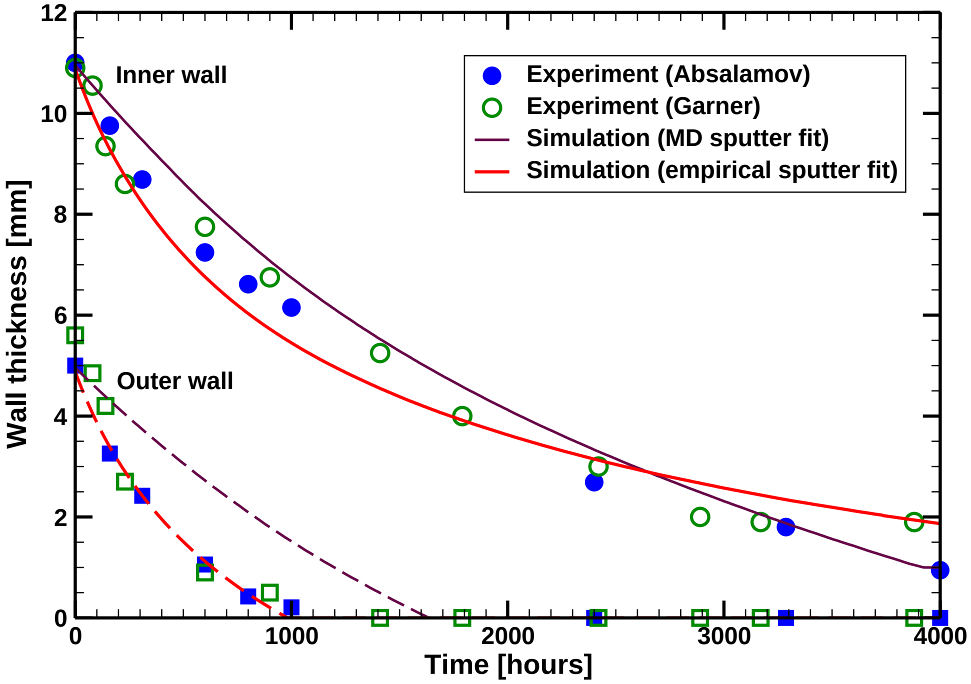

Figure 5.45: The erosion at the exit plane for the SPT-100 thruster using the empirical sputter yield fits.

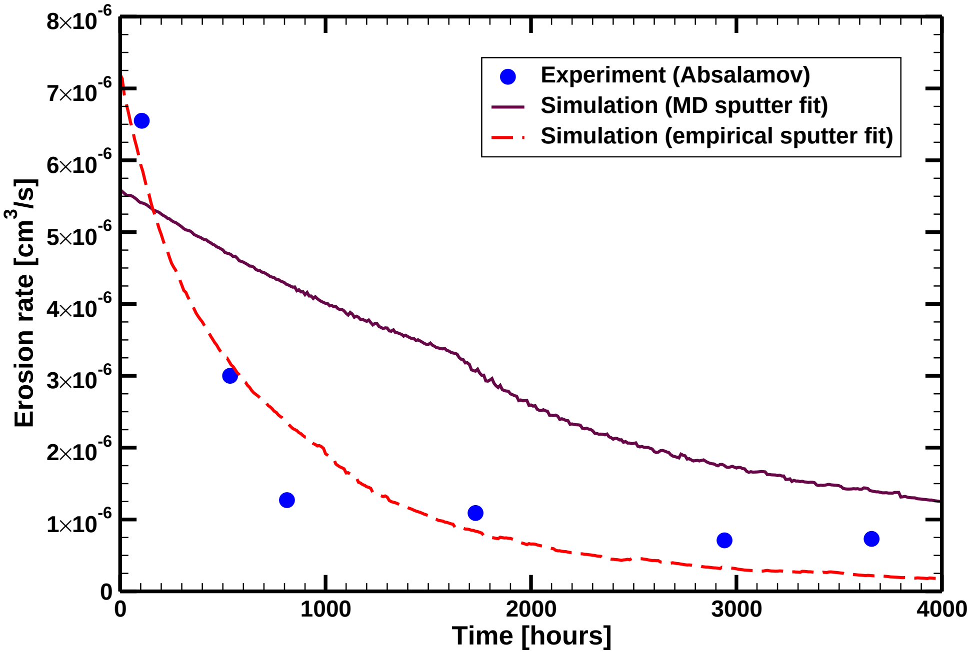

Figure 5.46: The total volumetric erosion rate for the SPT-100 thruster using the empirical sputter yield fits.

among others. For the case of the SPT-100 thruster, similar trends are occurring. The electron temperature profile along the channel is shown in Fig. 5.47. It steadily increases from the anode to the peak near the exit plane; no sharp increase indicating where the Hall current resides is observed. This produces a similar profile for the sheath potential drop. Since the ions are accelerated across the sheath to the walls, a higher sheath potential near the anode region will cause a higher erosion rate there too. Again, with the centerline potential profile, shown in Fig. 5.48, the decrease begins right from the anode region and is more gradual overall than is expected. These effects would smear the erosion over a wider domain as well, and stretch it back to the anode region. Capturing sharper gradients would push the onset location of erosion further downstream. This would also alleviate the issues seen with the total erosion rate profile over time shown in Fig. 5.46. The empirical sputter yield case presents a curve that is more logarithmic in shape than the MD sputter yield case. This shape is mostly affected by the eroded wall angle. As the wall angle increases, the divergent plasma flow of the thruster impinges less upon the walls, thus decreasing erosion for these geometries. The difference in the eroded wall angles for the simulations and experiment is evident in Figs. 5.39 and 5.40. Therefore, a model that better captures the sharp gradients of the plasma flow will push the onset location of erosion further downstream, which will increase the eroded wall angles, which in turn will further reduce erosion at later times, capturing the logarithmic dependence seen for the total erosion rate over time. The deficiencies of the plasma model are due in part to the electron transport modeling, which is presently still unable to be captured well by any state-of-the-art model.

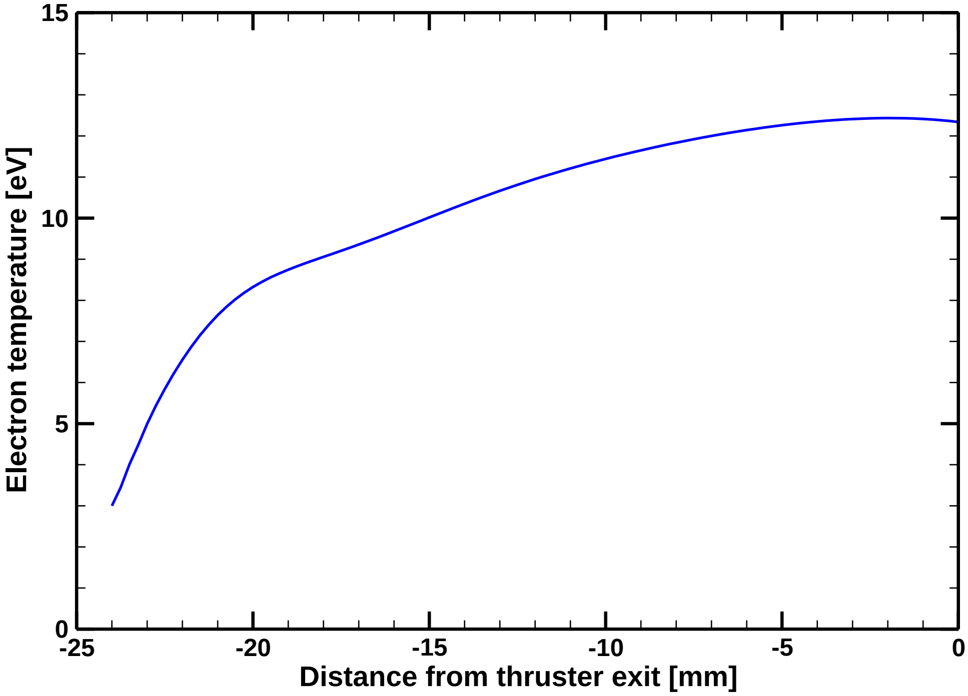

Figure 5.47: The calculated centerline electron temperature profile for the SPT-100 thruster.

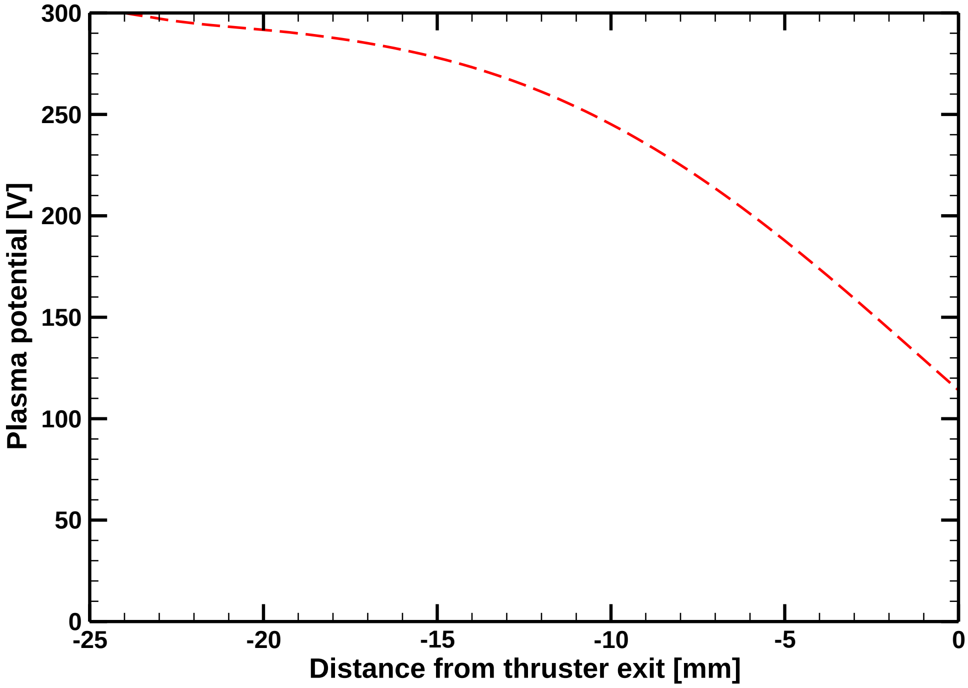

Figure 5.48: The calculated centerline plasma potential profile for the SPT-100 thruster.

CHAPTER VI

Conclusions

6.1 Summary

The development of a computational model of the erosion of the acceleration channel walls in Hall thrusters is presented in this thesis. At the beginning of this research, this work was the only Hall thruster erosion simulation work known that was not based on an empirical or semi-empirical approach, but rather focused on a plasma model combined with a sputter yield model. A hydrodynamic model is used to describe the plasma flow within a Hall thruster and a molecular dynamics model is used to calculate the sputter yields of the wall material. The hydrodynamic approach is chosen as it offers a relatively quick turnaround on results—less than a minute is required for a single run—while maintaining a physics-based foundation. This work presents the only fluid-based erosion simulation known to the author at the time of writing, though there are now several particle-based methods under development. The molecular dynamics model is chosen as it provides a method that is as close to a first-principles approach as possible while maintaining tractable solutions. This work presents the only known application of a full MD model for boron nitride sputter yield calculations and the first to present sputter yield data at energies below 80 eV.

The hydrodynamic model is used to simulate the plasma flow in two thrusters, the SPT-100 and the NASA-173Mv1 thrusters. For the SPT-100 thruster, the model is used to calculate the ion flux to the walls for erosion analysis. More will be mentioned about this work later in conjunction with the sputter yield model. For the NASA-173Mv1 thruster, the hydrodynamic model is used to compare the differences between krypton and xenon. In particular, simulations are run to analyze the specific issues that lower the performance of krypton as compared to xenon. Though the intrinsic properties of krypton such as the ionization energy and the ionization collision cross section lower the propellant utilization fraction, external factors, particularly the magnetic field configuration, also play a significant role. The magnetic field configuration affects many aspects of the plasma properties that can lower the efficiencies of the thruster. When the xenon case uses the magnetic field for krypton instead, a lower electron temperature profile reduces the ionization rate and therefore lowers the propellant utilization. The potential profile is also affected, elongating and pushing more of the acceleration region past the exit plane of the thruster, thereby increasing possible beam divergence which also would lower the overall performance. Thus, proper configuration of the magnetic field could lead towards a viable use of krypton as a propellant for Hall thrusters if the efficiency losses are minimized. Of course, many other considerations are in play when a magnetic field is being designed and optimized for a particular thruster at a particular operation setting, but the lower performance for krypton is not insurmountable due to its inherent characteristics. The hydrodynamic model is used successfully in this case to qualitatively examine the properties of the plasma flow within a thruster.

There are issues, however, with the hydrodynamic model seen in both simulation of the NASA-173Mv1 and the SPT-100 thrusters. The model has a tendency to smooth out gradients over a wider domain. Certain features that are expected in a Hall thruster are not as clearly marked or defined. These include the ionization region, where the electron Hall current is the greatest. The plasma density is expected to peak in this region, as is the electron temperature. The acceleration zone is also not sharply captured. The plasma potential profile should have a sudden drop corresponding to a high axial electric field that accelerates the ions out of the thruster over a short distance. These trends are directly observed experimentally in the case of the NASA-173Mv1 thruster where internal measurements have been taken using the HARP system. Though similar measurements have not been performed for the SPT-100 thruster, general Hall thruster theory and design lead toward similar conclusions. The hydrodynamic code does show peaks of the electron temperature and drops in the potential profile, signifying these mechanisms are still existent in the simulation. However, again, the regions are much more spread out than expected, and can even stretch all the way to the near-anode region or well past the exit plane.

This characteristic of the hydrodynamic code likely stems at least in part from the electron temperature calculations. The electron temperature plays a key role in many different aspects of the plasma and thus issues here will propagate through the simulation. The electron temperature is found from the electron energy equation given in Eq. (3.25), where it is rewritten as a balance between energy sources and sinks. Though most models involving the electron energy equation have similar forms, the particular details vary quite a bit in the different implementations.[4, 22, 59, 65, 76, 83, 84] For the form implemented here in the hydrodynamic model, the thermal conductivity term, often represented as the gradient of the thermal heat flux, is not included since it introduces a second-order derivative of the temperature into the equation, changing the mathematical nature of the formula. Inclusion of thermal conductivity into the electron energy equation would help to increase the fidelity of the electron temperature profile. The wall collision loss term is another difficult term to model accurately, not because of its mathematical nature, but because the actual physics of the near-wall region are still not well understood.

Another issue with the hydrodynamic code—and also with all other state-of-the-art Hall thruster simulation methods—is how cross-field electron mobility is handled. There is much that is not well understood with the mechanisms that transport the electrons across the predominantly radial magnetic field lines to the anode and this is a current area of active research. Standard classical electron mobility, due to collisions with the heavy particles, is insufficient to provide the necessary mobility for Hall thruster operation. There are two other additional transport mechanisms considered: Bohm mobility due to plasma turbulence and mobility due to wall collisions. However, these forms of electron mobility are complex and difficult to model accurately. Even the underlying physical processes are still not fully understood. The cross-field mobility plays an important role in determining the potential field within the thruster and consequently the electric fields as well. In particular, the mobility should be low near the exit plane where impeded axial electron motion will create a strong axial electric field in that region, narrowing the acceleration zone. The region upstream towards the anode will have a higher electron mobility, allowing for a greater electron current to complement the lower ion current in the region so as to keep the total current consistent with the discharge current. Accurate modeling of the potential and electric fields requires accurate modeling of the electron mobility.

The molecular dynamics method is used to simulate low energy xenon ion impacts on a boron nitride surface. The primary goal of this effort is to determine dependence of the BN sputter yield on ion energy. The results from the MD simulations are compared to experimental data. There is a significant amount of scatter in the experimental data, stemming perhaps from the quality and type of BN samples tested, the quality of the ion source, or a number of other possible factors. The MD results fall within the general range expected from the different sets of data. At the lowest energy set of experimental data available, around 100 eV, the MD results compare well with the data obtained with the QCM by Yalin *et al.*, but are much higher than the results obtained from weight loss by Rubin *et al.* However, the weight loss measurements are below the detection limit for that datum point.[95,109] Using the MD data, curve fits are applied to provide an expression, given in Eq. (5.1), usable for erosion studies. At the very low energies, below 50 eV, a fit based on an expression derived by Wilhelm using quantum-statistical mechanics is provided, while a semi-empirical fit based on the work by Zhang and Zhang is used for ion energies above 50 eV,

$$Y = \begin{cases} 7.62 \times 10^{-6} \left(E - 13.0\right)^2 & E < 50 \text{ eV} \\ \frac{0.205 \ln(1+1.1383(E/462.9))}{2(E/462.9+0.01321(E/462.9)^{0.21226}+0.19593(E/462.9)^{0.5})} \left(1 - \sqrt{\frac{70.8}{E}} \cos \frac{\pi}{4}\right) & E \geq 50 \text{ eV} \end{cases} \tag{6.1}$$

A single expression fit, using the Bohdansky formula, is also applied to the MD sputter results,

$$Y = 0.06 \left[1 - \left(\frac{18.26}{E}\right)^{2/3}\right] \left[1 - \frac{18.26}{E}\right]^2 \tag{6.2}$$

though this equation uses empirical means to model the very low energy sputtering as opposed to the quantum-statistical basis of the Wilhelm equation.

The molecular dynamics method does not include many parameters, such as a surface binding energy, that can be altered to adjust the results. Most of the assumptions using the MD method are present in the interatomic potential functions used. The Molière repulsive potential is a standard one used for ion bombardment interactions. The BN potential, provided by Albe *et al.*, is based on a bond-order class of potentials initially formulated by Tersoff, and is the best suited kind of potential to describe sputtering interactions as many non-equilibrium or non-structured configurations arise in addition to the standard solid lattice form. The Albe potential has been tested for many dimers and three-body boron and nitrogen compounds and shows good agreement with quantum mechanical results. Errors and issues with the MD method implemented here are more likely to stem from statistical considerations. Although several hundred ion impacts are simulated for each ion energy scenario, due to the low sputter yields, more simulations will provide a greater confidence in the quantitative results of the work. Also, only one particular initial lattice orientation is tested, where the $(10\bar{1}0)$ plane is parallel to the surface. Other crystal orientations may provide different sputter yields, though after initial ion bombardments, the upper levels of the surface become amorphous in nature and this is the region where most of the sputtering dynamics occur.

Both of the hydrodynamic and molecular dynamic methods are used for a full Hall thruster erosion simulation. A 4000 hour life test of the SPT-100 thruster is considered.

Very little is mentioned about the particulars of the experimental erosion measurements, but it is still clear that the simulation results are significantly different. The calculated erosion profiles begin much further upstream, yet underpredict erosion at the exit plane for most of the time. The total erosion rate over time is not very well predicted by the model as well. This is in comparison to previous work done with empirical sputter yields in place of the MD calculated sputter yields, which provide better matching results. However, it is expected that the main fault does not lie with the MD generated sputter yields, but rather with the hydrodynamic plasma model. As seen with the krypton work, the hydrodynamic model has a tendency to stretch gradients within the flow. Rather than seeing a sharp drop in the potential indicating the acceleration zone or a well defined peak of the electron temperature, these gradients of the flow are spread out over a wider region. In the case of the SPT-100 simulation, this causes the extent of erosion to spread almost all the way to the near anode region. Were the increase in the electron temperature and the drop in potential pushed further downstream, the onset of erosion would also move further downstream. The resulting erosion profiles would also create larger eroded wall angles, which would reduce the erosion rate quicker over time. The combined hydrodynamic and molecular dynamic model of thruster channel wall erosion still generally captures the extent of the erosion apart from the axial extent, but it is evident there is room for further improvement.

6.2 Future Work

There are several areas of the hydrodynamic model that could use additional investigation and improvement. As stated earlier, two of the main perceived shortcomings include the treatment of the electron temperature and electron mobility. In particular, the electron energy balance equation, from which the electron temperature is calculated, can be modeled with greater fidelity. Inclusion of thermal conductivity and a better understanding of the wall collision losses will help to produce a more accurate electron temperature profile. The electron mobility is an area currently under active research.

There is much to be understood about the mechanisms that transport electrons across magnetic field lines as classical mobility is insufficient by itself for Hall thruster operation. Unfortunately, experimental isolation and measurement of mobility is difficult and so far inconclusive. A clearer understanding of the mobility mechanisms and how they are best implemented into simulation models will greatly aid not only the hydrodynamic model presented here, but all other Hall thruster flow simulations. The Bohm, or anomalous, mobility due to plasma turbulence and the wall collision frequency and near-wall physics are the two areas in particular that require further research.

Though preliminary extension of the hydrodynamic model to incorporate a two-dimensional magnetic field profile is included, there still remain issues to resolve. Stability of the model is the most notable. Even when the model uses a one-dimensional approximation of the magnetic field, it is sensitive to the initial and boundary conditions. This problem is exacerbated when expanding to the two-dimensional field. This stems from the explicit nature of the solution scheme and the source terms of the governing equations. Were the source terms to be zero, the solution method should provide stable solutions as long as the CFL condition is met. However, the source terms due to ionization and electric field considerations lead towards possible instability of the computational code. For the two-dimensional magnetic field case, only a coarse mesh of the field is available for use which leads towards a poor evaluation of gradients. This eventually devolves into instability. Another issue with the provided magnetic field mesh—often the magnetic field profiles for these thrusters are proprietary and difficult to obtain—is that it did not comply with the zero divergence condition required by Maxwell's laws of electromagnetism, or in other words, it is not self-consistent, which also leads towards instability of the plasma solution. Assuming proper, fine-grained magnetic field data is provided, the model should provide more stable results, though improper boundary conditions can affect the stability still. A two-dimensional magnetic field profile ought to provide for a great improvement on wall erosion profile characteristics since properties along the channel centerline do not necessarily translate directly radial to the walls, but rather follow field lines. This is most evident with the electron temperature, which is often assumed to be constant along magnetic field lines. The electron temperature profiles along the walls will affect the erosion profiles. This can be particularly important for high curvature or asymmetric magnetic field profiles.

Another area of possible improvement includes the plasma-sheath boundary conditions. There is active debate on the exact properties at the plasma-sheath interface, though some of it stems from the definition of the plasma edge and the sheath edge which for some refer to the same point, but for others are separate and distinct. The physics in the near-wall region are also not clearly defined.[40] In addition to the ion properties entering the sheath, there is debate on the electron dynamics, particularly when secondary emission electrons are taken into consideration. With the ions impacting the walls, the electrons colliding with the walls, the secondary electrons being emitted from the walls, the electrons perhaps cascading down the walls providing extra mobility, the strong magnetic fields influencing the dynamics near the walls, there is certainly much activity and complexity in the near-wall regions. From an erosion standpoint, the near-wall region is particularly important as it directly involves the ions impacting the walls and the walls themselves.

Another possible area for further research with the hydrodynamic model includes extending the domain past the exit plane to incorporate the near-field plume. The near-field plume region includes important dynamics that may affect the calculation of the plasma flow within the channel.[21] It also allows for a better assessment of thruster properties such as the thrust and characterization of ion acceleration outside of the thruster. It may also affect how the erosion at the corners of the walls at the exit plane evolves.[117]

The incorporation of doubly and other higher charged ions will also increase the fidelity of the hydrodynamic model. Doubly-charged ions can represent a significant fraction of the ion current and will affect the calculated plasma properties that may alter the structure of the flow. Doubly-charged ions will also impact the walls with a greater energy, knocking off a greater number of sputtered particles. There will be both direct and indirect effects on the erosion rate due to multiply-charged ions.

For the molecular dynamics model, the main consideration is to generate larger sample sizes to reduce the variance of the data presented. Though trends can be extracted from the present set of data, including a greater number of simulation events will increase the precision of the data. More sputtering events will also aid in the evaluation of differential sputter yield data. Since at the lower energies the sputter yields are fairly low, very sparse data are available to calculate differential yields. Other lattice orientations of the material also need to be tested, if at least to show independence of the sputter yields from crystal orientation. Though an amorphous layer develops at the surface, the underlying regions may affect the sputter yields in an indirect manner. With these additional tests, a greater confidence can be placed in the sputter yield results.

In addition to the dependence of the sputter yield due to ion energy, the ion incidence angle also plays a major role in determining the sputter yields. Again, more tests need to be simulated to generate a more definitive angular dependence profile. Though it is assumed that the energy and angular dependence are fairly independent of each other, this may not be the case. Instead of a single energy dependence profile and a single angular profile, a full study may need to be carried out across a range of energy profiles at various angles and a range of angular profiles at various energies to see how much influence one has on the other. Angular effects may be more pronounced at higher energies or lower energies or may peak somewhere in between.

Finally for the MD sputter yield results, more simulation runs can be tested to provide a more quantitative trend on temperature dependence. More precise values of the sputter yields at various temperatures, also including testing at more temperature values, will help to better quantify the effect of temperature on the sputter yield results. Again, the temperature dependence may not be an isolated factor, but may differ with various ion energies and incidence angles.

For the total erosion model, continued validation against different thrusters at different operating conditions at different stages in life will be needed to ensure the development of robust erosion simulations. To calibrate the model to one particular thruster and operation point does not necessarily translate to other thrusters and conditions. The hydrodynamic code can also be compared to results obtained from particle-based and hybrid methods. The molecular dynamic simulation results can be compared to further experimental data or with other simulation methods such as TRIM. The models and methods set forth in this thesis, even if ever perfected, do not represent the be-all and end-all for Hall thruster erosion analysis. There will always be a need for experimental observations as well as a range of different models and simulation methods to be able to fully characterize the erosion process and to confidently predict future wall erosion. The hydrodynamic and molecular dynamics models are part of the contribution towards this effort.

APPENDIX

APPENDIX A

The Derivation of the Force Components from the Potential Functions

A.1 Basic vector differentiation

The force field is found from the negative of the gradient of the potential, $\vec{F} = -\nabla\Phi$. At a point i, the force at that location can be found by taking the derivative of the potential with respect to the position vector, $\vec{r}_i$. A helpful vector formula is

$$\frac{\partial\left(\vec{r}_i \cdot \vec{r}_j\right)}{\partial \vec{r}_k} = \vec{r}_i \delta_{jk} + \vec{r}_j \delta_{ik} \tag{A.1}$$

This leads to the differentiation of a magnitude of a vector

$$\frac{\partial r_{ij}}{\partial \vec{r}_k} = \frac{\left(\vec{r}_i - \vec{r}_j\right)\left(\delta_{ik} - \delta_{jk}\right)}{r_{ij}} \tag{A.2}$$

where i, j, and k are points, not necessarily axis directions, r_{ij} is the magnitude of the vector from j to i, and δ is the Kronecker delta. This can be reduced to the three cases where $k = i$, $k = j$, or $k \neq i, j$ the formula reduces to

$$\frac{\partial r_{ij}}{\partial \vec{r}_k} = \begin{cases} \frac{\left(\vec{r}_i - \vec{r}_j\right)}{r_{ij}}, & k = i \\ \frac{\left(\vec{r}_j - \vec{r}_i\right)}{r_{ij}}, & k = j \\ 0, & k \neq i, j \end{cases} \tag{A.3}$$

which produces a vector along the $\vec{r}_{ij}$ (or $\vec{r}_{ji}$) direction when not zero.

A.2 Derivative of the Molière potential for xenon

The Molière potential function is given in Eq. (4.13). Its derivative is straightforward following Eq. (A.2) and when taken with respect to point n is equal to

$$\vec{F}_n = -\frac{\partial \Phi}{\partial \vec{r}_n} = -\frac{Z_i Z_j e^2}{4\pi\epsilon_0 r_{ij}} \left[\left(\frac{0.105}{a_F} + \frac{0.35}{r_{ij}}\right)\exp\left(-0.3\frac{r_{ij}}{a_F}\right) + \left(\frac{0.66}{a_F} + \frac{0.55}{r_{ij}}\right)\exp\left(-1.2\frac{r_{ij}}{a_F}\right) + \left(\frac{0.60}{a_F} + \frac{0.10}{r_{ij}}\right)\exp\left(-6.0\frac{r_{ij}}{a_F}\right)\right]\left(\frac{\vec{r}_i - \vec{r}_j}{r_{ij}}\right)(\delta_{in} - \delta_{jn}) \tag{A.4}$$

A.3 Derivative of the boron nitride potential

Recall the modified Tersoff potential for boron nitride in Eqs. (4.3) to (4.9). Taking the derivative of the boron nitride potential with respect to point n then results, from the chain rule,

$$\vec{F}_n = -\frac{\partial \Phi}{\partial \vec{r}_n} = -\frac{1}{2}\sum_{i,j(i\neq j)} \left(f_c[f'_R - b_{ij}f'_A - b'_{ij}f_A] + f'_c[f_R - b_{ij}f_A]\right) \tag{A.5}$$

where

$$f'_c(r_{ij}) = \frac{\partial f_c}{\partial \vec{r}_n}\begin{cases} 0, & r \leq R - D \\ -\frac{9x}{2D(x^3-1)^2}\exp\left(\frac{3x^3}{x^3-1}\right), & R - D < r < R + D \\ 0, & r \geq R + D \end{cases} \tag{A.6}$$

$$f'_R = \frac{\partial f_R}{\partial \vec{r}_n} = -\beta\sqrt{2S}\frac{D_0}{S-1}\exp\left(-\beta\sqrt{2S}(r_{ij} - r_0)\right)\left(\frac{\vec{r}_i - \vec{r}_j}{r_{ij}}\right)(\delta_{in} - \delta_{jn}) \tag{A.7}$$

$$f'_A = \frac{\partial f_A}{\partial \vec{r}_n} = -\beta\sqrt{2S}\frac{D_0}{S-1}\exp\left(-\beta\sqrt{\frac{2}{S}}(r_{ij} - r_0)\right)\left(\frac{\vec{r}_i - \vec{r}_j}{r_{ij}}\right)(\delta_{in} - \delta_{jn}) \tag{A.8}$$

and

$$b'_{ij} = \frac{\partial b_{ij}}{\partial \vec{r}_n} = -\frac{1}{2}\gamma^n \chi_{ij}^{n-1}\left(1 + \gamma^n \chi_{ij}^n\right)^{-\frac{1}{2n}-1}\chi'_{ij} \tag{A.9}$$

$$\chi'_{ij} = \frac{\partial \chi_{ij}}{\partial \vec{r}_n} = \sum_{k\neq i,j} f'_c g h + f_c g' h + f_c g h' \tag{A.10}$$

$$h' = \frac{\partial h_{ij,ik}}{\partial \vec{r}_n} = 3\lambda_3^3(r_{ij} - r_{ik})^2\exp\left[\lambda_3^3(r_{ij} - r_{ik})^3\right]\left(\frac{\vec{r}_i - \vec{r}_j}{r_{ij}}(\delta_{in} - \delta_{jn}) - \frac{\vec{r}_i - \vec{r}_k}{r_{ik}}(\delta_{in} - \delta_{kn})\right) \tag{A.11}$$

$$g' = \frac{\partial g_{ij,ik}}{\partial \vec{r}_n} = -\frac{2c^2\left(m - \cos\left(\theta_{ijk}\right)\right)}{\left[d^2 + \left(m - \cos\left(\theta_{ijk}\right)\right)^2\right]^2}\frac{\partial \cos\left(\theta_{ijk}\right)}{\partial \vec{r}_n} \tag{A.12}$$

The cosine of the angle between the three particles can be represented as a function of the particle locations through the dot product identity

$$\vec{r}_{ij} \cdot \vec{r}_{ik} = r_{ij} r_{ik} \cos\left(\theta_{ijk}\right) \tag{A.13}$$

or

$$\cos\left(\theta_{ijk}\right) = \frac{\left(\vec{r}_j - \vec{r}_i\right) \cdot \left(\vec{r}_k - \vec{r}_i\right)}{r_{ij} r_{ik}} = \frac{\vec{r}_j \cdot \vec{r}_k - \vec{r}_j \cdot \vec{r}_i - \vec{r}_k \cdot \vec{r}_i + \vec{r}_i \cdot \vec{r}_i}{r_{ij} r_{ik}} \tag{A.14}$$

Then the derivative of the cosine becomes

$$\begin{aligned}
\frac{\partial \cos\left(\theta_{ijk}\right)}{\partial \vec{r}_n} &= \frac{\partial}{\partial \vec{r}_n} \left(\frac{\vec{r}_j \cdot \vec{r}_k - \vec{r}_j \cdot \vec{r}_i - \vec{r}_k \cdot \vec{r}_i + \vec{r}_i \cdot \vec{r}_i}{r_{ij} r_{ik}} \right) \\
&= \frac{1}{r_{ij} r_{ik}} \left[\frac{\partial (\vec{r}_j \cdot \vec{r}_k)}{\partial \vec{r}_n} - \frac{\partial (\vec{r}_i \cdot \vec{r}_j)}{\partial \vec{r}_n} - \frac{\partial (\vec{r}_i \cdot \vec{r}_k)}{\partial \vec{r}_n} + \frac{\partial (\vec{r}_i \cdot \vec{r}_i)}{\partial \vec{r}_n} \right] \\
&\quad + \left(\vec{r}_j - \vec{r}_i\right) \cdot \left(\vec{r}_k - \vec{r}_i\right) \frac{\partial}{\partial \vec{r}_n} \left(\frac{1}{r_{ij} r_{ik}} \right) \\
&= \frac{1}{r_{ij} r_{ik}} \left[\vec{r}_j \delta_{kn} + \vec{r}_k \delta_{jn} - \vec{r}_i \delta_{jn} - \vec{r}_j \delta_{in} - \vec{r}_i \delta_{kn} - \vec{r}_k \delta_{in} + 2 \vec{r}_i \delta_{in} \right] \\
&\quad - \frac{(\vec{r}_j - \vec{r}_i) \cdot (\vec{r}_k - \vec{r}_i)}{(r_{ij} r_{ik})^2} \left(r_{ij} \frac{\vec{r}_i - \vec{r}_k}{r_{ik}} \left(\delta_{in} - \delta_{kn}\right) + r_{ik} \frac{\vec{r}_i - \vec{r}_j}{r_{ij}} \left(\delta_{in} - \delta_{jn}\right) \right) \\
&= \left(\frac{\delta_{in} - \delta_{kn}}{r_{ik}} - \frac{(\vec{r}_j - \vec{r}_i) \cdot (\vec{r}_k - \vec{r}_i)}{r_{ij}^2 r_{ik}} \left(\delta_{in} - \delta_{jn}\right) \right) \left(\frac{\vec{r}_i - \vec{r}_j}{r_{ij}} \right) \\
&\quad + \left(\frac{\delta_{in} - \delta_{jn}}{r_{ij}} - \frac{(\vec{r}_j - \vec{r}_i) \cdot (\vec{r}_k - \vec{r}_i)}{r_{ij} r_{ik}^2} \left(\delta_{in} - \delta_{kn}\right) \right) \left(\frac{\vec{r}_i - \vec{r}_k}{r_{ik}} \right) \\
&= \left[\left(\frac{1}{r_{ik}} - \frac{(\vec{r}_j - \vec{r}_i) \cdot (\vec{r}_k - \vec{r}_i)}{r_{ij}^2 r_{ik}} \right) \left(\frac{\vec{r}_i - \vec{r}_j}{r_{ij}} \right) + \left(\frac{1}{r_{ij}} - \frac{(\vec{r}_j - \vec{r}_i) \cdot (\vec{r}_k - \vec{r}_i)}{r_{ij} r_{ik}^2} \right) \left(\frac{\vec{r}_i - \vec{r}_k}{r_{ik}} \right) \right] \delta_{in} \\
&\quad + \left[\frac{(\vec{r}_j - \vec{r}_i) \cdot (\vec{r}_k - \vec{r}_i)}{r_{ij}^2 r_{ik}} \left(\frac{\vec{r}_i - \vec{r}_j}{r_{ij}} \right) - \frac{1}{r_{ij}} \left(\frac{\vec{r}_i - \vec{r}_k}{r_{ik}} \right) \right] \delta_{jn} \\
&\quad + \left[\frac{(\vec{r}_j - \vec{r}_i) \cdot (\vec{r}_k - \vec{r}_i)}{r_{ij} r_{ik}^2} \left(\frac{\vec{r}_i - \vec{r}_k}{r_{ik}} \right) - \frac{1}{r_{ik}} \left(\frac{\vec{r}_i - \vec{r}_j}{r_{ij}} \right) \right] \delta_{kn}
\end{aligned} \tag{A.15}$$

Then for the above, there are two force directions (one along $\vec{r}_{ij}$ and the other along $\vec{r}_{ik}$) acting on the three particles. The six resultant forces are then (where F_{ij} is the force on particle i in the direction of $\vec{r}_{ij}$):

$$\vec{F}_{ij} = -\frac{1}{2} \sum_{i,j(i \neq j)} f_{cj} f'_R + f'_{cj} f_R - f_{cj} b_{ij} f'_A - f'_{cj} b_{ij} f_A - f_{cj} f_A \partial b_{ij} \sum_{k \neq i,j} \left(f_{ck} g'_{ij} h + f_{ck} g h'_{ij} \right) \tag{A.16}$$

$$\vec{F}_{ik} = -\frac{1}{2} \sum_{i,j(i \neq j)} -f_{cj} f_A \partial b_{ij} \sum_{k \neq i,j} \left(f'_{ck} g h + f_{ck} g'_{ik} h - f_{ck} g h'_{ik} \right) \tag{A.17}$$

$$\vec{F}_{ji} = -\frac{1}{2} \sum_{i,j(i \neq j)} -f_{cj} f'_R - f'_{cj} f_R + f_{cj} b_{ij} f'_A + f'_{cj} b_{ij} f_A + f_{cj} f_A \partial b_{ij} \sum_{k \neq i,j} \left(f_{ck} g'_{ji} h + f_{ck} g h'_{ji} \right) \tag{A.18}$$

$$\vec{F}_{jk} = -\frac{1}{2} \sum_{i,j(i \neq j)} f_{cj} f_A \partial b_{ij} \sum_{k \neq i,j} f_{ck} g'_{jk} h \tag{A.19}$$

$$\vec{F}_{ki} = -\frac{1}{2} \sum_{i,j(i \neq j)} f_{cj} f_A \partial b_{ij} \sum_{k \neq i,j} \left(f'_{ck} g h + f_{ck} g'_{ki} h - f_{ck} g h'_{ki} \right) \tag{A.20}$$

$$\vec{F}_{kj} = -\frac{1}{2} \sum_{i,j(i \neq j)} f_{cj} f_A \partial b_{ij} \sum_{k \neq i,j} f_{ck} g'_{kj} h \tag{A.21}$$

where

$$\partial b_{ij} = -\frac{1}{2} \gamma^n \chi_{ij}^{n-1} \left(1 + \gamma^n \chi_{ij}^n \right)^{-\frac{1}{2n} - 1} \tag{A.22}$$

BIBLIOGRAPHY

BIBLIOGRAPHY

[1] Abgaryan, V. et al., "Calculation Analysis of the Erosion of the Discharge Chamber Walls and Their Contamination During Prolonged SPT Operation," *30th AIAA/SAE/ASME/ASEE Joint Propulsion Conference and Exhibit*, July 1994, AIAA 94-2859.

[2] Absalamov, S. K. et al., "Measurement of Plasma Parameters in the Stationary Plasma Thruster (SPT-100) Plume and Its Effect on Spacecraft Components," *28th AIAA/SAE/ASME/ASEE Joint Propulsion Conference and Exhibit*, July 1992, AIAA 92-3156.

[3] Ahedo, E., Antón, A., Garmendia, I., Caro, I., and del Amo, J. G., "Simulation of Wall Erosion in Hall Thrusters," *30th International Electric Propulsion Conference*, Sept. 2007, IEPC-2007-067.

[4] Ahedo, E., Gallardo, J. M., and Martínez-Sánchez, M., "Model of the Plasma Discharge in a Hall Thruster with Heat Conduction," *Physics of Plasmas*, Vol. 9, No. 9, Sept. 2002, pp. 4061–4070.

[5] Ahedo, E., Gallardo, J. M., and Martínez-Sánchez, M., "Effects of the Radial Plasma-Wall Interaction on the Hall Thruster Discharge," *Physics of Plasmas*, Vol. 10, No. 8, Aug. 2003, pp. 3397–3409.

[6] Ahedo, E., Martínez, P., and Martínez-Sánchez, M., "Steady and Linearly-Unsteady Analysis of a Hall Thruster with an Internal Sonic Point," *36th AIAA/SAE/ASME/ASEE Joint Propulsion Conference and Exhibit*, July 2000, AIAA 2000-3655.

[7] Albe, K. and Möller, W., "Modelling of Boron Nitride: Atomic Scale Simulations on Thin Film Growth," *Computational Materials Science*, Vol. 10, 1998, pp. 111–115.

[8] Albe, K., Möller, W., and Heinig, K.-H., "Computer Simulation and Boron Nitride," *Radiation Effects and Defects in Solids*, Vol. 141, 1997, pp. 85–97.

[9] Arhipov, B. A. et al., "The Results of 7000-hour SPT-100 Life Testing," *24th International Electric Propulsion Conference*, 1995, IEPC 95-39.

[10] Baranov, V., Nazarenko, Y., and Petrosov, V., "The Wear of the Channel Walls in Hall Thrusters," *27th International Electric Propulsion Conference*, 2001, IEPC 01-48.

[11] Baranov, V. I., Vasin, A. I., Kalyaev, A. A., and Petrosov, V. A., "Prediction of Electric Thruster Lifetime," *23rd International Electric Propulsion Conference*, 1993, IEPC 93-099.

[12] Barnes, J. and Hut, P., "A Hierarchical O(N log N) Force-Calculation Algorithm," *Nature*, Vol. 324, No. 6096, 1986, pp. 446–449.

[13] Barral, S., Makowski, K., Peradzynski, Z., Gascon, N., and Dudeck, M., "Wall Material Effects in Stationary Plasma Thrusters. II. Near-Wall and In-Wall Conductivity," *Physics of Plasmas*, Vol. 10, No. 10, Oct. 2003, pp. 4137–4152.

[14] Berendsen, H. J. C., Postma, J. P. M., van Gunsteren, W. F., DiNola, A., and Haak, J. R., "Molecular Dynamics with Coupling to an External Bath," *Journal of Chemical Physics*, Vol. 81, No. 8, Oct. 1984, pp. 3684–3690.

[15] Betz, G. and Wehner, G. K., "Sputtering of Multicomponent Materials," *Sputtering by Particle Bombardment II (Topics in Applied Physics)*, edited by R. Behrisch, Vol. 52, Springer-Verlag, Berlin, 1983, pp. 11–90.

[16] Biersack, J. P. and Eckstein, W., "Sputtering Sutdies with the Monte Carlo Program TRIM.SP," *Applied Physics A*, Vol. 34, 1984, pp. 73–94.

[17] Boeuf, J. P. and Garrigues, L., "Low Frequency Oscillations in a Stationary Plasma Thruster," *Journal of Applied Physics*, Vol. 84, No. 7, Oct. 1998, pp. 3541–3554.

[18] Bohdansky, J., "A Universal Relation for the Sputtering Yield of Monatomic Solids at Normal Ion Incidence," *Nuclear Instruments and Methods in Physics Research B2*, 1984, pp. 587–591.

[19] Boyd, I. D. and Dressler, R. A., "Far-Field Modeling of the Plasma Plume of a Hall Thruster," *Journal of Applied Physics*, Vol. 92, Aug. 2002, pp. 1764–1774.

[20] Boyd, I. D. and Falk, M. L., "A Review of Spacecraft Material Sputtering by Hall Thruster Plumes," *37th AIAA/SAE/ASME/ASEE Joint Propulsion Conference and Exhibit*, July 2001, AIAA 2001-3353.

[21] Boyd, I. D. and Yim, J. T., "Modeling of the Near Field Plume of a Hall Thruster," *Journal of Applied Physics*, Vol. 95, No. 9, May 2004, pp. 4575–4584.

[22] Braginskii, S., "Transport Processes in Plasma," *Review of Plasma Physics*, edited by M. Leontovich, Vol. 1, Consultants Bureau, New York, 1965, pp. 201–311.

[23] Brenner, D. W., "Empirical Potential for Hydrocarbons for Use in Simulating the Chemical Vapor Deposition of Diamond Films," *Physical Review B*, Vol. 42, No. 15, Nov. 1990, pp. 9458–9471.

[24] Britton, M., Waters, D., Messer, R., Sechkar, E., and Banks, B., "Sputtering Erosion Measurement on Boron Nitride as a Hall Thruster Material," Tech. rep., NASA, 2002, NASA TM-2002-211837.

[25] Chen, M., Rohrbach, G., Neuffer, A., Barth, K.-L., and Lunk, A., “Simulation of Boron Nitride Sputtering Process and Its Comparison with Experimental Data,” *IEEE Transactions on Plasma Science*, Vol. 26, No. 6, Dec. 1998, pp. 1713–1717.

[26] Cheng, S. Y. and Martinez-Sanchez, M., “Modeling of Hall Thruster Lifetime and Erosion Mechanisms,” *30th International Electric Propulsion Conference*, Sept. 2007, IEPC-2007-250.

[27] Chesta, E. et al., “Flexible Variable-Specific-Impulse Electric Propulsion Systems for Planetary Missions,” *Acta Astronautica*, Vol. 59, 2006, pp. 931–945.

[28] Choueiri, E. Y., “Fundamental Difference Between the Two Hall Thruster Variants,” *Physics of Plasmas*, Vol. 8, No. 11, 2001, pp. 5025–5033.

[29] Clauss, C., Day, M., Kim, V., Kondakov, Y., and Randolph, T., “Preliminary Study of Possibility to Ensure Large Enough Lifetime of SPT Operating Under Increased Powers,” *33rd AIAA/SAE/ASME/ASEE Joint Propulsion Conference and Exhibit*, July 1997, AIAA 97-2789.

[30] Day, M., Maslennikov, N., Randolph, T., and Rogers, W., “SPT-100 Subsystem Qualification Status,” *32nd AIAA/SAE/ASME/ASEE Joint Propulsion Conference and Exhibit*, July 1996, AIAA 96-2713.

[31] de Heer, F. J., Jansen, R. H. J., and van der Kaay, W., “Total Cross Sections for Electron Scattering by Ne, Ar, Kr, and Xe,” *Journal of Physics B*, Vol. 12, No. 6, 1979, pp. 979–1002.

[32] De Zeeuw, D. and Powell, K. G., “An Adaptively Refined Cartesian Mesh Solver for the Euler Equations,” *Journal of Computational Physics*, Vol. 104, No. 1, 1993, pp. 56–68.

[33] Dunaevsky, A., Raitses, Y., and Fisch, N. J., “Secondary Electron Emission from Dielectric Materials of a Hall Thruster with Segmented Electrodes,” *Physics of Plasmas*, Vol. 10, No. 6, June 2003, pp. 2574–2577.

[34] Eckstein, W. and Biersack, J. P., “Computer Simulation of Two-Component Target Sputtering,” *Applied Physics A*, Vol. 37, 1985, pp. 95–108.

[35] Elovikov, S. S., Khrustachev, I. K., Mosunov, A. S., and Yurasova, V. E., “Mass Dependence of Nitride Sputtering,” *Radiation Effects and Defects in Solids*, Vol. 158, 2003, pp. 573–582.

[36] Eltekov, V. A., Elovikov, S. S., Colligon, J. S., Negrebetskaya, N. N., Promokhov, A. A., and Yurasova, V. E., “Sputtering of Graphite-Like BN Crystals,” *Radiation Effects and Defects in Solids*, Vol. 133, 1995, pp. 107–120.

[37] Emhoff, J. W., *Simulation of Ion Optics Using Particle-In-Cell and Treecode Methods*, Ph.D. thesis, University of Michigan, 2005.

[38] Fife, J. M., *Hybric-PIC Modeling and Electrostatic Probe Survey of Hall Thrusters*, Ph.D. thesis, Massachusetts Institute of Technology, 1998.

[39] Franke, E., Neumann, H., Zeuner, M., Frank, W., and Bigl, F., "Particle Energy and Angle Distributions in Ion Beam Sputtering," *Surface and Coatings Technology*, Vol. 97, 1997, pp. 90–96.

[40] Franklin, R. N., "Where is the 'sheath edge'?" *Journal of Physics D: Applied Physics*, Vol. 37, April 2004, pp. 1342–1345.

[41] Gamero-Castaño, M. and Katz, I., "Estimation of Hall Thruster Erosion Using HPHall," *29th International Electric Propulsion Conference*, Oct. 2005, IEPC-2005-303.

[42] Garner, C. E., Brophy, J. R., Polk, J. E., and Pless, L. C., "Cyclic Endurance Test of a SPT-100 Stationary Plasma Thruster," *30th AIAA/SAE/ASME/ASEE Joint Propulsion Conference and Exhibit*, July 1994, AIAA 94-2856.

[43] Garnier, Y., Viel, V., Roussel, J.-F., and Bernard, J., "Low-Energy Xenon Ion Sputtering of Ceramics Investigated for Stationary Plasma Thrusters," *Journal of Vacuum Science and Technology A*, Vol. 17, No. 6, Nov/Dec 1999, pp. 3246–3254.

[44] Garrigues, L., Hagelaar, G. J. M., Bareilles, J., Boniface, C., and Boeuf, J. P., "Model Study of the Influence of the Magnetic Field Configuration on the Performance and Lifetime of a Hall Thruster," *Physics of Plasmas*, Vol. 10, No. 12, Dec. 2003, pp. 4886–4892.

[45] Godyak, V. A., "Modified Bohm Criterion for a Collisional Plasma," *Physics Letters*, Vol. 89, No. 2, April 1982, pp. 80–81.

[46] Godyak, V. A. and Sternberg, N., "Smooth Plasma-Sheath Transition in a Hydrodynamic Model," *IEEE Transactions on Plasma Science*, Vol. 18, No. 1, Feb. 1990, pp. 159–168.

[47] Greengard, L. and Rokhlin, V., "A Fast Algorithm for Particle Simulations," *Journal of Computational Physics*, Vol. 73, No. 2, 1987, pp. 325–348.

[48] Haas, J. M., Gallimore, A. D., McFall, K., and Spanjers, G., "Development of a High-Speed, Reciprocating Electrostatic Probe System for Hall Thruster Interrogation," *Review of Scientific Instruments*, Vol. 71, 2000, pp. 4131–4138.

[49] Hagelaar, G. J. M., Bareilles, J., Garrigues, L., and Boeuf, J.-P., "Two-Dimensional Model of a Stationary Plasma Thruster," *Journal of Applied Physics*, Vol. 91, No. 9, May 2002, pp. 5592–5598.

[50] Hobbs, G. D. and Wesson, J. A., "Heat Flow Through a Langmuir Sheath in the Presence of Electron Emission," *Plasma Physics*, Vol. 9, 1967, pp. 85–87.

[51] Hofer, R. R., Katz, I., Mikellides, I. G., and Gamero-Castaño, M., "Heavy Particle Velocity and Electron Mobility Modeling in Hybrid-PIC Hall Thruster Simulations," *42nd AIAA/SAE/ASME/ASEE Joint Propulsion Conference and Exhibit*, July 2006, AIAA-2006-4658.

[52] Hofer, R. R., Mikellides, I. G., Katz, I., and Goebel, D. M., "BPT-4000 Hall Thruster Discharge Chamber Erosion Model Comparison with Qualification Life Test Data," *30th International Electric Propulsion Conference*, Sept. 2007, IEPC-2007-267.

[53] Jacobson, D. T. and Manzella, D. H., "50 kW Class Krypton Hall Thruster Performance," *39th AIAA/SAE/ASME/ASEE Joint Propulsion Conference and Exhibit*, July 2003, AIAA 2003-4550.

[54] Jahn, R. G., *Physics of Electric Propulsion*, McGraw-Hill, 1968.

[55] Jain, A., Etemadi, B., and Karim, K. R., "Total (Elastic Plus Inelastic) Cross Sections for Electron Scattering with Argon and Krypton Atoms at Energies 10-6000 eV," *Physica Scripta*, Vol. 41, 1990, pp. 321–328.

[56] Kalyaev, A., Baranov, V., and Petrosov, V., "Stationary Plasma Hall Thruster Lifetime Prediction," *24th International Electric Propulsion Conference*, 1995, IEPC 95-57.

[57] Kalyanasundaram, N., Moore, M. C., Freund, J. B., and Johnson, H. T., "Stress Evolution Due to Medium-Energy Ion Bombardment of Silicon," *Acta Materialia*, Vol. 54, 2006, pp. 483–491.

[58] Keidar, M. and Beilis, I. I., "Electron Transport Phenomena in Plasma Devices With E×B Drift," *IEEE Transaction on Plasma Science*, Vol. 34, No. 3, 2006, pp. 804–814.

[59] Keidar, M., Boyd, I. D., and Beilis, I. I., "Plasma Flow and Plasma-Wall Transition in Hall Thruster Channel," *Physics of Plasmas*, Vol. 8, No. 12, Dec. 2001, pp. 5315–5322.

[60] Keidar, M., Gallimore, A. D., Raitses, Y., and Boyd, I. D., "On the Potential Distribution in Hall Thrusters," *Applied Physics Letters*, Vol. 85, No. 13, Sept. 2004, pp. 2481–2483.

[61] Kieckhafer, A. and King, L. B., "Energetics of Propellant Options for High-Power Hall Thrusters," *Journal of Propulsion and Power*, Vol. 23, No. 1, 2007, pp. 21–26.

[62] Kim, V., Kozlov, V., Semenov, A., and Shkarban, I., "Investigation of the Boron Nitride Based Ceramics Sputtering Yield Under Its Bombardment by Xe and Kr Ions," *27th International Electric Propulsion Conference*, 2001, IEPC 01-073.

[63] Koo, J. W., *Hybrid PIC-MCC Computational Modeling of Hall Thrusters*, Ph.D. thesis, University of Michigan, 2005.

[64] Kress, J. D., Hanson, D. E., Voter, A. F., Liu, C. L., Liu, X.-Y., and Coronell, D. G., "Molecular Dynamics Simulation of Cu and Ar Ion Sputtering of Cu (111) surfaces," *Journal of Vacuum Science and Technology A*, Vol. 17, No. 5, 1999, pp. 2819–2825.

[65] Kroesen, G. M. W., Schram, D. C., Timmermans, C. J., and de Haas, J. C. M., "The Energy Balance of a Plasma in Partial Local Thermodynamic Equilibrium," *IEEE Transactions on Plasma Science*, Vol. 18, No. 6, Dec. 1990, pp. 985–990.

[66] Kubota, N. A., Economou, D. J., and Plimpton, S. J., "Molecular Dynamics Simulations of Low-Energy (25-200eV) Argon Ion Interactions with Silicon Surfaces: Sputter Yields and Product Formation Pathways," *Journal of Applied Physics*, Vol. 83, No. 8, 1998, pp. 4055–4063.

[67] Lazurenko, A., Vial, V., Bouchoule, A., Skrylnikov, A., Kozlov, V., and Kim, V., "Dual-Mode Operation of Stationary Plasma Thrusters," *Journal of Propulsion and Power*, Vol. 22, No. 1, 2006, pp. 38–47.

[68] LeVeque, R. J., "Wave Propagation Algorithms for Hyperbolic Systems," *Journal of Computational Physics*, Vol. 131, No. 2, 1997, pp. 327–353.

[69] Lieberman, M. A. and Lichtenberg, A. J., *Principles of Plasma Discharges and Materials Processing*, John Wiley & Sons, Inc., 2005.

[70] Linnell, J. A., *An Evaluation of Krypton Propellant in Hall Thrusters*, Ph.D. thesis, University of Michigan, 2007.

[71] Linnell, J. A. and Gallimore, A. D., "Internal plasma potential measurements of a Hall thruster using xenon and krypton propellant," *Physics of Plasmas*, Vol. 13, 2006, pp. 093502.

[72] Linnell, J. A. and Gallimore, A. D., "Krypton Performance Optimization in High-Voltage Hall Thrusters," *Journal of Propulsion and Power*, Vol. 22, No. 4, 2006, pp. 921–925.

[73] Lipp, A., Schwetz, K. A., and Hunold, K., "Hexagonal Boron Nitride: Fabrication, Properties and Applications," *Journal of the European Ceramic Society*, Vol. 5, 1989, pp. 3–9.

[74] Los, J. H. and Fasolino, A., "Intrinsic Long-Range Bond-Order Potential for Carbon: Performance in Monte Carlo Simulations of Graphitization," *Physical Review B*, Vol. 68, 2003, pp. 024107.

[75] Lovtsov, A., Shagayda, A., and Gorshkov, O., "Semi-Empirical Method of Hall Thrusters Lifetime Prediction," *42nd AIAA/ASME/SAE/ASEE Joint Propulsion Conference and Exhibit*, July 2006, AIAA-2006-4661.

[76] Makowski, K., Peradzynski, Z., Gascon, N., and Dudeck, M., "A Stationary Model for Stationary Plasma Thruster (SPT) Discharge," *35th AIAA/SAE/ASME/ASEE Joint Propulsion Conference and Exhibit*, June 1999, AIAA 1999-2295.

[77] Manzella, D. H., Yim, J. T., and Boyd, I. D., "Predicting Hall Thruster Operational Lifetime," *40th AIAA/SAE/ASME/ASEE Joint Propulsion Conference and Exhibit*, July 2004, AIAA 2004-3953.

[78] Marrese, C., Gallimore, A. D., Haas, J., Foster, J., King, B., Kim, S. W., , and Khartov, S., "An Investigation of Stationary Plasma Thruster Performance with Krypton Propellant," *31st AIAA/SAE/ASME/ASEE Joint Propulsion Conference and Exhibit*, July 1995, AIAA 95-2932.

[79] Maslennikov, N. A., “Lifetime of the Stationary Plasma Thruster,” *24th International Electric Propulsion Conference*, 1995, IEPC 95-75.

[80] Mason, L. S., Jankovsky, R. S., and Manzella, D. H., “1000 Hours of Testing on a 10 Kilowatt Hall Effect Thruster,” *37th AIAA/SAE/ASME/ASEE Joint Propulsion Conference and Exhibit*, July 2001, AIAA 2001-3773.

[81] Matsunami, N., Yamamura, Y., Itikawa, Y., Itoh, N., Kazumata, Y., Miyagawa, S., Morita, K., and Shimizu, R., “A Semiempirical Formula for the Energy Dependence of the Sputtering Yield,” *Radiation Effects Letters*, Vol. 57, 1980, pp. 15–21.

[82] Mirkarimi, P. B., McCarty, K. F., and Medlin, D. L., “Review of Advances in Cubic Boron Nitride Film Synthesis,” *Materials Science and Engineering*, Vol. R21, 1997, pp. 47–100.

[83] Mitchner, M. and Kruger, C. H., *Partially Ionized Gases*, John Wiley & Sons, Inc., 1973.

[84] Morozov, A. I. and Savel’ev, V. V., “Fundamentals of Stationary Plasma Thruster Theory,” *Reviews of Plasma Physics*, edited by B. B. Kadomtsev and V. D. Shafranov, Vol. 21, Kluwer Academic / Plenum Publishers, New York, 2000, pp. 203–391.

[85] Nakles, M. R., Wang, J. J., Shutthanandan, V., and Zhang, Y., “Further Investigation of Low-Energy Ion Sputtering in Ion Thrusters,” *40th AIAA/SAE/ASME/ASEE Joint Propulsion Conference and Exhibit*, July 2004, AIAA 2004-3789.

[86] Nicholson, D. R., *Introduction to Plasma Theory*, John Wiley & Sons, Inc., 1983.

[87] O’Connor, D. J. and Biersack, J. P., “Comparison of Theoretical and Empirical Interatomic Potentials,” *Nuclear Instruments and Methods in Physics Research B*, Vol. 15, 1986, pp. 14–19.

[88] Ohler, S. G., Gilchrist, B. E., and Gallimore, A. D., “Electromagnetic Signal Modification in a Localized High-Speed Plasma Flow: Simulations and Experimental Validation of a Stationary Plasma Thruster,” *IEEE Transactions on Plasma Science*, Vol. 27, No. 2, 1999, pp. 587–594.

[89] Peterson, P. Y., Jacobson, D. T., Manzella, D. H., and John, J. W., “The Performance and Wear Characterization of a High-Power High-Isp NASA Hall Thruster,” *41st AIAA/SAE/ASME/ASEE Joint Propulsion Conference and Exhibit*, July 2005, AIAA 2005-4243.

[90] Petrosov, V., Baranov, V., Vasin, A., Kaliaev, A., and Nazarenko, Y., “The SPT Channel Erosion Model,” *24th International Electric Propulsion Conference*, 1995, IEPC 95-60.

[91] Promokhov, A. A., Mosunov, A. S., Elovikov, S. S., and Yurasova, V. E., “Features of Sputtering of Nitrides with Various Component Mass Ratios,” *Vacuum*, Vol. 56, 2000, pp. 247–252.

[92] Robinson, M. T. and Torrens, I. M., "Computer Simulation of Atomic-Displacement Cascades in Solids in the Binary-Collision Approximation," *Physical Review B*, Vol. 9, No. 12, 1974, pp. 5008–5024.

[93] Roe, P. L., "Approximate Riemann Solvers, Parameter Vectors, and Difference Schemes," *Journal of Computational Physics*, Vol. 135, No. 2, 1997, pp. 250–258.

[94] Roy, S. and Pandey, B. P., "Development of a Finite Element-Based Hall-Thruster Model," *Journal of Propulsion and Power*, Vol. 19, No. 5, Sept. 2003, pp. 964–971.

[95] Rubin, B., Topper, J. L., and Yalin, A. P., "Total and Differential Sputter Yields of Boron Nitride Measured by Quartz Crystal Microbalance and Weight Loss," *30th International Electric Propulsion Conference*, Sept. 2007, IEPC 2007-074.

[96] Sigmund, P., "Theory of Sputtering. I. Sputtering Yield of Amorphous and Polycrystalline Targets," *Physical Review*, Vol. 184, No. 2, 1969, pp. 383–416.

[97] Sigmund, P., "Sputtering by Ion Bombardment: Theoretical Concepts," *Sputtering by Particle Bombardment (Topics in Applied Physics)*, edited by R. Behrisch, Vol. 47, Springer-Verlag, Berlin, 1981, pp. 9–71.

[98] Sommier, E., Allis, M. K., and Cappelli, M. A., "Wall Erosion in 2D Hall Thruster Simulations," *29th International Electric Propulsion Conference*, Oct. 2005, IEPC-2005-189.

[99] Sorokin, A. A., Shmaenok, L. A., Bobachev, S. V., Möbus, B., Richter, M., and Ulm, G., "Measurements of Electron-Impact Ionization Cross Sections of Argon, Krypton, and Xenon by Comparison with Photoionization," *Physical Review A*, Vol. 61, 2000, pp. 022723.

[100] Sun, Q. and Boyd, I. D., "Evaluation of Macroscopic Properties in the Direct Simulation Monte Carlo Method," *Journal of Thermophysics and Heat Transfer*, Vol. 19, No. 3, 2005, pp. 329–335.

[101] Sutton, G. P. and Biblarz, O., *Rocket Propulsion Elements*, John Wiley & Sons, Inc., 2001.

[102] Szabo, J. J., *Fully Kinetic Modeling of a Hall Thruster*, Ph.D. thesis, Massachusetts Institute of Technology, 2001.

[103] Tersoff, J., "New Empirical Model for the Structural Properties of Silicon," *Physical Review Letters*, Vol. 56, No. 6, Feb. 1986, pp. 632–635.

[104] Tersoff, J., "New Empirical Approach for the Structure and Energy of Covalent Systems," *Physical Review B*, Vol. 37, No. 12, April 1988, pp. 6991–7000.

[105] Urbassek, H. M., "Molecular-Dynamics Simulation of Sputtering," *Nuclear Instruments and Methods in Physics Research B*, Vol. 122, 1997, pp. 427–441.

[106] Vel, L., Gemazeau, G., and Etourneau, J., "Cubic Boron Nitride: Synthesis, Physicochemical Properties and Applications," *Materials Science and Engineering B*, Vol. B10, No. 2, Oct. 1991, pp. 149–164.

[107] Wilhelm, H. E., "Quantum-Statistical Analysis of Surface Sputtering," *Journal of Spacecraft*, Vol. 13, No. 2, 1976, pp. 116–118.

[108] Wilhelm, H. E., "Quantum-Statistical Analysis of Low Energy Sputtering," *Australian Journal of Physics*, Vol. 38, 1985, pp. 125–133.

[109] Yalin, A. P., Rubin, B., Domingue, S. R., Glueckert, Z., and Williams, J. D., "Differential Sputter Yields of Boron Nitride, Quartz, and Kapton Due to Low Energy Xe+ Bombardment," *43rd AIAA/SAE/ASME/ASEE Joint Propulsion Conference and Exhibit*, July 2007, AIAA 2007-5314.

[110] Yalin, A. P., Surla, V., Farnell, C., Butweiller, M., and Williams, J. D., "Sputtering Studies of Multi-Component Materials by Weight Loss and Cavity Ring-Down Spectroscopy," *42nd AIAA/SAE/ASME/ASEE Joint Propulsion Conference and Exhibit*, July 2006, AIAA 2006-4338.

[111] Yalin, A. P., Tao, L., Yamamoto, N., Smith, T. B., and Gallimore, A. D., "Boron Nitride Sputter Erosion Measurements by Cavity Ring-Down Spectroscopy," *30th International Electric Propulsion Conference*, Sept. 2007, IEPC 2007-075.

[112] Yamamura, Y., "An Empirical Formula for Angular Dependence of Sputtering Yields," *Radiation Effects*, Vol. 80, 1984, pp. 57–72.

[113] Yamamura, Y. and Tawara, H., "Energy Dependence of Ion-Induced Sputtering Yields from Monatomic Solids at Normal Incidence," *Atomic Data and Nuclear Data Tables*, Vol. 62, No. 2, March 1996, pp. 149–253.

[114] Yamashiro, M., Yamada, H., and Hamaguchi, S., "Molecular Dynamics Simulation Study on Substrate Temperature Dependence of Sputtering Yields for an Organic Polymer Under Ion Bombardment," *Journal of Applied Physics*, Vol. 101, 2007, pp. 046108.

[115] Yang, G., Causon, D. M., Ingram, D. M., Saunders, R., and Batten, P., "A Cartesian Cut Cell Method for Compressible Flows Part A: Static Body Problems," *The Aeronautical Journal*, Vol. 101, 1997, pp. 47–56.

[116] Yim, J. T., Keidar, M., and Boyd, I. D., "An Investigation of Factors Involved in Hall Thruster Wall Erosion Modeling," *42nd AIAA/SAE/ASME/ASEE Joint Propulsion Conference and Exhibit*, July 2006, AIAA 2006-4657.

[117] Yu, D., Li, Y., and Song, S., "Ion Sputtering Erosion of Channel Wall Corners in Hall Thrusters," *Journal of Physics D: Applied Physics*, Vol. 39, 2006, pp. 2205–2211.

[118] Zhang, L. and Zhang, Z. L., "Anisotropic Energy Distribution of Sputtered Atoms Induced by Low Energy Heavy Ion Bombardment," *Radiation Effects and Defects in Solids*, Vol. 160, Aug. 2005, pp. 337–347.

[119] Zhang, Z. L. and Zhang, L., "Anisotropic Angular Distribution of Sputtered Atoms," *Radiation Effects and Defects in Solids*, Vol. 159, May 2004, pp. 301–307.

[120] Zhou, X. W., Wadley, H. N. G., and Sainathan, S., "Low Energy Sputtering of Nickel by Normally Incident Xenon Ions," *Nuclear Instruments and Methods in Physics Research B*, Vol. 234, 2005, pp. 441–457.

[121] Zhurin, V. V., Kaufman, H. R., and Robinson, R. S., "Physics of Closed Drift Thrusters," *Plasma Sources Science and Technology*, Vol. 8, No. 1, 1999, pp. R1–R20.

[122] Ziegler, J. F., Biersack, J. P., and Littmark, U., *The Stopping and Range of Ions in Solids*, Pergamon Press, 1985.